Imperial College London

Si/SiGe Thermoelectric Generator

A THESIS

SUBMITTED TO THE DEPARTMENT OF

ELECTRICAL&ELECTRONIC ENGINEERING OF

IMPERIAL COLLEGE LONDON

IN FULFILMENT OF THE REQUIREMENTS

FOR THE DEGREE OF

DOCTOR OF PHILOSOPHY

Bin Xu

2015

Declaration of Originality

I hereby declare that this thesis is entirely my own work and that any additional sources of information have been duly cited.

I hereby declare that any internet sources, published or unpublished work from which I have quoted or drawn references have been referenced fully in the text and reference. I understand that failure to do this will result in failure of this thesis due to plagiarism.

Copyright Declaration

The copyright of this thesis rests with the author and is made available under a Creative Commons Attribution Non-Commercial No Derivatives licence. Researchers are free to copy, distribute or transmit the thesis on the condition that they attribute it, that they do not use it for commercial purpose and that they do not alter, transform or build upon it. For any reuse or redistribution, researchers must make clear to others the licence terms of this work.

Abstract

This PhD thesis researches thermoelectric generator (TEG) which transfers wasted heat into electricity by thermoelectric materials.

As a parameter used to characterize thermoelectric materials, figure-of-merit (ZT) models of Si bulk, $Si/Si_{1-x}Ge_x$ bulk and Si bulk/nanowires (NWs) are built via building their models of Seebeck coefficient, electrical conductivity and thermal conductivity in this thesis. ZT of Si bulk is increased by 18% by applying a $3\mu m$ thick $Si_{0.8}Ge_{0.2}$ bulk layer, and it is increased by 1000% by applying $35\mu m$ long Si NWs.

TEG' s output power model which takes account of the effects of thermoelectric material, as well as all parasitic effects that affect TEG's output power. TEG's output power model demonstrates the output power depends on thermoelectric material's characteristics and the contact interface quality between thermoelectric material and metal probe. Thermoelectric material's characteristics are improved by Si NWs, $Si_{1-x}Ge_x$ bulk, $Si_{1-x}Ge_x$ NWs and spin-on-doping (SOD). SOD also improves the contact interface quality between thermoelectric material and metal probe, which also can be improved by sputter coating a layer of metal on thermoelectric material's surface. Finally, TEG's output power is increased by an order of 3 by these techniques.

Publication list

[1] Xu, B. & Fobelets, K. (2014) Spin-on-doping for output power improvement of silicon nanowire array based thermoelectric power generators. *Journal of Applied Physics*. 115 (21), 214306.

[2] Xu, B., Khouri, W. & Fobelets, K. (2014) Two-Sided silicon nanowire array/bulk thermoelectric power generator. *Electron Device Letters, IEEE* 35(5), 596--598.

[3] Xu, B., Li, C., Myronov, M. & Fobelets, K. (2013) n-Si--p-$Si_{1-x}Ge_x$ nanowire arrays for thermoelectric power generation. *Solid-State Electronics*. 83,107--112.

[4] Khas, M., Rahman, T. & Xu, B. (2013) Impedance spectroscopy of Si nanowire/conjugated polymer compounds. In: *39th Int. Conf. on Micro and Nano Engineering*. 2013

[5] Shougee, A., Rahman, T., Fobelets, K. & Xu, B. (2013) Optimization strategies for thermoelectric power from Si nanowire arrays. In: *39th Int. Conf. on Micro and Nano Engineering*. 2013

[6] Xu, B. & Fobelets, K. (2013) Efficiency improvement of silicon nanowire arrays (NWAs) thermoelectric power generation (TEG) by spin on doping (SOD). In: *The Electrochemical Society (ECS)*.2013

[7] Xu, B., Li, C., Thielemans, K. & Myronov, M. et al. (2012) Thermoelectric performance of nanowire arrays. *Electron Devices, IEEE Transactions* 59 (12), 3193--3198.

[8] Xu, B., Li, C., Myronov, M. & Durrani, Z. et al. (2012) $Si_{1-x}Ge_x$ nanowire arrays for thermoelectric power generation. In: *Silicon-Germanium Technology and Device Meeting (ISTDM)*. 2012

[9] Li, C., Xu, B., Durrani, Z. & Fobelets, K. (2011) SiGe nanowire arrays fabrication and their Seebeck coefficient characterisation. In: *9 th European Conference on Thermoelectrics*. 2011

Acknowledgement

FIRST AND FOREMOST I want to thank my supervisor Dr. Kristel Fobelets for giving me the opportunity to the world of thermoelectric engineering and giving me the opportunity to join her research group. During past four years, she not only helped me a lot in my research, but also impressed me with her persistent way of solving scientific problems. I do not think I can complete my PhD study on time without her help, and it is also impossible for me to publish my paper without her supervision.

Secondly, I want to thank Dr. Munir Ahmad for giving me a lot of suggestions about my experiments in my PhD career. I really saved much time under his excellent assistance.

Thirdly, I want to thank Dr. Chuanbo Li who also gave me a lot of help at the beginning stage of my PhD career, and his help enabled me to begin my PhD research quickly.

Finally, I am very happy that I can do my PhD research in OSD group which is a warm big family.

Table of Contents

Declaration of Originality I
Copyright Declaration II
Abstract III
Publication list IV
Acknowledgement V
List of symbols VIII
List of figures XIII
List of tables XX
Chapter 1: Introduction 1
1.1: Background: 1
1.2: Relationship between thermoelectric coefficients 1
1.3: Basic principles of a TEG 4
1.4: Thermoelectric transport in a TEG 7
1.5:The Si nanowire arrays TEG 10
1.6: Conclusion 11
1.7: Outlines of this thesis 12
Chapter 2: Literature overview and initial measurements 13
2.1: Introduction 13
2.2: Thermoelectric characteristics of Si NWs, SiGe alloy 13
2.3: Thermoelectric generator based on NWs 16
2.4: Metal assisted chemical etching 17
2.5: Measurement techniques 22
2.5.1: Seebeck coefficient measurement 23
2.5.2: Schottky barrier height and ideality factor measurement 25
2.5.3: Output power measurement 27
2.6 :Conclusion 29
Chapter 3: Theoretical calculations, simulations and predictions 30
3.1: Figure-of-merit (ZT) 30
3.1.1:ZT of bulk 30
3.1.2: ZT of Si NWs at room temperature (T=300K) 53
3.1.3: Conclusions 55
3.2: TEG's theoretical output power 55
3.2.1: Temperature distribution in TEG 59
3.2.2: Voltage distribution in TEG 61
3.3: Spin-on-doping (SOD) 67
3.4: Conclusions 72
Chapter 4: Material preparation 74
4.1: Si bulk and its nanostructures 74
4.1.1: Si bulk 74
4.1.2: Si NWAs 74
4.2: Si/SiGe bulk and its nanostructures 79
4.2.1: Si/SiGe bulk 79

4.2.2:Si/SiGe NWAs 80
4.3: Si bulk and its nano-structures with SOD and sputter coated Cu contacts 81
4.3.1: Si bulk and its nano-structures with SOD 81
4.3.2: Si bulk with sputter coated Cu contacts 82
4.4: Conclusions 85
Chapter 5: Output power of Si and Si/SiGe nanowire arrays 87
5.1: Influences of SiGe alloy and nanostructure 87
5.1.1: Si/$Si_{0.8}Ge_{0.2}$ bulk and nanostructure 87
5.1.2: Si/$Si_{1-x}Ge_x$ (x=0.2, 0.3 and 0.4) bulk, nanostructures and pn junctions 92
5.2: Influence of carrier concentration 96
5.3: TEG's output power increase via SOD 98
5.4: Output power increase by longer NWAs and small sample areas 106
5.5: Conclusions 107
Chapter 6: Conclusion and future work 109
Reference 113

List of symbols

1: Physical quantities

Symbol	Unit	Description
α	mV/K	Seebeck coefficient
α_p	mV/K	Seebeck coefficient of p-type semiconductor
α_n	mV/K	Seebeck coefficient of n-type semiconductor
α_{pe}	mV/K	Electronic contribution to the Seebeck coefficient of p-type semiconductor
α_{ne}	mV/K	Electronic contribution to the Seebeck coefficient of n-type semiconductor
$\alpha_{measurement}$	mV/K	Measured Seebeck coefficient
α_{real}	mV/K	Real Seebeck coefficient
α_{TE}	mV/K	Seebeck coefficient of thermoelectric material
$\lvert\alpha_n^{real}\rvert$	mV/K	Absolute value of n-type semiconductor's real Seebeck coefficient
$\lvert\alpha_p^{real}\rvert$	mV/K	Absolute value of p-type semiconductor's real Seebeck coefficient
α_{tot}^{real}	mV/K	$\lvert\alpha_n^{real}\rvert + \lvert\alpha_p^{real}\rvert$
α_{NWAs}	mV/K	Seebeck coefficients of Si NWAs
α_{Bulk}	mV/K	Seebeck coefficients of Si bulk
ΔV	mV	Voltage difference
V	mV	Voltage
V_R	mV	Voltage of load resistance
V_{oc}	mV	Open circuit voltage
T_h	K	High temperature
T_c	K	Low temperature
ΔT	K	Temperature difference
ΔT_{Cu}	K	Temperature drop across Cu
ΔT_{Bulk}	K	Temperature drop across Si bulk
ΔT_{NWAs}	K	Temperature drop across Si NWAs
ΔT_i	K	Temperature drop at contact interface
ΔT_s	K	$\Delta T_{Bulk} + \Delta T_{NWAs}$ or temperature drop across sample
ΔT_{max}	K	Maximum temperature difference
$\Delta T_{Si\ bulk}$	K	Temperature drop across Si bulk
$\Delta T_{Si_{0.8}Ge_{0.2}\ bulk}$	K	Temperature drop across the $Si_{0.8}Ge_{0.2}$ bulk
$\Delta T_{Si\ NWAs}$	K	Temperature drop across Si NWAs
T	K	Temperature
Π	mV	Peltier Coefficient

q	μW	Heat flux
I	mA	Electrical current
τ	mV/K	Thomson coefficient
R_L	Ω	Load resistance
R_{TEG}	Ω	Resistance of TEG
R_{diff}	Ω	Resistance gotten via I-V figure
K	$\mu W/K$	Thermal conductance
η	—	Efficiency
ZT	—	Figure-of-merit
ZT_{NW}	—	ZT of individual NWs
ZT_{comp}	—	ZT of the NW/matrix composite material
σ_{TEG}	$1/(\Omega \cdot cm)$	Electrical conductivity of TEG
σ_n	$1/(\Omega \cdot cm)$	Electrical conductivity of n-type bulk
σ_p	$1/(\Omega \cdot cm)$	Electrical conductivity of p-type bulk
σ_{TE}	$1/(\Omega \cdot cm)$	Electrical conductivity of thermoelectric material
σ_i	$1/(\Omega \cdot cm)$	Electrical conductivity of intermediate layer
λ	$W/(K \cdot cm)$	Thermal conductivity
λ_{matrix}	$W/(K \cdot cm)$	Matrix thermal conductivity
λ_{NW}	$W/(K \cdot cm)$	NW thermal conductivity
λ_{SOG}	$W/(K \cdot cm)$	Spin-on-glass thermal conductivity
λ_{TE}	$W/(K \cdot cm)$	Thermal conductivity of thermoelectric material
$\lambda_{Si\ bulk}$	$W/(K \cdot cm)$	Thermal conductivity of Si bulk
$\lambda_{Si_{0.8}Ge_{0.2}\ bulk}$	$W/(K \cdot cm)$	Thermal conductivity of $Si_{0.8}Ge_{0.2}$ bulk
$\lambda_{Si\ NWAs}$	$W/(K \cdot cm)$	Thermal conductivity of Si NWAs
λ_c	$W/(K \cdot cm)$	Thermal conductivity of the contact layer
J	mA/cm^2	Current density
J_n	mA/cm^2	Current density inside n-type bulk
J_p	mA/cm^2	Current density inside p-type bulk
L	cm	Length
$L_{Si\ bulk}$	μm	Si bulk's thickness
$L_{Si\ NWAs}$	μm	Si NWAs length
$L_{Si_{0.8}Ge_{0.2}\ bulk}$	μm	$Si_{0.8}Ge_{0.2}$ bulk's thickness
L_{NWAs}	μm	NWAs length
L_c	μm	Thickness of the contact layer
A	cm^2	Area
$A_{Si\ Bulk}$	cm^2	Area of Si bulk

$A_{Si\ NWAs}$	cm^2	Area of Si NWAs
x	cm	x-axis
P or P_{out}	nW or μW	Output power
P_{out}^{max}	nW or μW	Maximum output power
f_{NW}	—	NW packing density
$\emptyset_B$	eV	Schottky barrier height
n_0	—	Ideality factor
S_v	—	Carrier charge sign
μ	$cm^2/V \cdot s$	Carrier mobility
μ_n	$cm^2/V \cdot s$	Electron mobility
μ_P	$cm^2/V \cdot s$	Hole mobility
μ_{Si}	$cm^2/V \cdot s$	Si's carrier mobility
μ_{Ge}	$cm^2/V \cdot s$	Ge's carrier mobility
$\mu_{Si_{1-x}Ge_x}$	$cm^2/V \cdot s$	$Si_{1-x}Ge_x$ carrier mobility
Φ	V	Electrochemical potential of carrier
Φ_n	V	Electrochemical potential of electrons
Φ_p	V	Electrochemical potential of holes
$N_{c,V}$	cm^{-3}	Effective density states in the conduction/valence band
n	cm^{-3}	Electron concentration
p	cm^{-3}	Hole concentration
s	m/s	Sound velocity
F	—	Fraction of the carrier's momentum that is transferred to the sound waves
τ_r	s	Relaxation time
E_{LH}	eV	Energy of light hole
E_{HH}	eV	Energy of heavy hole
m_{LH}^*	kg	Light hole effective mass
m_{HH}^*	kg	Heavy hole effective mass
m_{nx}^*	kg	Effective density of state mass in the X minima of the conduction band
m_{nL}^*	kg	Effective density of state mass in the L minima of the conduction band
E_{cx}	eV	Energy at the bottom of the X energy valley
E_{cL}	eV	Energy at the bottom of the L energy valley
N	cm^{-3}	Carrier concentration
N_A	cm^{-3}	Acceptor doping density
N_D	cm^{-3}	Donor doping density
N_{NWAs}	cm^{-3}	Doping density of NWAs
N_{bulk}	cm^{-3}	Doping density of bulk
n_i	cm^{-3}	Intrinsic carrier concentration

ΔE_g^*	meV	Apparent band-gap narrowing caused by heavily doping
f	Hz	Phonon frequency
τ_N	s	N-process relaxation time
τ_p	s	U-process relaxation time
M	—	Atomic weight
δ	cm	Cube root of the atomic volume
θ	K	Derby temperature
W_p	$W^{-1} \cdot K \cdot cm$	Lattice thermal resistivity due to three phonon an-harmonic scattering
W	$W^{-1} \cdot K \cdot cm$	Total lattice thermal resistivity includes three phonon an-harmonic scattering and disorder of the lattice
R_{tc}	$W^{-1} \cdot K \cdot cm^2$	Thermal contact resistance
$\emptyset_s$	eV	Si's work function
$\emptyset_m$	eV	Cu's work function
E_g	eV	Band gap
χ_s	eV	Electron affinity
E_{00}	J	Characteristic energy
R_c	$\Omega \cdot cm^2$	Specific contact resistance
E_0	1	Tunneling probability in the TFE region
E_F	eV	Fermi level
E_C	eV	Conduction band
E_V	eV	Valence band
U_F	eV	$E_F - E_C$ or $E_V - E_F$
t	s	Time
C_{surf}	cm^{-3}	Surface carrier concentration
ρ	Ω·cm	Electrical resistivity
ρ_{Bulk}	Ω·cm	Electrical resistivity of bulk
ρ_c	Ω· μm	Electrical contact resistivity
r	—	Scattering factor
n_{SOD}	—	Number of SOD applications

2: Constants

Symbol	Value and Unit	Description
A^*	$112\frac{A}{cm^2 \cdot K^2}$ for n-type Si $32\frac{A}{cm^2 \cdot K^2}$ for p-type Si	Richardson's constant
k	$1.38 \times 10^{-23} J/K$	Boltzmann constant

e	1.6×10^{-19}C	Unit charge
h	6.626×10^{-34}J · s	Planck constant
ħ	1.06×10^{-34}J · s	Reduced Planck constant
m^*	$m_e^* = 9.8388 \times 10^{-31}$kg $m_h^* = 10.37929 \times 10^{-31}$kg	Carrier effective mass. m_e^* is for electrons and m_h^* is for holes
π	3.14	Ratio of a circle's circumference to its diameter
m_0	9.11×10^{-31} kg	Free electron's mass
m	1.66×10^{-27}kg	Unit atomic mass
M_{Si}	28.09	Si atomic weight
M_{Ge}	72.6	Ge atomic weight
ΔM	44.51	M_{Ge}-M_{Si}
δ_{Si}	2.7155×10^{-8} cm	Si cube root of the atomic volume
δ_{Ge}	2.82875×10^{-8}cm	Ge cube root of the atomic volume
Δδ	0.11325×10^{-8} cm	$\delta_{Ge} - \delta_{Si}$
β	1.52×10^{-8}K · $cm^{3/2}$	Constant within SiGe alloy
ϵ	1.04×10^{-10}F/m	Si's dielectric constant

List of figures

1.1: Junction with two dissimilar material A and B of which one end is at a higher temperature than the other end: $T_h > T_c$. An open circuit voltage ΔV is created as a function of ΔT (Rowe, 1995). P.2

1.2: Schematic of basic TEG which is constructed from an n- and p-type semiconductor. The holes in the p-type and the electrons in the n-type semiconductor both diffuse from the hot (T_h) to the cold side (T_c) and hence current is generated in the load resistance (Rowe,1995). P.4

1.3: Thermoelectric properties of materials: Insulators have low $\alpha^2\sigma$ due to its pretty low σ; Metals also have low $\alpha^2\sigma$ due to its extremely low α; Semiconductor has highest $\alpha^2\sigma$ by controlling carrier concentration via doping, and it has relatively low λ(Xu, 2012). P.6

1.4: State of the art ZTvalues for a range of materials relevant to this research (Minnich, Dresselhaus & Ren et al., 2009). P.7

1.5: TEG structure and boundary conditions. J is the current density. q is the heat flux. V is the electrostatic potential and T the temperature. P.7

1.6: Simulated output power as a function of load resistance for a TEG (L=0.05cm, A=1.5cm^2). The α is assumed to be constant at 1mV/K. (a): Influence of temperature difference, $\Delta T = 2,3$ and 4K, with $\sigma_{TEG} = \frac{1}{6}\frac{1}{k\Omega.cm}$; (b): Influence of electrical conductivity, $\sigma_{TEG} = 0.05, 0.075$ and $0.1\frac{1}{k\Omega.cm}$, with $\Delta T =$ 4K. P.9

1.7: (a): SEM picture of a Si NWA's cross section view and top view (upper left).
(b): Schematic of a possible Si NWA TEG. P.10

1.8: NWAs TEG between Cu blocks for measurements. Electrical and Thermal contact resistances are indicated on the sketch. Voltage and temperature are measured in the Cu blocks. Al_2N_3 is a thermal conductor and electrical insulator needed to keep the temperature the same in the two Cu blocks at the cold side (Snyder, 2008). P.11

2.1: Growth mechanism for Si NWAs (Peng, Yan & Gao et al., 2003). P.18

2.2: $Si_{0.6}Ge_{0.4}$ NWs which are prepared by one-step MACE. P.19

2.3: Electroless Ag deposition (Peng, Wu & Fang et al., 2005), (Zhang, Peng & Fan et al., 2008). P.20

2.4: Electrochemical anodic dissolution of Si (Peng, Wu & Fang et al., 2005), (Zhang, Peng & Fan et al., 2008). P.20

2.5: SEM and TEM images show the evolution of Si NWs morphology from n-type Si(100) with $0.008 - 0.02\Omega \cdot cm$ resistivity in etchant solution composed of 4.8 M HF and 0.2 M H_2O_2 for 30 min (a and b) and 60 min(c and d). NWs length increases with increasing etching time, and NWs are more porous with longer etching time due to Ag NPs become smaller and smaller in the etching process (Qu, Liao & Li et al., 2009). P.21

2.6: (a): Tritt's Seebeck coefficient measurement set-up (Rowe, 1995).
(b): Seebeck coefficient measurement set-up used in our research. P.23

2.7: (a): Rough surfaces contact and temperature drop (Chapman, 1987).
(b) Temperature drops in the Seebeck coefficient measurement set-up. P.24

2.8 :(a): Measured Seebeck coefficient as a function of pressure. The markers are measurement values, and the solid line is a guide to the eye only.
(b):Temperature difference measurement ΔT as a function of heater power P_{heat} for a Si/SiGe NWAs sample between two Cu blocks. ×: measurement without Ag foil, + measurement with Ag foil. The solid lines are guides to the eye only. P.25

2.9: Schottky barrier height and ideality factor measurement set-up. P.26

2.10: (a): I-V characteristic of n-type Si ($1\text{-}10\Omega \cdot cm$) bulk.
(b):The natural logarithm of the current for V > 0.8 V in order to satisfy $V \gg kT/e$. P.27

2.11: One-leg output power measurement set-up. (a): Original set-up.(b) Enhanced set-up. P.27

2.12: Two-leg output power measurement set-up. P.28

3.1: n-type and p-type Si bulk's Seebeck coefficient as a function of temperature and carrier concentration. The solid lines are theoretical Seebeck coefficients of Si gotten via eq. (3.4 and 3.5), and the square points are Seebeck coefficients measured by Geballe & Hull (Geballe & Hull, 1955) and Slack & Hussain (Slack & Hussain, 1991). P.33

3.2: Seebeck coefficient of $Si_{0.8}Ge_{0.2}$ bulk as a function of temperature and carrier concentration. P.34

3.3: Seebeck coefficient of $Si_{1-x}Ge_x$ bulk as a function of Ge fraction(x) and carrier concentration. P.35

3.4: Carrier mobility of bulk Si as a function of temperature and doping density for (a) electron and (b) hole. P.36

3.5: Electrical conductivity of bulk Si as a function of temperature and doping density for (a) n-type and (b) p-type Si. P.39

3.6: Carrier mobility of bulk Ge as a function of doping density at room temperature (T=300K) (Pierret & Huang, 2004). P.40

3.7: Carrier mobility of bulk Ge as a function of doping density at room temperature (T=300K). The black solid line is measured value (Pierret & Huang, 2004). The red and blue solid lines are theoretical values. P.42

3.8: Carrier mobility of bulk Ge as a function of temperature and doping density for (a) electron and (b) hole. P.42

3.9: Carrier mobility of $Si_{0.8}Ge_{0.2}$ bulk as a function of temperature with different doping densities for (a) electron and (b) hole. P.43

3.10: Electrical conductivity of bulk $Si_{0.8}Ge_{0.2}$ as a function of temperature and doping density for (a) n-type and (b) p-type. P.43

3.11: Lattice thermal conductivity of bulk Si as a function of temperature (Glassbrenner & Slack, 1964). P.44

3.12: Electronic portion of thermal conductivity for (a) n-type Si bulk and (b) p-type Si bulk. P.44

3.13: Thermal conductivity of bulk Si as a function of temperature and doping density for (a) n-type and (b) p-type. P.45

3.14: Lattice thermal conductivity of $Si_{1-x}Ge_x$ as a function of Ge fraction and temperature. P.47

3.15: $Si_{0.8}Ge_{0.2}$ electronic portion of thermal conductivity as a function of temperature and doping density for (a) n-type bulk and (b) p-type bulk. P.48

3.16: Thermal conductivity of bulk $Si_{0.8}Ge_{0.2}$ as a function of temperature and doping density for (a) n-type and (b) p-type. P.48

3.17: ZT of Si bulk as a function of doping density and temperature for (a) n-type and (b) p-type. P.49

3.18: ZT of $Si_{0.8}Ge_{0.2}$ as a function of doping density and temperature for (a) n-type

and (b) p-type bulk. P.49

3.19: The structure of $Si/Si_{1-x}Ge_x$ bulk. P.50

3.20: Thermal conductivity as a function of doping density and temperature for (a) n-type $Si/Si_{0.8}Ge_{0.2}$ bulk and (b) p-type $Si/Si_{0.8}Ge_{0.2}$ bulk. P.51

3.21: Seebeck coefficient as a function of doping density and temperature for n-type and p-type $Si/Si_{0.8}Ge_{0.2}$ bulk. P.52

3.22: Electrical conductivity as a function of doping density and temperature for (a) n-type $Si/Si_{0.8}Ge_{0.2}$ bulk and (b) p-type $Si/Si_{0.8}Ge_{0.2}$ bulk. P.53

3.23: ZT as a function of doping density and temperature for (a) n-type $Si/Si_{0.8}Ge_{0.2}$ bulk and (b) p-type $Si/Si_{0.8}Ge_{0.2}$ bulk. P.53

3.24: ZT of Si bulk/NWs sample as a function of doping density at room temperature. P.54

3.25: Highest ZT of Si bulk, $Si/Si_{0.8}Ge_{0.2}$ bulk and Si bulk/NWs as a function of temperature. The doping density of n-Si bulk and n-$Si/Si_{0.8}Ge_{0.2}$ bulk with highest ZT is$10^{20}cm^{-3}$, and the doping density of remaining samples with highest ZT is$10^{19}cm^{-3}$. P.55

3.26: Schematic of five-layer structure with cross section area of $2cm \times 2cm$. P.56

3.27: TEG's output power as a function of load resistance with different electrical conductivities of intermediate layers. P.57

3.28: TEG's output power as a function of load resistance R_L with the same intermediate layer and different thermoelectric materials. P.59

3.29: Model in COMSOL. P.60

3.30: COMSOL simulation of temperature distribution. (a): the cross section of Fig. 3.29; (b) the temperature distribution along the red solid line in (a). P.61

3.31: Temperature distribution along thermoelectric material which is n-type Si bulk whose doping density is$10^{19}cm^{-3}$, as well as with thickness of $500\mu m$and area of$4cm^2$. The intermediate layer's electrical conductivity is$1.5 \times 10^{-7}\frac{1}{\Omega \cdot cm}$. P.62

3.32: The voltage distribution in TEG whose thermoelectric material is n-type Si bulk with doping density of $10^{19}cm^{-3}$, as well as thickness of$500\mu m$, area of $4cm^2$ and

the heat flux is 1W. (a): as a function of load resistance with $\sigma_i = 1.5 \times 10^{-7} \frac{1}{\Omega \cdot cm}$; (b): as a function of intermediate layer's electrical conductivity σ_i with $R_L = 500\Omega$. P.63

3.33: (a): Energy band diagrams of Cu and n-type Si.
(b): Schottky contact at Cu/n-type Si contact; (c): Energy band diagrams of Cu and p-type Si; (d): Schottky contact at Cu/p-type Si contact (Turner & Rhoderick, 1968). P.64

3.34: Si's work function as a function of carrier concentration at room temperature. (a): n-type Si ;(b): p-type Si. P.65

3.35: Ideal specific contact resistance as a function of doping density with different Schottky barrier heights. (a): Cu and n-type Si contact, $m^* = 0.26m_0$, $\epsilon = 11.8\epsilon_0$,T=300K, A=4 cm^2 , $A^* = 200 \frac{A}{cm^2 \cdot K^2}$, $N_C = 2.8 \times 10^{19} cm^{-3}$. (b): Cu and p-type Si contact, $m^* = 0.6m_0$, $\epsilon = 11.8\epsilon_0$,T=300K, A=4 cm^2 , $A^* = 79 \frac{A}{cm^2 \cdot K^2}$, $N_V = 3.1 \times 10^{19} cm^{-3}$ (Chang, Fang & Sze, 1971). P.67

3.36: Phosphorous concentration at the Si surface as a function of RTP time duration (Mathiot, Lachiq & Slaoui et al., 1998). P.71

3.37: Electrically active phosphorous concentration profiles by ARHS measurement for SOG/Si samples RTP annealed for 25s at 850℃, 900℃, 950℃ and 1000℃(Hartiti, Slaoui & Muller et al., 1992). P.72

3.38: Boron's solubility in Si as a function of temperature (Vick & Whittle, 1969). The circles are the measurement values and the solid line is the regression line. P.73

3.39: Boron's dopant profile in Si as a function of temperature and diffusion time (Wehmeier, Schraps & Wagner et al., 2013). P.73

4.1: Si NWAS. (a): n-type (1-10 Ω· cm);(b): p-type (1-5 Ω· cm).P.76

4.2: p-type Si (0.01-0.02Ω· cm) NWAs. P.77

4.3: Output voltages of p-type Si NWAs as a function of time when a fixed temperature difference is applied. (a): p-type (0.01-0.02 Ω·cm), ΔT=0K;(b): p-type (0.01-0.02 Ω·cm), ΔT=9.8K. P.77

4.4: (a): Top view cross section of a single p-type Si nanowire. R is the NW radius

and W is the depletion width due to the surface depletion. The white area is the remaining conduction path.

(b): Schematic of collapsed p-type Si NWs which make large amounts of positive charges at the surface of the Cu contact. P.78

4.5: p-type Si (0.01-0.02 Ω· cm) NWAs. P.79

4.6: n-type Si (0.01-0.02 Ω·cm) NWAs (using heavy Ag nucleation). P.79

4.7: n-type Si (0.01-0.02 Ω·cm) NWAs (light Ag nucleation). P.80

4.8. (a): SEM cross-section of $Si_{0.8}Ge_{0.2}$ NWAs.

(b): EDX spectrum of $Si_{0.8}Ge_{0.2}$ NWAs taken from (a). The red line is taken from '1', and the blue line is taken from '2'. (c): The length of NWAs for an etch time of 15 min as a function of Ge fraction etched with the same chemical recipe. P.81

4.9. (a): I-V characteristic of n-type Si bulk (1-10 Ω · cm) with sputtered Cu contacts.

(b): The natural logarithm of the current as a function of voltage. P.84

4.10: I-V characteristics for Si samples with SOD on both surfaces. (a): n-type Si bulk (1-10 Ω· cm); (b): n-type Si bulk (0.01-0.02 Ω· cm); (c): p-type Si bulk (1-5 Ω· cm); (d): p-type Si bulk (0.01-0.02 Ω· cm). P.85

4.11: I-V characteristics, SOD and sputter coating are done on Si two surfaces. (a): n-type Si bulk(1-10 Ω· cm); (b): n-type Si bulk (0.01-0.02 Ω· cm); (c): p-type Si bulk (1-5 Ω· cm); (d): p -type Si bulk (0.01-0.02 Ω· cm). P.86

5.1: I-V figure of all samples using a Cu pressure contact. P.89

5.2: Output power of all samples. Solid lines are the theoretical calculations, and squares are the measured values. Output power is measured under the same heat input. P.90

5.3: Output power P_{out} normalized by ΔT_s^2 as a function of load resistance R_L. P.93

5.4: Seebeck coefficient measurement. (a): For the individual n- and p-type Si NWAs samples and the pn junction made with the same material. No Ag foil is used and no pressure is applied. (b) For all three SiGe samples containing SiGe NWAs. Ag foil is used to minimize the temperature drop across the interface and a pressure of $167 N/cm^2$ is applied. P.95

5.5: Output power P_{out} as a function of load resistance R_L for four different pn junction configurations. (a) Bulk samples. (b) NWAs samples. P.96

5.6: Output power P_{out} as a function of load resistance R_L for Si bulk and Si NWAs pn junction TEGs. (a): ρ ≈5.6Ω·cm ;(b): ρ ≈0.01Ω·cm. P.98

5.7: Samples used in this experiment. P.101

5.8: I-V characteristics of S2 and S6. P.102

5.9 (a): Open circuit voltage versus temperature difference measurements.
(b) Output power measurements as a function of load resistance for constant heat flux. Open markers: p-type sample and closed markers n-type samples. Squares and triangles are bulk samples with and without SOD, respectively. Circles are NWAs/bulk samples with SOD. The SOD applied forms an Ohmic contact (Xu & Fobelets, 2014). P.102

5.10: Raw performance parameters for n-type Si as a function of SOD applications. (a),(c): Seebeck coefficient. (b),(d): Maximum output power. (a),(b) bulk, (c),(d) NWAs/bulk(Xu & Fobelets, 2014). P.104

5.11: Raw performance parameters for p-Si as a function of anneal time. (a),(c): Seebeck coefficient. (b),(d): Maximum output power. (a),(b) bulk, (c),(d) NWA/bulk(Xu & Fobelets, 2014). P.104

5.12: Si NWAs with the arrows indicating the direction of the dopants diffusion (Xu & Fobelets, 2014). P.105

List of tables

3.1: Parameters for electrons and holes (Pierret & Huang, 2004). P.36

3.2: Thermal conductivity of bulk Si at different temperatures. P.45

3.3: Sheet resistance of Si after SOD as a function of phosphorus concentration (Mathiot, Lachiq & Slaoui et al., 1998). P.70

3.4: Sheet resistance of Si after SOD as a function of RTP temperature (Mathiot, Lachiq & Slaoui et al., 1998). P.71

4.1: Ideality factor (n_0) and Schottky barrier height ($\emptyset_B$) for Cu-Si contacts at room temperature (kT=0.0258eV). The contact area is 4 cm^2, the Richardson's constant for n-type Si is $112\frac{A}{cm^2 \cdot K^2}$, and the Richardson's constant for p-type Si is $32\frac{A}{cm^2 \cdot K^2}$ (Li & Thurder, 1977). P.83

4.2: n and $\emptyset_B$ are obtained at room temperature (kT=0.0258eV). P.84

4.3: Summary of the contact resistance. P.85

4.4: Summary of contact resistance. P.86

5.1: Summary of measured values in Figure 5.2. P.90

5.2: Seebeck coefficient and temperature drops across samples. P.91

5.3: Length of the NWAs, L_{NWAs}, the measured Seebeck coefficient, α for the different Ge fractions and the real Seebeck coefficient, α_{real} that takes into account the temperature drop at the interfaces. P.95

5.4: Performance parameters for the different TEGs: maximum output power P_{out}^{max}, internal resistance R_{TEG}, temperature difference ΔT, open circuit voltage ΔV, and NWAs length L_{NWAs}. Samples in the first column only indicate the p-type sample of pn junctions. Subscript p and n in the last column indicate the doping type of the NWAs. P.97

5.5: Performance parameters for different starting wafers. P.98

5.6: Measurement summaries of all samples. R_L is the load resistance which matches TEG's internal resistance($R_L = R_{TEG}$), and R_{diff} is the resistance gotten via I-V figure(Xu & Fobelets, 2014). P.102

5.7: Summary of the extracted parameters. α the Seebeck coefficient; P_{out} the maximum output power, R_{TEG} the internal resistance of the TEG, ΔT the temperature difference, T_h the hot side temperature for the same heat flux and ρ the resistivity measured by 4-point-probe measurement(Xu & Fobelets, 2014). P.105

5.8: Summary of the extracted Seebeck coefficients for the NWAs(Xu & Fobelets, 2014). P.106

5.9: Power factor for samples with maximum SOD(Xu & Fobelets, 2014). P.107

5.10: Summary of raw measurement results (Xu, Khouri & Fobelets, 2014). P.108

Chapter 1: Introduction

1.1: Background:

Historically, the development and use of energy facilitates the progress of human society and civilization. The continuous economic growth, industrial development and social stability increasingly depend on the supply of energy, especially that of fossil fuels. As the most significant energy source, fossil fuel is, under the current circumstances, being consumed quickly and oil will run out within 100 years at current exploitation rate (Carboncounted.co.uk, 2014).

The development of new energy and improvements in efficiency of energy distribution and use are considered feasible ways to ease the tight energy supply worldwide. Energy harvesters and scavengers are attracting increased attentions in recent years since they are potential alternative energy sources converting different forms of ambient energy (Jiang, 2011). In practice, many energy conversion techniques are being used, for example, wristwatches are powered by kinetic energy, in this case, movement of the arm; piezoelectric crystals or fibers generate a small voltage whenever they are mechanically deformed; photovoltaics is a method of generating electrical power by converting solar radiation into direct current and so on (Wikipedia, 2013).

Among them is the thermoelectric generator (TEG) which converts heat (temperature difference) directly into electrical energy via the Seebeck effect. In 1821, Thomas Johann Seebeck discovered that a thermal gradient between two dissimilar conductors produces a voltage (Wikipedia, 2014). At the end of World War II the investigation into thermoelectric material and TEGs began to boom due to the development of semiconductor materials (Su, 2014). At the beginning of the 1960s, radioisotope TEGs were successfully used in space exploration by the USA and it is still the first power supply option in space exploration until now (Karacalıoğlu, 2014). From the beginning of the 1990s, many corporations, governments and research institutes invested large amounts of money in thermoelectric material and TEG research for environmental protection and sustainable development. Thus the research of thermoelectric material and TEGs has entered a new era with the advent of nanotechnology (ScienceDaily, 2014).

1.2: Relationship between thermoelectric coefficients

The Seebeck effect is the generation of an open circuit voltage across a junction made of dissimilar material due to a temperature difference across this junction. A simple

thermocouple is given in Fig. 1.1 (Rowe, 1995). Two dissimilar materials A and B are connected electrically in series but thermally in parallel, and a temperature difference $\Delta T = T_h - T_c$ is maintained between the hot and cold junction. The given temperature difference ΔT causes a certain voltage difference ΔV between hot and cold junction. ΔV is proportional to ΔT given by the Seebeck coefficient α (Rowe, 1995).

$$\alpha = \frac{\Delta V}{\Delta T} \tag{1.1}$$

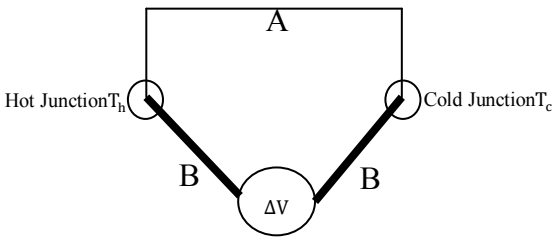


Figure 1.1: Junction with two dissimilar material A and B of which one end is at a higher temperature than the other end: $T_h > T_c$. An open circuit voltage ΔV is created as a function of ΔT (Rowe, 1995).

The Peltier effect is the reverse effect of the Seebeck effect. An electrical current I is driven through two connected dissimilar materials and causes a temperature difference between the two junctions. Thus heat is absorbed in one junction, and rejected in the other junction. Peltier coefficient is defined as Π (Rowe, 1995).

$$\Pi = \frac{q}{I} \tag{1.2}$$

With q the rate of heating (cooling). The Peltier and Seebeck coefficient are not independent of each other. They follow the expression (Rowe, 1995):

$$\Pi = \alpha T \tag{1.3}$$

With T the arithmetic average of T_h and T_c.

The Thomson effect, which was predicted by Lord Kelvin in 1851, relates to the rate of generation or absorption of reversible heat q, which results from the passage of a current I along a portion of a single conductor along which is a temperature differenceΔT. Thomson coefficient is defined as τ (Rowe, 1995):

$$\tau = \frac{q}{I\Delta T} \tag{1.4}$$

Thomson coefficient and Seebeck coefficient are connected by Kelvin's second relations (Rowe, 1995):

$$\tau = T\frac{d\alpha}{dT} \tag{1.5}$$

With T the arithmetic average of T_h and T_c.

Let two dissimilar materials, A and B, given in Fig. 1.1, constitute a circuit in which the hot junction is at temperature T_h and the cold junction is at temperature T_c and both are maintained by heat reservoirs. The Seebeck voltage generated by the temperature difference is ΔV. So the electrical energy is expressed as (Rowe,1995):

$$I\Delta V = I\frac{d(\Delta V)}{dT}\Delta T \tag{1.6}$$

For unit current flowing in the thermoelectric circuit, eq. (1.6) is simplified as:

$$\Delta V = \frac{d(\Delta V)}{dT}\Delta T \tag{1.7}$$

The other energy factors in a thermoelectric circuit are Peltier and Thomson effects. Heat absorbed at the hot junction due to the Peltier effect is πT_h, and heat liberated at the cold junction due to the Peltier effect is πT_c. Heat absorbed in material B due to the Thomson effect is $\tau_B \Delta T$, and heat liberated in material A due to the Thomson effect is $\tau_A \Delta T$.

The thermal and electrical energies can be equated under unit current flow in the circuit, which is given by (Rowe,1995):

$$\frac{d(\Delta V)}{dT}\Delta T = \Pi_{(T_h)} - \Pi_{(T_C)} + (\tau_B - \tau_A)\,\Delta T \tag{1.8}$$

Eq. (1.8) is divided by ΔT to obtain:

$$\frac{d(\Delta V)}{dT} = \frac{d\Pi}{dT} + (\tau_B - \tau_A) \tag{1.9}$$

This is the fundamental thermodynamic theorem for thermoelectric circuits, and it shows the relationship between Seebeck effect, Peltier effect and Thomson effect. This relation is consistent with eq. (1.3) and eq. (1.5).

1.3: Basic principles of a TEG

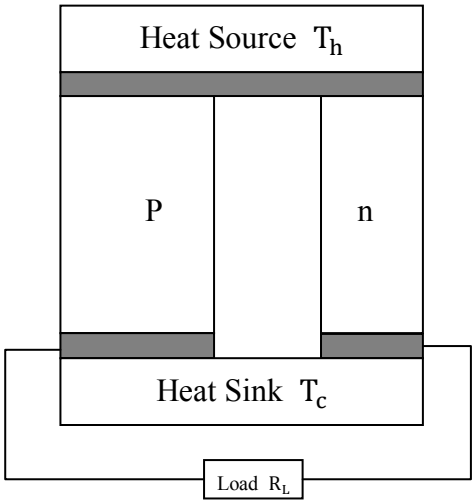


Figure 1.2: Schematic of basic TEG which is constructed from an n- and p-type semiconductor. The holes in the p-type and the electrons in the n-type semiconductor both diffuse from the hot (T_h) to the cold side (T_c) and hence current is generated in the load resistance (Xu, 2012).

A basic TEG is shown in Fig. 1.2. It is constructed from two dissimilar materials, in this case an n- and p-type semiconductor, connected in series electrically and thermally in parallel. When a temperature difference is established across the junction it produces an open circuit voltage, called Seebeck voltage is created. The holes in the p-type and the electrons in the n-type semiconductor both diffuse from the hot to the cold side and hence current flows through the load resistanceR_L. Thus, the conversion between thermal and electrical energy is realized via the diffusion of carrier from hot to cold side which sets up a Seebeck voltage related to the internal electric field (Xu, 2012).

The output power which is shown in Fig. 1.2 is defined as P (Rowe, 1995), (Snyder, 2008):

$$P = [\frac{(\alpha_p - \alpha_n)(T_h - T_c)}{(R_L + R_{TEG})}]^2 R_L \qquad (1.10)$$

With α_p the Seebeck coefficient of p-type semiconductor which is a positive value, α_n is the Seebeck coefficient of n-type semiconductor which is a negative value, R_{TEG} is the resistance of TEG itself.

Next, consider the rate at which heat is supplied by the source. Most of this heat is conducted to the sink through the thermocouple branches but it should not be forgotten that some is used to balance the Peltier effect associated with the flow of current. Also, half of the Joule heating in the arms finds its way to the source. If all these terms are included, the heat rate is given by q (Rowe, 1995), (Snyder, 2008):

$$q = K(T_h - T_c) + (\alpha_p - \alpha_n)\, IT_h - I^2 R_{TEG}/2 \quad (1.11)$$

With K the thermal conductance of the two branches in parallel, I the current is equal to $(\alpha_p - \alpha_n)(T_h - T_c)/(R_L + R_{TEG})$.

The efficiency of the TEG is equal to P/q and its value depends to some extent on the way that the load is matched to the resistance of the TEG. If the ratio of R_L/R_{TEG} is denoted by m, as shown by Rowe (Rowe, 1995), $m = \sqrt{1 + ZT}$ maximizes the efficiency of the TEG. Substituting this value in to eq. (1.11), the efficiency of a TEG is given by η (Snyder, 2008):

$$\eta = \frac{T_h - T_c}{T_h} \frac{\sqrt{1+ZT}-1}{\sqrt{1+ZT}+\frac{T_c}{T_h}} \quad (1.12)$$

Where the first term is the Carnot efficiency and ZT is the figure-of-merit of thermoelectric material. ZT is defined as (Snyder, 2008):

$$ZT = \frac{\alpha^2 \sigma T}{\lambda} \quad (1.13)$$

with α the Seebeck coefficient, σ the electrical conductivity, λ the thermal conductivity and T the temperature, which is the mean value of T_h and T_c.

According to eq. (1.12), the efficiency of a TEG is determined by ZT,T_h and T_c. Good efficiency is realized by high ZT with given T_h and T_c. From eq. (1.13) we see that the $\alpha^2\sigma$– called the power factor – must be large and λ small. In Fig. 1.3 these factors are compared as a function of free charge carriers. σ increases with carrier concentration, limited by mobility at high concentrations. α decreases with carrier concentration because it is inversely proportional to the carrier concentration. λ is approximately constant and determined by lattice scattering phenomena until at high concentrations charged carriers contribute to the increase in thermal conductivity. Metals have high σ, but low α while the thermal conductivity is high due to the electron contribution to the thermal conductivity λ_e. On the other hand, σ of insulators is low, α high and λ low. Insulators and metals are in general not seen as good thermoelectric materials. However, since the carrier concentration in semiconductors can be controlled via doping, an optimum in $\alpha^2\sigma$ can be achieved with relatively low thermal conductivity. When increasing the doping concentration further, λ will increase based on the Wiedemans-Franz law (Rowe,1995). Semiconductor can be good thermoelectric material, which with high ZT (Rowe, 1995).

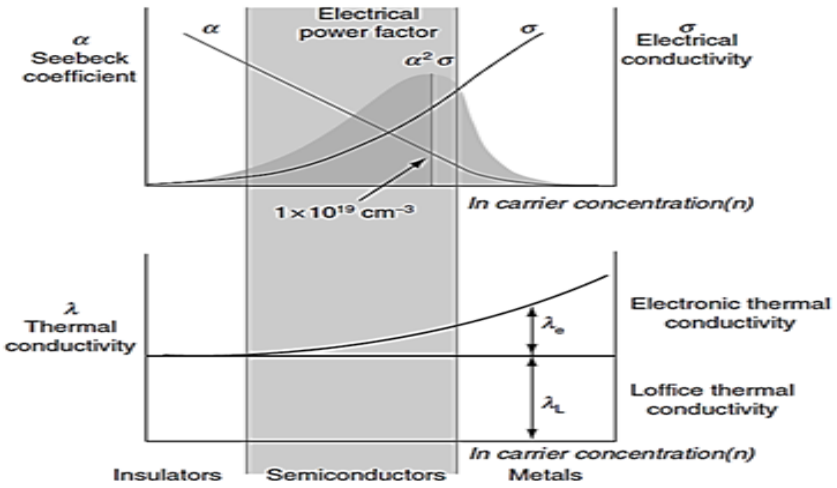


Figure 1.3: Thermoelectric properties of materials: Insulators have low $\alpha^2\sigma$ due to its pretty low σ; Metals also have low $\alpha^2\sigma$ due to its extremely low α; Semiconductor has highest $\alpha^2\sigma$ by controlling carrier concentration via doping, and it has relatively low λ (Rowe,1995).

The development and potential of bulk materials for thermoelectric applications is an active area of research. High-temperature bulk materials such as skutterudites, clathrates, half-Heusler alloys, and complex chalcogendies are being investigated. These materials possess complex crystal structures and exhibit properties that are favorable for potential thermoelectric materials. Recently, ceramic oxide materials have also shown potential as high temperature thermoelectric materials. Some of the goals of current research efforts are to find new materials that either raise the current efficiency of thermoelectric devices or have the capability of operating in new and broader temperature regimes, especially at lower temperatures (T<150K) and higher temperatures (T>400K). Over the past 30 years, alloys based on the Bi_2Te_3 system$[(Bi_{1-x}Sb_x)_2(Te_{1-x}Se_x)_3]$ and the $Si_{1-x}Ge_x$ system have been extensively studied and optimized for their use as thermoelectric materials (Minnich, Dresselhaus & Ren et al., 2009).

Bulk material applications are demanding new breakthroughs in thermoelectric applications. The potential of nano materials and their roles in thermoelectric research are an emerging area of interest due to the extremely low thermal conductivity of nano materials (Tritt & Subramanian, 2006).

Fig. 1.4 shows ZT as a function of temperature for BiSbTe, SiGe materials and their nanostructures as well as many of the more recent materials that have been developed over the past decades. At low temperatures (T<200K), BiSbTe has very good thermoelectric performance, and SiGe is an important thermoelectric material candidate at high temperatures (T>600K). Alloys based on PbSbTe system exhibits high ZT in the temperature range between 200K and 600K. Furthermore, nanostructures of these materials have much higher ZT in contrast to their bulk structures.

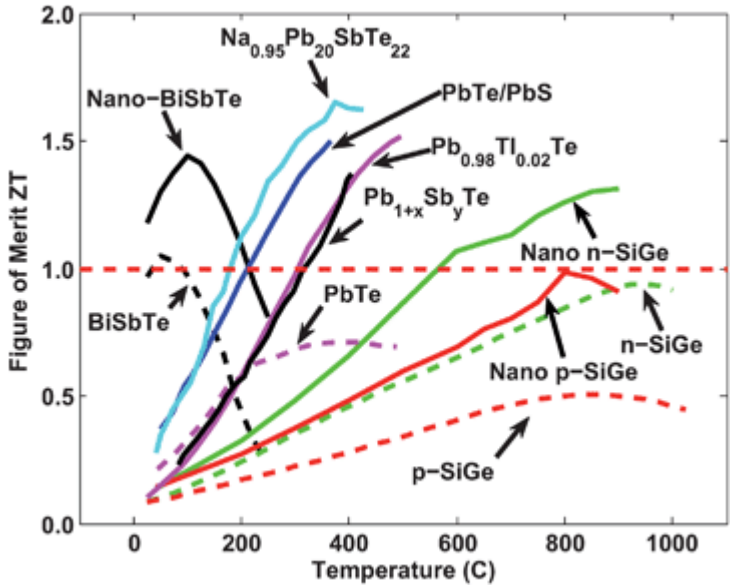


Figure 1.4: State of the art ZT values for a range of materials relevant to this research (Minnich, Dresselhaus & Ren et al., 2009).

1.4: Thermoelectric transport in a TEG

In this Section, we will present a theoretical output power model for a TEG which is composed of one thermoelectric material and two Cu blocks. We also will present the voltage and temperature distribution in thermoelectric material. The analysis is done in 1 dimension, thus heat losses to the environment are ignored.

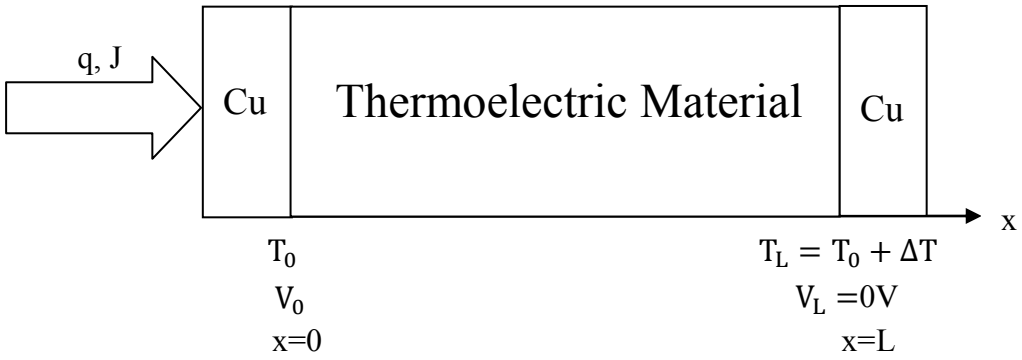


Figure 1.5: TEG structure and boundary conditions. J is the current density. q is the heat flux. V is the electrostatic potential and T the temperature.

In Fig. 1.5, a 1-D TEG structure with boundary conditions along the x-axis is given. We will ignore the Thompson effect as the temperature gradients across the samples remain small (P'erez-Aparicio, Taylor & Gavela, 2007),(Xu,Li&Thielemans et al.,2012).

The set of coupled differential equations that govern the thermo-electric transport is given by the following 4 equations (P'erez-Aparicio, Taylor & Gavela, 2007) ,(Xu,Li&Thielemans et al.,2012):

$$J = -\sigma_{TEG}\frac{dV}{dx} - \alpha\sigma_{TEG}\frac{dT}{dx} \quad (1.14)$$

$$q = \alpha TJ - \lambda\frac{dT}{dx} \quad (1.15)$$

$$\frac{dJ}{dx} = 0 \quad (1.16)$$

$$\frac{dq}{dx} + J\frac{dV}{dx} = 0 \quad (1.17)$$

J is the current density, V is the electrostatic potential, T is the temperature, q is the heat flux, σ_{TEG} is the effective electrical conductivity of TEG which takes account of thermoelectric material and the contact between Cu and thermoelectric material, λ the thermal conductivity and α is the Seebeck coefficient of thermoelectric material. Cu is ignored due to its extremely high electrical conductivity and thermal conductivity.

Rewriting eq. (1.14), gives:

$$\frac{dV}{dx} = -\frac{J}{\sigma_{TEG}} - \alpha\frac{dT}{dx} \quad (1.18)$$

When eq. (1.18) and eq. (1.15) are substituted into eq. (1.17), a second order differential in T(x) will be obtained:

$$\frac{d^2T}{dx^2} + \frac{J^2}{\lambda\sigma_{TEG}} = 0 \quad (1.19)$$

Integration with the boundary conditions shown in Fig. 1.5, gives:

$$T_{(x)} = \frac{J^2x(L-x)}{2\sigma_{TEG}\lambda} + \frac{\Delta Tx}{L} + T_0 \quad (0 \le x \le L) \quad (1.20)$$

When the first order differential of eq. (1.20) is substituted into eq. (1.14), a first order differential of V(x) will be obtained:

$$\frac{dV}{dx} = -\frac{J}{\sigma_{TEG}} - \frac{\alpha J^2 L}{2\lambda\sigma_{TEG}} + \frac{\alpha J^2 x}{\lambda\sigma_{TEG}} - \frac{\alpha\Delta T}{L} \quad (1.21)$$

Integrating with the boundary condition ($V_L = 0V$) shown in Fig 1.5, gives :

$$V_{(x)} = \left(\frac{J}{\sigma_{TEG}} + \frac{\alpha\Delta T}{L} - \frac{\alpha J^2 x}{2\lambda\sigma_{TEG}}\right)(L - x)(0 \le x \le L) \quad (1.22)$$

When eq. (1.20) and its first order differential equation are substituted into eq. (1.15), the expression of q(x) is found:

$$q_{(x)} = \alpha j\left[\frac{j^2x(L-x)}{2\sigma_{TEG}\lambda} + \frac{\Delta Tx}{L} + T_0\right] - \lambda\left[\frac{j^2(L-2x)}{2\lambda\sigma_{TEG}} + \frac{\Delta T}{L}\right](0 \le x \le L) \quad (1.23)$$

When the material is used as a TEG, the current density, J flows through the load resistance R_L when a temperature difference ΔT exists. Thus the final equation is

Ohm's law imposed on the load resistance R_L that relates current density to potential difference:

$$V_{(L)} - V_{(0)} = R_L JA \tag{1.24}$$

with A is TEG's cross section area.

If $V_{(L)}$ and $V_{(0)}$ are substituted into eq. (1.24), then the expression of J can be expressed as:

$$J = \frac{-\alpha\sigma_{TEG}\Delta T}{AR_L\sigma_{TEG}+L} \tag{1.25}$$

The output power is expressed as:

$$P = j^2A^2R_L = \frac{\alpha^2\sigma_{TEG}^2\Delta T^2A^2R_L}{A^2R_L^2\sigma_{TEG}^2+L^2+2AR_L\sigma_{TEG}^2L} = \frac{\alpha^2\sigma_{TEG}^2\Delta T^2R_L}{R_L^2\sigma_{TEG}^2+(\frac{L}{A})^2+2R_L\sigma_{TEG}(\frac{L}{A})} \tag{1.26}$$

If we assume, $\frac{L}{A}$ is fixed and the Seebeck coefficient remains constant, then the output power is mainly influenced by the temperature difference ΔT and the effective electrical conductivity σ_{TEG}. The temperature difference is a function of the thermal conductivity of thermoelectric material. Fig. 1.6 illustrates the dependence of the output power on electrical conductivity and temperature difference. The power versus load curves goes through a maximum. This point is reached when the load resistance is equal to the internal resistance of the TEG, which is equal to $L/(\sigma_{TEG}A)$. We notice that with increasing ΔT the maximum shifts only in amplitude while with a variation of the electrical conductivity, the maximum power varies in amplitude and also in position as the internal resistance is changing.

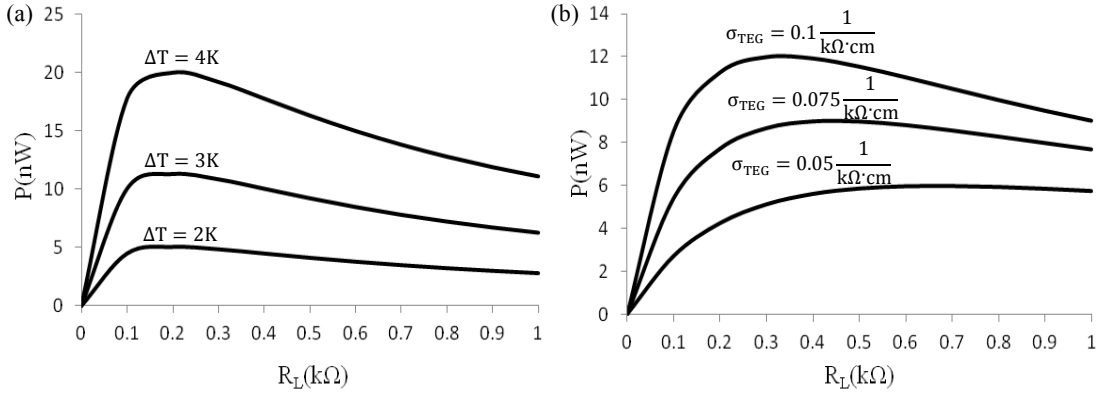


Figure 1.6: Simulated output power as a function of load resistance for a TEG (L=0.05cm, A=1.5cm^2). The α is assumed to be constant at 1mV/K. (a): Influence of temperature difference, $\Delta T = 2, 3$ and 4K, with $\sigma_{TEG} = \frac{1}{6}\frac{1}{k\Omega.cm}$; (b): Influence of electrical conductivity, $\sigma_{TEG} = 0.05, 0.075$ and $0.1\frac{1}{k\Omega.cm}$, with $\Delta T =$ 4K.

1.5:The Si nanowire arrays TEG

Currently, key constituents of commercial thermoelectric generators (TEGs), such as Bi, Te, As and Pb (see Fig. 1.4), are undesirable due to toxicity, rarity(He, Liu & Funahashi, 2011) and/or their primary sources being in politically sensitive regions. Research into alternative, non-toxic and abundant materials, that could substitute the classical ones in selected applications, is a key strategy to cope with future energy supply challenges. Si is ubiquitous, well known, widely available, used in a variety of well-established industries, is non-poisonous and stable at high temperatures. Si bulk however, has high thermal conductivity and is not appropriate for thermoelectricity. Si nanowires (NWs) have been suggested as an alternative material for thermoelectric energy generation. Data on single Si NWs show a figure-of-merit, ZT≈ 0.6 at T ≈ 300 K(Hochbaum, Chen & Delgado et al., 2008). The increase in ZT is attributed mainly to the reduction of λ due to phonon-boundary scattering (Mingo, Yang & Li et al., 2003) which becomes apparent at diameters less than ~100 nm.

The TEG structure we will investigate in this work is illustrated in Fig. 1.7. We will convert a part of the Si bulk into an array of vertically upstanding Si nanowires – Si nanowire arrays (NWAs).

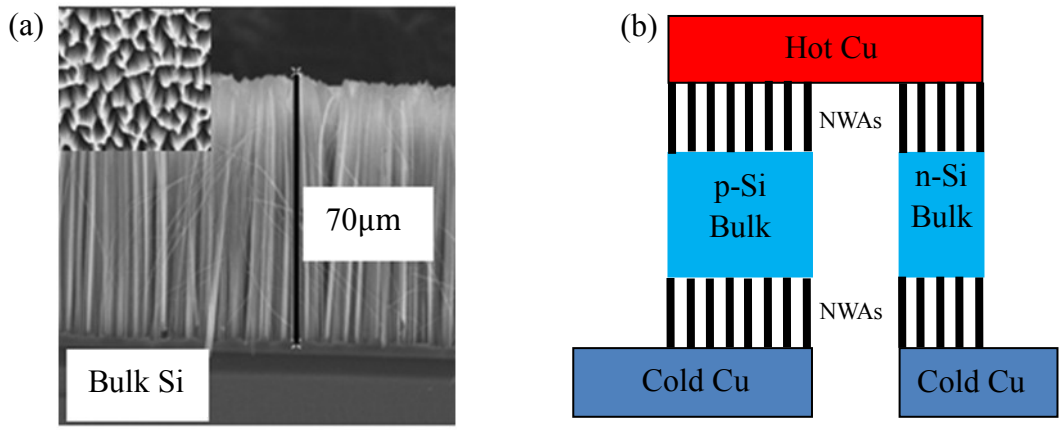


Figure 1.7: (a): SEM picture of a Si NWA's cross section view and top view (upper left). (b): Schematic of a possible Si NWA TEG.

$Si_{1-x}Ge_x$ alloy bulk and its nanostructure are also the options in our research due to their lower thermal conductivity which is caused by alloy structure. Furthermore, $Si_{1-x}Ge_x$ alloy bulk is also relatively easy to be gotten via reduced-pressure chemical vapor deposition. As the data given in Fig. 1.4, ZT of n-type $Si_{1-x}Ge_x$ alloy bulk almost reaches 1 at 950℃, and ZT of both p- and n-type $Si_{1-x}Ge_x$ nanostructure could reach 1 at high temperature. The thermoelectric characteristic of $Si_{1-x}Ge_x$ is much better than Si.

Due to the character of the NWAs TEG's, measurements can only be done by making an integrated circuit that includes thermocouples and voltage probe contacts via micro processing techniques or by sandwiching the NWAs between 2 Cu blocks to which the electrical contacts and the thermocouples are attached. In our work we have

chosen the second option to avoid the need for extensive micro fabrication development. However, in this solution we have to take the influence of thermal and electrical contact resistance into account (see Fig. 1.8).

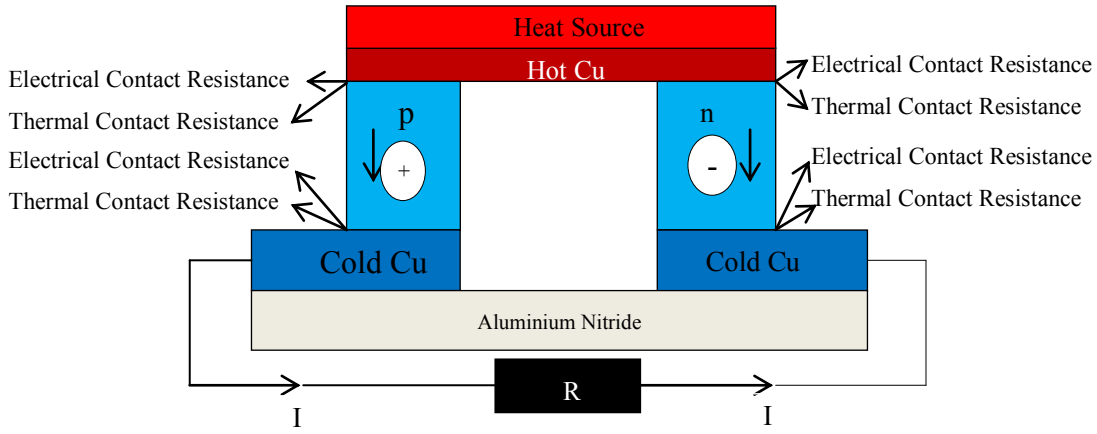


Figure 1.8: NWAs TEG between Cu blocks for measurements. Electrical and Thermal contact resistances are indicated on the sketch. Voltage and temperature are measured in the Cu blocks. Al_2N_3 is a thermal conductor and electrical insulator needed to keep the temperature the same in the two Cu blocks at the cold side (Snyder, 2008).

With respect to the analysis of the output power of a thermo element, these parasitic at the contacts will have to be taken into account.

Therefore the electrical conductivity σ_{TEG} in eq. (1.14) has to take the p-and n-type thermoelectric material's resistance as well as the two contact resistances to the Cu into account. In addition, a part of the temperature difference will drop across the thermoelectric material/Cu interface, decreasing the effective temperature difference across the thermoelectric material and reducing output power. From this simulation, we conclude that the output power is strongly influenced by the fabrication process of the contact, as well as the thermal conductivity and electrical conductivity of the thermoelectric material.

As analyzed before, ZT is an important parameter to characterize thermoelectric material. However, measuring ZT in our NWAs/bulk structures is a highly challenging task prone to large measurement errors. Therefore, ZT is not used to characterize the TEG's performance in our research. Instead, we use the output power as a function of load resistance with maximum heat flux by the heat source as the technique to compare different designs.

1.6: Conclusion

Within the thermoelectric generation community, the research is on to increase ZT of materials in order to improve the thermoelectric generation efficiency. Our research

aim is to investigate alternative materials that are sustainable and non-poisonous. Si has these characteristics but is a poor thermoelectric material because of its high thermal conductivity. Reports on single Si nanowires have shown that when Si bulk is converted to nanowires, the thermal conductivity decreases. We want to explore the feasibility of a TEG based on Si nanowires. In order to do this we convert part of a Si bulk into a Si NWAs. The studies of $Si_{1-x}Ge_x$ alloy bulk and its NWAs are also applied in our research due to its lower thermal conductivity. Characterizing these structures with non-continuous contacts and which a not capable to withstand shear strain is challenging. Therefore, the research has focused on different topics: the building of a set-up to measure the output power of the Si and $Si_{1-x}Ge_x$ NWAs; the study of the influence of the parasitic introduced by the set-up; the study of techniques to improve the thermoelectric performance of the TEGs.

1.7: Outlines of this thesis

The report is organized as follows after this introduction of thermoelectric generation.

Chapter 2 gives an overview of the literature which refers to the thermoelectric characteristics of Si NWs and $Si_{1-x}Ge_x$ alloy, TEG's output power based on NWs, NWs etching by metal assisted chemical etching (MACE) and some measurement techniques.

Chapter 3 describes the theoretical model of ZT, and TEG's output power which is significantly related to metal-semiconductor contact resistance which can be reduced sharply by spinning-on-doping.

Chapter 4 gives the experiments material characterizations which are used in our research by NWAs fabrication technique, spinning-on-doping and sputter coating.

Chapter5 describes the improvement of TEG's output power.

Chapter6 concludes the whole thesis.

Chapter7 lists future work.

Chapter 2: Literature overview and initial measurements

2.1: Introduction

As the key component of TEG in this research, the thermoelectric characteristics of Si and $Si_{1-x}Ge_x$ NWs, the thermoelectric performance of TEG based on Si NWs and the etching of Si and $Si_{1-x}Ge_x$NWs are reviewed in this chapter. Furthermore, the measurement techniques, which are used to characterize thermoelectric material's Seebeck coefficient, the Schottky barrier height and ideality factor of Cu-Si contact, as well as TEG's output power, are also reviewed in this Chapter.

2.2: Thermoelectric characteristics of Si NWs, SiGe alloy

Thermoelectric materials are qualified by ZT whose value of $ZT\sim1$ is necessary for practical applications (Krali & Durrani, 2013). Over the past five decades it has been challenging to increase ZT>1, since the parameters of bulk thermoelectric material's ZT are generally interdependent (Hochbaum, Chen & Delgado et al., 2008): an increase in α usually results in a decrease in σ, and a decrease in σ produces a decrease in the electronic contribution to λ, following Wiedemans-Franz law (Dresselhaus, Chen & Tang et al., 2007). Over the 3 decades from 1960 to 1990, only incremental gains were achieved in increasing ZT, with the $(Bi_{1-x}Sb_x)_2(Se_{1-y}Te_y)_3$ alloy family remaining the best commercial material with $ZT \approx 1$(Dresselhaus, Chen & Tang et al., 2007). While bulk Si, the most widely used semiconductor and the basis of large-scale integrated circuits, has a poor $ZT\sim0.01$, due to its high thermal conductivity $\lambda = 150W/(m \cdot K)$ at 300K(Krali & Durrani, 2013).

After 1990s, low-dimensional materials are taken as a solution to boost ZT of thermoelectric materials: firstly, the introduction of nanoscale constituents would introduce quantum confinement effects to enhance the power factor $\alpha^2\sigma$(Krali & Durrani, 2013); secondly, the thermal conductivity can be reduced due to more phonon scatterings without affecting electrical conductivity based on differences in the respective mean free path of phonons and electrons (Dresselhaus, Chen & Tang et al., 2007). For example, the measurements done on ZT of a single Si nanowire and ~100 Si nanowires in parallel have reported $ZT\sim1$ (Bouki,Bunimovich & Tahir-Kheli et al.,2008),(Hochbaum,Chen&Delgado et al., 2008). Hochbaum, Chen & Delgado et al., also demonstrates the Si nanowires with diameters of about 50nm exhibit 100-fold reduction in thermal conductivity, yielding ZT=0.6 at room temperature (Hochbaum, Chen & Delgado et al., 2008).

The low-dimensional thermoelectric materials use the quantum confinement phenomena to enhance α and to control α and σ somewhat independently

(Dresselhaus, Chen & Tang et al., 2007), (Bux, Fleurial & Kaner, 2010). Krali and Durrani have measured temperature dependence of α in an n-type Si sample with an area of $0.5 \times 0.5\text{cm}^2$ and a doping concentration of $\sim 10^{15}\text{cm}^{-3}$ consisting of $\sim 10^7$ vertically aligned NWAs with an average diameter of $\sim 250\text{nm}$ fabricated using MACE. At room temperature, α of bulk Si is about 0.75mV/K. α of Si NWAs whose length is $350\mu\text{m}$ is $\sim 1.9\text{mV/K}$ at room temperature (Krali & Durrani, 2013).

The many internal interfaces found in nanostructures would be designed so that λ would be reduced more than the σ, based on differences in their respective scattering lengths (Dresselhaus, Chen & Tang et al., 2007). The mean free path length of electrons is 110nm for heavily doped Si sample at room temperature, and $\sim 300\text{nm}$ for phonons (Feser, Sadhu & Azeredo et al., 2012). Furthermore, as the experiments done by Weisse, Marconnet & Kim (Weisse, Marconnet & Kim et al., 2012), the porosity of nanostructures is also a factor to affect λ.

Three kinds of Si NWs are prepared in Weisse, Marconnet & Kim et al.'s first experiment: nonporous Si NWs are formed by deep reactive ion etching (DRIE); two different kinds of porous Si NWs are fabricated by metal-assisted chemical etching (MACE), and the porosity is controlled by varying the metal catalyst and wafer doping concentration. For low-porosity nanowires, the catalyst layer consists of a 15-nm Ag film covered by 5-nm Au, while for the moderate to highly porous nanowires, a 50-nm Ag film is used as the catalyst and the initial wafer doping concentration is varied. The entire Si NWs diameter is between 300nm and 350nm. According to Weisse, Marconnet & Kim et al.'s measurement results, λ of the nonporous Si NWs is $142 \pm 13\text{W/(m} \cdot \text{K)}$, which is very close to that of bulk Si ($150\text{W/(m} \cdot \text{K)}$). λ of low-porosity nanowires is significantly reduced to $98\text{W/(m} \cdot \text{K)}$ and λ of moderate to highly porous nanowires is further reduced to $51\text{W/(m} \cdot \text{K)}$. The diameter of Si NWs is bigger than phonon mean free path, but the thermal conductivity of Si NWs can be reduced significantly with increasing porosity (Weisse, Marconnet & Kim et al., 2012).

Weisse, Marconnet & Kim et al.'s second experiment demonstrates λ of Si NWs with small diameters $\sim 130\text{nm}$ also decrease with increasing porosity, similar to the large-diameter Si NWs whose diameter is between 300nm and 350nm. However, λ of these small diameter Si NWs is much smaller than that of large diameter Si NWs of similar porosities. Specifically, λ is reduced from $51\text{W/(m} \cdot \text{K)}$ for the large-diameter ($\sim 350\text{nm}$) Si NWs to $28\text{W/(m} \cdot \text{K)}$ for the smaller-diameter ($\sim 130\text{nm}$) Si NWs under the same porosity. This highlights the significant impact of phonon-external boundary scattering on the thermal conductivity at length scales that are smaller than the phonon mean free path. The additional reduction in λ(to$17\text{W/(m} \cdot \text{K)}$) with increasing H_2O_2 concentration in the MACE solution for the smaller-diameter Si NWs indicates that the increasing internal porosity also has a significant impact on λ(Weisse, Marconnet & Kim et al., 2012).

Hochbaum, Chen & Delgado et al.'s research results illustrate λ of Si NWs with different diameters which are prepared by vapour liquid solid (VLS) and MACE respectively. The measured λ of both VLS and MACE Si NWs are strongly diameter-dependent, which is attributed to boundary scattering of phonons. They also find that the magnitude of λ is five-to eightfold lower for MACE nanowires of comparable diameters, because roughness at the MACE nanowire surface behaves like secondary scattering phases, and the roughness may contribute to higher rates of diffuse reflection or backscattering of phonons at the interfaces. Furthermore, they find that λ of Si NWs firstly increases with increasing temperature, and then decreases with increasing temperature. For VLS Si NWs, the temperature of peak $\lambda(\sim 45\mathrm{W}/(\mathrm{m}\cdot\mathrm{K})$ with diameter of 115nm) is 175-200K, while that ($\sim 10\mathrm{W}/(\mathrm{m}\cdot\mathrm{K})$ with diameter of 115nm) of MACE Si NWs is above 250K, and both are significantly higher than that of bulk Si, which peaks at around 25K. This shift suggests that the phonon mean free path is limited by boundary scattering as opposed to intrinsic Umklapp scattering (Hochbaum, Chen & Delgado et al., 2008).

Dismukes, Ekstrom & Steigmeier et al. describe the detailed investigation of the thermal properties of $\mathrm{Si_{1-x}Ge_x}$ alloys as a function of composition, doping impurity additions, and temperature, and the optimization of the material for TEG. They measured the thermal resistivity of two kinds of p-type $\mathrm{Si_{1-x}Ge_x}$ alloys ($\mathrm{Si_{0.7}Ge_{0.3}}$ and$\mathrm{Si_{0.85}Ge_{0.15}}$) as a function of temperature and carrier concentration: (1): with the increase of temperature, their thermal resistivity firstly increases, and then decreases. The temperature corresponds to peak thermal resistivity is between 1000K and 1100K; (2): with the increase of carrier concentration, their thermal resistivity firstly increases, and then decreases. The carrier concentration corresponds to peak thermal resistivity is $\sim 2\times 10^{20}\mathrm{cm}^{-3}$ at room temperature; (3): the thermal resistivity of $\mathrm{Si_{0.7}Ge_{0.3}}$ is slightly higher than that one of $\mathrm{Si_{0.85}Ge_{0.15}}$ under the same temperature and carrier concentration; (4): the thermal resistivity of $\mathrm{Si_{0.7}Ge_{0.3}}$ alloy with carrier concentration of $3.5\times 10^{20}\mathrm{cm}^{-3}$ under room temperature is about $18.2(\mathrm{cm}\cdot\mathrm{K}/\mathrm{W})$, and the thermal resistivity for $\mathrm{Si_{0.85}Ge_{0.15}}$ alloy under the same condition is about $17.5(\mathrm{cm}\cdot\mathrm{K}/\mathrm{W})$. The thermal resistivity of Si bulk at room temperature is $\sim 0.667(\mathrm{cm}\cdot\mathrm{K}/\mathrm{W})$, which is much lower than the one of $\mathrm{Si_{1-x}Ge_x}$ alloys. They also measured the Seebeck coefficient of two kinds of p-type $\mathrm{Si_{1-x}Ge_x}$alloys ($\mathrm{Si_{0.7}Ge_{0.3}}$ and$\mathrm{Si_{0.85}Ge_{0.15}}$) as a function of temperature and carrier concentration: (1): their Seebeck coefficients all increase with increasing temperature which is from 300K to 1100K; (2): the trend of the relation between their Seebeck coefficients and temperature is the same as the one of Si bulk: Seebeck coefficients decreases with increasing carrier concentration for the same kind of $\mathrm{Si_{1-x}Ge_x}$alloys under the same temperature; (3):the fraction of Ge or Si cannot affect the Seebeck coefficient of $\mathrm{Si_{1-x}Ge_x}$ alloys (Dismukes, Ekstrom & Steigmeier et al., 1964).

As the literatures reviewed in this section, thermoelectric characteristic of Si can be improved by introducing Si NWs via the reduction of thermal conductivity which is caused by more phonon scatterings and the increase of Seebeck coefficient which is

caused by quantum confinement. Thermoelectric characteristic also can be improved by introducing $Si_{1-x}Ge_x$ alloys due to its much lower thermal conductivity which is also caused by more phonon scattering, but its Seebeck coefficient is not increased compared with Si under the same condition.

2.3: Thermoelectric generator based on NWs

The thermoelectric characteristics of Si NWs have been analyzed from the aspects of its α and λ in Section 2.2. While efficient thermoelectric devices must consist of dense arrays of Si NWs that are fabricated with conventional processing methods, and thermoelectric devices' characteristics also can be valued by its output power.

Curtin & Bowers fabricated Si NW arrays directly from bulk Si wafers by reactive-ion etching, and then spin-on glass (SOG) was chosen as the matrix material in which the vertical Si NW array embedded in. ZT of the NW/matrix composite material is:

$$ZT_{comp} = ZT_{NW} / \left\{1 + \frac{\lambda_{matrix}}{\lambda_{NW}} \left[\frac{1}{f_{NW}} - 1\right]\right\} \quad (2.1)$$

With ZT_{NW} the ZT of individual NWs, λ_{matrix} and λ_{NW} are the matrix and NW thermal conductivity and f_{NW} is the NW packing density (Curtin & Bowers, 2012).

As the matrix material, glass is with extremely low λ_{matrix} which can boost ZT_{comp}

In addition, Curtin & Bowers also verified the value of λ_{NW} in his experiment by the equation:

$$\lambda_{NW} = f_{NW}^{-1}[\lambda_{comp} - (1 - f_{NW})\lambda_{SOG}] \quad (2.2)$$

The measured λ_{comp} is $\sim 1.45 W/(m \cdot K)$ from 300K to 450K. f_{NW} is $\sim 15\%$ and λ_{SOG} is $0.39 W/(m \cdot K)$ .Therefore, λ_{NW} is $\sim 7.5 W/(m \cdot K)$ at 300K which corresponds to a $16\times$ decrease over bulk Si and a $5\times$ decrease over VLS etched Si NWs with similar diameter which is between 80nm and 90nm. Furthermore, Curtin & Bowers measured the output power of the $50\mu m \times 50\mu m$ combined Si NW/SOG composite film and substrate device which generated $29.3\mu W$ output power with a ΔT of 56K (Curtin & Bowers, 2012). At this temperature, the open circuit voltage and short circuit current were measured to be $17.05mV$ and $6.87mA$, respectively(Curtin & Bowers, 2012).

Li, Buddharaju & Tinh et al. have also fabricated a thermoelectric power generator with polyimide as matrix material. A matrix material is essential to mechanically support the high-aspect-ratio Si NWs which was fabricated using DUV lithography, resist trimming, and Si dry etch process. As the heat flux needs to be channeled

preferentially through the Si NWs over the matrix material, a matrix material of low λ, ideally zero (vacuum), is desired. Polyimide whose λ is $0.14\mathrm{W/(m\cdot K)}$ is chosen as matrix material in this research, and the other reason is its compatibility with CMOS processing during fabrication. The fully fabricated TEG is with Si NWs of diameter~80nm, and a height of $\sim 1\mu\mathrm{m}$. The completed device had a Si NWs array of size $5\mathrm{mm}\times 5\mathrm{mm}$. Consequently, an open-circuit voltage of 27.9mV, a short-circuit current of $67\mu\mathrm{A}$, and a maximum power output of $0.47\mu\mathrm{W}$ were obtained under a temperature difference of 70K across the experimental setup. If the matrix material is replaced by SiO_2 whose λ is $1.4\mathrm{W/(m\cdot K)}$, the open-circuit voltage is 1.5mV, a short-circuit current of $3.79\mu\mathrm{A}$, and a maximum power output of $0.0015\mu\mathrm{W}$ were obtained under the same temperature difference(Li, Buddharaju & Tinh et al., 2012).

Davila, Tarancon & Calaza et al. proposed a thermoelectric micro generator (μTEG) which is based on an architecture consisting of a thermocouple with a leg of p-type Si NW array (acting as nanostructure thermoelectric material) grown by the CVD-VLS mechanism and another one of tungsten. This architecture is usually referred to as 'uni-leg' since only a single polarity semiconductor is used as thermoelement. The Si NWs physically connect the high and low temperature areas. The TEG's output power density increases with the quantity of Si NWs array. A maximum Seebeck voltage of $4.4\mathrm{mV}$ and a power density of $9\mu\mathrm{W/cm^2}$ were measured for 9 arrays of Si NWs when placed on a heat source at $300℃$ with $\Delta\mathrm{T}=27℃$. In order to test the full extent of the potentiality of the μTEG as energy harvesters, the heater was employed to evaluate the performance when the structures were subjected to higher temperature differences: a maximum Seebeck voltage value of $58\,\mathrm{mV}$ and a maximum power density of $1.44\mathrm{mW/cm^2}$ were measured as a temperature difference of $300℃$(Davila, Tarancon & Calaza et al., 2012).

Si NWs are the first option to fabricate TEG due to the broad existence of Si, as well as the Si NWs' great thermal characteristic. As the literatures reviewed in this section, Si NWs are embedded in a matrix material which is with extremely low thermal conductivity in order to boost and TEG's output power.

2.4: Metal assisted chemical etching

Nanoscale Si and $Si_{1-x}Ge_x$ have attracted considerable interests due to their potential to impact broad application areas ranging from electronics, photonics, and renewable energy to biomedical sensing. Significant efforts have been devoted to develop new Si and $Si_{1-x}Ge_x$ nanostructures, including quantum dots, nanowires (NWs), or porous Si. Si and $Si_{1-x}Ge_x$ NWs in particular have been the focus of intensive research over the past decade due to their unique one-dimensional physical morphology and the associated electrical, mechanical, and thermal properties (Li, Qian & Xiang et al.,

2006), (Qu, Liao & Li et al., 2009). In our application, we are concerned with the low thermal conductivity property of Si and $Si_{1-x}Ge_x$ NW arrays (NWAs).

Currently, different methods have been utilized to produce Si NWAs, such as laser ablation, thermal evaporation, chemical vapor deposition, molecular beam epitaxy, chemical etching, and solution growth (Hazra & Chakrabarti et al.,2012). However, repeatable and controllable preparation of Si NWAs epitaxial from substrate with defined type, orientation, and doping level is still a challenge (Zhang, Peng & Fan et al., 2008). Metal assisted chemical etching (MACE) is the Si and $Si_{1-x}Ge_x$ NWAs etching method used in our research. MACE was first developed by Peng et al. in 2003 (Peng, Yan & Gao et al., 2003) and then further adapted by different research groups (Huang, Geyer & Werner et al., 2011).

In general, MACE can be classified into two types: a one-step reaction in an etchant containing HF and metal salts and a two-step reaction that involve the pre-deposition of metal nanoparticles (NPs) or patterned metal thin films, followed by chemical etching in the presence of HF and H_2O_2(Zhang, Peng & Fan et al., 2008).

1: One-step reaction
Usually, the metal salt used in the etchant is $AgNO_3$(Peng, Wu & Fang et al., 2005). The 'growth' mechanism for Si NWAs is shown in Fig. 2.1. The global chemical reaction can be formulated as in eq. (2.3), which can be separated into two half-cell reactions, shown in eq. (2.4) (Peng, Yan & Gao et al., 2003).

$$4Ag^+ + Si + 6F^- \rightarrow 4Ag + SiF_6^{2-} \tag{2.3}$$

$$\begin{aligned} Ag^+ + e^- &\rightarrow Ag \\ Si + 6F^- &\rightarrow SiF_6^{2-} + 4e^- \end{aligned} \tag{2.4}$$

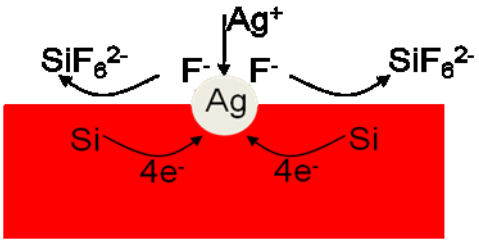


Figure 2.1: Growth mechanism for Si NWAs (Peng, Yan & Gao et al., 2003).

The process can be explained as follows: at the start, the Si etching and Ag deposition occur simultaneously at the Si surface; the deposited Ag atoms from nanoclusters acting as local cathodes and the areas surrounding these nanoclusters act as anodes. That is to say, numerous nanosized electrochemical cells self-assemble on the surface of the Si wafer. Generally, the metal nanoclusters have a strong tendency to coalesce and form continuous grain film in the process of electroless metal deposition. However, in the case of the HF- $AgNO_3$ system, the simultaneous growth of a mass of Ag dendrites effectively holds back the coalescence of Ag nanoclusters by consuming

large quantities of superfluous deposited Ag atoms, so those free-standing nanoscales electrolytic cells were successfully preserved (Peng, Yan & Gao et al., 2003).

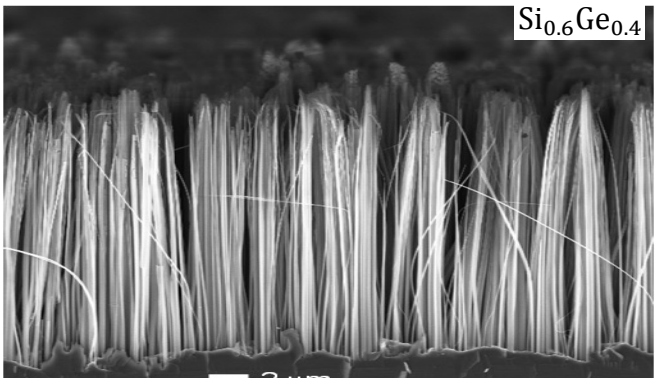


Figure 2.2: $Si_{0.6}Ge_{0.4}$ NWs which are prepared by one-step MACE.

Different parameters influence the one-step etching process:

1. The etching temperature affects the surface morphology of etched Si wafer, high etching temperature can increase the etching speed and lead to disorder of surface microstructure (Peng, Yan & Gao et al., 2003).
2. The etching time and concentration of Ag^+ also affect the etched structures. When the sample is prepared with a low concentration of Ag^+ and short etch time, only porous microstructures can be obtained. They can be seen as non-free-standing Si NWs. These porous microstructures can evolve into free-standing Si NWs by enhancing etching time or concentration of Ag^+ in the etch solution. Then a high density of NWs are freely arrayed on the Si substrate if the concentration of Ag^+ is sufficiently high. Increasing the etch time or concentration of Ag^+ further, normally leads to removal of Si NWs or the formation of disordered microstructures(Peng, Yan & Gao et al., 2003). Therefore, etching time and concentration of Ag^+ always have to be optimized to obtain good NWs.
3. If NH_4F is used to substitute HF, only micrometer-sized Ag grain film was grown on the surface of Si substrate, and no Ag dendrite could be observed. The Si substrate was uniformly etched and no pits could even be observed when removing the Ag film from Si substrate. This means that the presence of HF in the solution is a key factor in the formation of Si NWs (Peng, Yan & Gao et al., 2003).

In order to clarify the role of Ag^+ in the 'growth' of the Si NWs, other oxidizing agents with different metal species were also added into the aqueous HF. When Ag^+ ions are replaced by $Fe^{3+}, Mn^{2+}, Ni^{2+}, Co^{2+}, Cr^{2+}$ and Mg^{2+} ions, no metal deposition could occur because the equilibrium potentials of these metal ions are lower than that of hydrogen in the present experimental system. If Si samples are prepared in aqueous HF solution containing $Cu(NO_3)_2$ or K_2PtCl_6, continuous metal grain films are always found on the surface of the Si substrate, but no metallic dendrites. Many shallow pits can be observed when these metal grain films were removed from the substrate. However, no Si NWAs are observed (Peng, Yan & Gao et al., 2002), (Peng, Yan & Gao et al., 2003).

One-step reaction is used to etch SiGe NWAs in our research. The etching rate is slow

and reduces quickly with increasing Ge composition and etching time. For p-type $Si_{0.8}Ge_{0.2}$ NWAs, the etching rate is 0.4 μm/min in 15 minutes under room temperature with the recipe described in Section4.2.2. The etching rate for p-type $Si_{0.7}Ge_{0.3}$ NWAs and p-type $Si_{0.6}Ge_{0.4}$ NWAs are 0.27μm/min and 0.13μm/min respectively under the same circumstance. One-step reaction is successfully used to etch the SiGe layer fully (thickness=6μm) in our research.

2: Two-step reaction

In the two-step reaction, the pre-cleaned Si wafers are immersed into a buffered oxide etchant to remove the native oxide layer and then immediately transferred into an Ag deposition solution containing HF and $AgNO_3$. The color of the surface changes from dark to colorful, indicating the formation of Ag NPs on the surface of Si wafers. The Ag-deposited Si is rinsed in deionized water to remove extra Ag ions and then immediately soaked into an etchant bath composed of HF and H_2O_2(Qu, Liao & Li et al., 2009). The growth mechanism is shown in Fig. 2.3and Fig. 2.4(Peng, Wu & Fang et al., 2005), (Zhang, Peng & Fan et al., 2008).

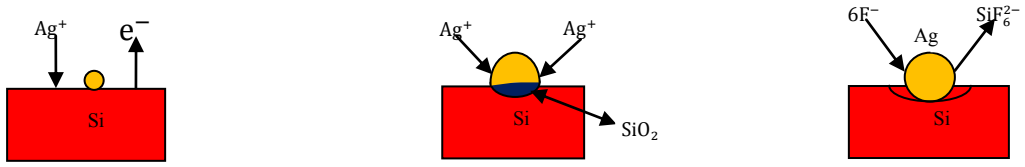


Figure 2.3: Electroless Ag deposition (Peng, Wu & Fang et al., 2005), (Zhang, Peng & Fan et al., 2008).

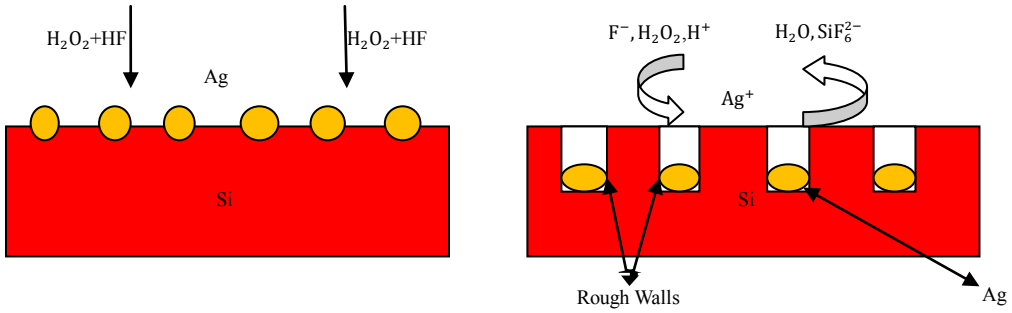


Figure 2.4: Electrochemical anodic dissolution of Si (Peng, Wu & Fang et al., 2005), (Zhang, Peng & Fan et al., 2008).

Fig. 2.3 illustrates the electroless deposition of Ag NPs on Si in the HF- $AgNO_3$ solution: SiO_2 forms simultaneously underneath the Ag particles while pits form as a result of etching the SiO_2 in HF solution. The chemical reaction is shown in eq. (2.5) (Zhang, Peng & Fan et al., 2008).

$$4Ag^+ + Si + 6F^- \rightarrow 4Ag + SiF_6^{2-} \qquad (2.5)$$

Fig. 2.4 illustrates the electrochemical anodic dissolution of Si in the HF-H_2O_2 solution. The left graph of Fig. 2.4 shows the starting point. Ag is coated on the surface of Si wafer by the reaction eq. (2.5). The Ag is oxidized immediately and partially dissolved in solution to form Ag^+ ions once the wafer is put into an etchant

containing HF and H_2O_2, the chemical reaction is shown in eq. (2.6)(Zhang, Peng & Fan et al., 2008).

$$2Ag + H_2O_2 + 2H^+ \rightarrow 2Ag^+ + 2H_2O \quad (2.6)$$

The Ag^+ ions quickly react with the Si by the reaction shown in Fig. 2.3, so the etching is localized in the regions covered by Ag NPs. Hence, the Si forms Si NWAs. The net etching reaction of these two steps is shown in eq. (2.7) (Zhang, Peng & Fan et al., 2008).

$$Si + 2H_2O_2 + 6F^- + 4H^+ \rightarrow SiF_6^{2-} + 2H_2O \quad (2.7)$$

The net etching reaction shown in eq. (2.7), in which H_2O_2 and HF diffuse into the pores and SiF_6^{2-} and H_2O is released.

With the continuous etching reaction, the Ag NPs sink deeper. Meanwhile, some Ag+ ions formed by the reaction shown in eq. (2.6) diffuse out. So the Ag NPs become smaller, which leads to the formation of gradient in NW width and rough pore walls. In addition, when the concentration of the diffused Ag+ ions reaches a certain value, it will etch the sidewalls of the NWs (Zhang, Peng & Fan et al., 2008). Thus, the quality of Si NWAs is closely related to the etch solution recipe, the etch temperature and time.

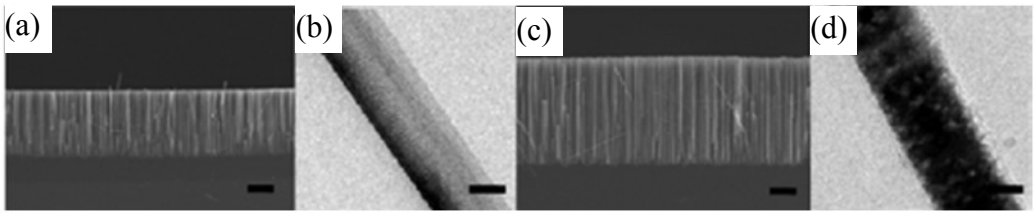


Figure 2.5: SEM and TEM images show the evolution of Si NWs morphology from n-type Si(100) with $0.008 - 0.02\Omega \cdot cm$ resistivity in etchant solution composed of 4.8 M HF and 0.2 M H_2O_2 for 30 min (a and b) and 60 min(c and d). NWs length increases with increasing etching time, and NWs are more porous with longer etching time due to Ag NPs become smaller and smaller in the etching process (Qu, Liao & Li et al., 2009).

As shown in Fig. 2.3 and 2.4, the Ag NPs catalyze the reaction around and below them and thus create nanopits that confine the Ag NPs. Thus this confines the etching reaction in the nanopits and ensures the etching is predominantly along the vertical direction. The initial nucleation of Ag NPs may preferentially occur near defective sites (e.g. around the dopants) where the energy barrier for the redox reaction is lower. Thus, heavily doped Si bulk tends to have a too high density of nucleated Ag NPs on the surface that are in close proximity of each other, and each NPs may not be effectively confined within its own pits. Additionally, the existence of many defects (near the dopants) and the availability of a large amount of Ag ions in the solution may facilitate the deposition of Ag NPs on the side walls of the NWs and create new lateral etching pathways. On the basis of these two arguments, the amount of Ag ions in the solution must be controlled (Qu, Liao & Li et al., 2009). As shown in Fig. 2.4,

the NW diameter is determined by the distance between two adjacent nanopits, so also by the distance between two adjacent Ag ions. The distance of two adjacent Ag ions will become bigger if the Ag ions' concentration is decreased, so that the diameter of NWs also becomes bigger.

It is found that the concentration of H_2O_2 has a big influence on the morphology of the Si NWAs. Higher concentration of H_2O_2 produces a lower density Si NWs, increasingly rough surface and eventually porous NWs. Increased H_2O_2 concentration increases the driving force for the etching reaction. Hence, the reaction becomes faster, so more Si dissolves. Therefore, the density of Si NWs decreases with increasing concentration of H_2O_2. In addition, as the H_2O_2 concentration increases, the concentration of Ag+ ions increases. In this case, the Ag+ ions may not be 100% recovered into the original Ag NPs and some may diffuse out. When the amount of the out-diffused Ag+ ions reaches a certain threshold, these Ag+ ions may start to nucleate on the NWs forming new Ag NPs for a new etching pathway along the lateral direction which explains the increased porosity with increasing H_2O_2(Zhang, Peng & Fan et al., 2008), (Qu, Liao & Li et al., 2009).

The Si NWs become rougher, shorter and sparser with higher etching temperature. Furthermore, the reaction rate increases with increasing reaction temperature, but the fast reaction rate enhances the chance of random etching (Zhang, Peng & Fan et al., 2008).

It is also found that the etching time mainly affects the length and the order of the Si NWs, longer and more ordered Si NWs are obtained with longer etching time however only in the presence of a sufficient amount of Ag NPs (Zhang, Peng & Fan et al., 2008).

The etching rate for both n-type(1-10$\Omega \cdot$ cm)and p-type(1-5$\Omega \cdot$ cm) Si NWAs is about $1\mu m/min$ at room temperature with the recipe described in the Part 1 of Section 4.1.2 in 45 minutes, and the etching rate becomes slower with increasing etching time. The longest Si NWAs gotten in our research is $300\mu m$ by Dr. Chuanbo Li.

The feature of preferential Ag NPs nucleation on defects might also influence the etching of NWAs in $Si_{1-x}Ge_x$. In addition, Ge is removed by H_2O_2. Therefore, we found that in order to etch $Si_{1-x}Ge_x$ NWAs one-step MACE is used. More details on our changes to the NWAs etching recipe will be discussed in Chapter 4.

2.5: Measurement techniques

This section describes the set-up for measuring the thermoelectric material properties and the output power of the TEG's. It presents the classical approach and highlights the challenges imposed by the Si NWAs.

2.5.1: Seebeck coefficient measurement

Traditionally, the Seebeck coefficient is measured on bulk material in a set-up proposed by T. Tritt and given in Fig. 2.6 (a) (Rowe, 1995).The sample is placed between two Cu blocks. The temperature difference is measured via 2 Cu blocks and the voltage is measured via the sample itself directly. However, due to the fact that our sample is thin (~500μm) and consist of fragile NWAs, contact wires cannot be connected directly to the sample. Cu blocks, which are good thermal and electrical conductors, are used to take the external leads to measure the temperature drop and voltage across the structure, as shown in Fig. 2.6 (b). The sample is clamped between two Cu blocks with little holes, which are ~1 mm from the Cu surfaces, for the connections to the voltmeter and the thermometer. The cold side is placed on a finned heat sink to improve heat dissipation. The heater is a power resistor from Vishay (Model: RH025) (Vishay, 2014). The weight scale used to measure the pressure given by the screw is from Hanson (Model: HX5000) (Amazon.co.uk, 2014). The Cu leads from the Cu blocks are attached to a Keithley 2000 voltmeter (Keithley.com, 2014) to measure the voltage difference ΔV and Cu/constantan thermocouples are connected to a Fluke52II digital thermometer to measure the temperature difference ΔT (Myflukestore.com, 2014). A 10 cm×10 cm black metal heat sink with cooling fins is used to cool the cold side. The sides of the TEG structure are insulated with a 0.5 cm thick layer of polystyrene insulator and the setup is placed in a glove box at atmospheric pressure and room temperature to prevent influences from external air flow variations. The Seebeck coefficient α is extracted from the open circuit voltage ΔV versus ΔT measurements.

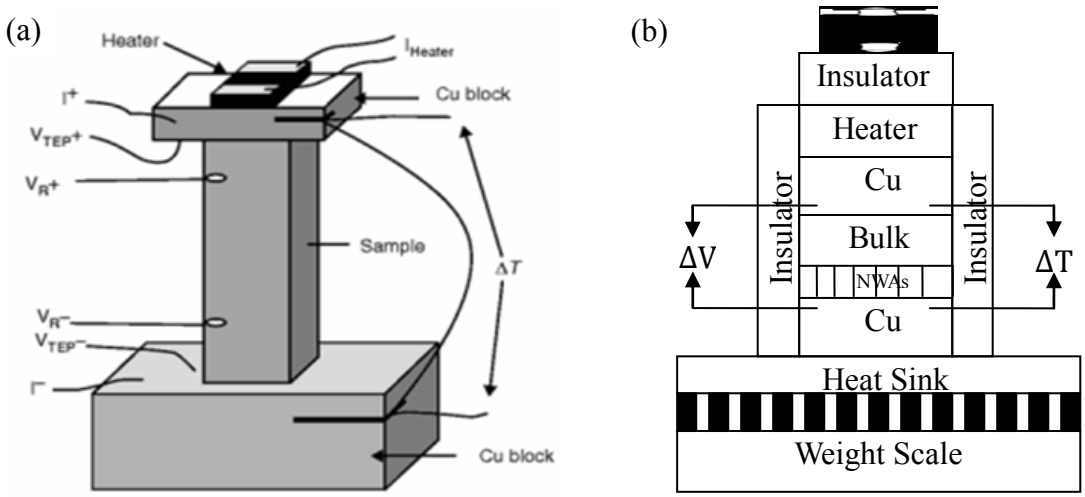


Figure 2.6: (a) Tritt's Seebeck coefficient measurement set-up (Rowe, 1995), (b) Seebeck coefficient measurement set-up used in our research.

According to the Seebeck coefficient model which will be described in Section 3.1.1, the theoretical Seebeck coefficient of lightly doped Si/SiGe bulk, which is given in Fig. 3.1, is ~1.1mV/K within a temperature range between 300 K and 350 K, consistent with the experimental temperature range in our research. The measured

Seebeck coefficient of the Si/SiGe NWAs (5 μm long), which are etched from the $Si_{0.8}Ge_{0.2}$layer, is $\sim 0.24 mV/K$ under a pressure of $\sim 150\,N$ which is imposed by the screw. Obviously, this value is much smaller than theoretically expected. This lower value can be attributed to the thermal contact resistance that occurs between the Cu block and the Si/SiGe sample due to the surface roughness of Cu and Si/SiGe sample.

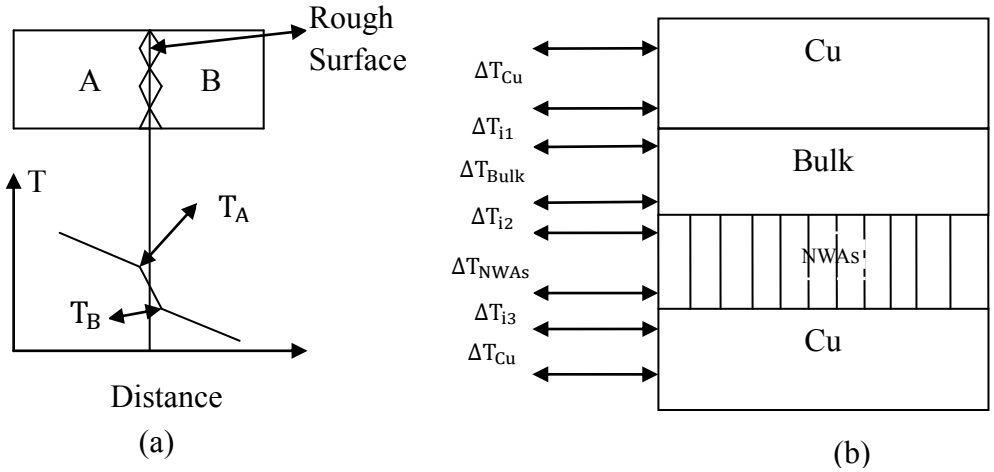


Figure 2.7 (a): Rough surfaces contact and temperature drop (Chapman, 1987). (b) Temperature drops in the Seebeck coefficient measurement set-up.

As given in Fig. 2.7 (a) (Chapman, 1987), a sudden temperature drop occurs at the contact interface (Cooper, Mikic & Yovanovich, 1969). As shown in Fig. 2.7 (b), the temperature difference in our measurements includes three components: the temperature drop across Cu (ΔT_{Cu}), the temperature drop at the interfaces ($\Delta T_{i1}, \Delta T_{i2}$ and ΔT_{i3}) and the temperature drop across sample (ΔT_{Bulk} and ΔT_{NWAs}). Therefore, the total temperature difference that we measure is given by eq. (2.8).

$$\Delta T = 2\Delta T_{Cu} + \Delta T_{Bulk} + \Delta T_{NWAs} + \Delta T_{i1} + \Delta T_{i2} + \Delta T_{i3} \qquad (2.8)$$

Thus the measured Seebeck coefficient is:

$$\alpha_{measurement} = \frac{\alpha_{real}(\Delta T_{Bulk}+\Delta T_{NWAs})}{2\Delta T_{Cu}+\Delta T_{Bulk}+\Delta T_{NWAs}+\Delta T_{i1}+\Delta T_{i2}+\Delta T_{i3}} \qquad (2.9)$$

Where $\Delta T_{Bulk} + \Delta T_{NWA} = \Delta T_s$ and $\Delta T_{i1} + \Delta T_{i2} + \Delta T_{i3} = \Delta T_i$.This shows that the measured Seebeck coefficient ($\alpha_{measurement}$) is always smaller than the real Seebeck coefficient (α_{real}). Re-writing eq. (2.9) gives:

$$\alpha_{measurement} = \frac{\alpha_{real}\Delta T_s}{2\Delta T_{Cu}+\Delta T_s+\Delta T_i} = \frac{\alpha_{real}}{1+\frac{2\Delta T_{Cu}}{\Delta T_s}+\frac{\Delta T_i}{\Delta T_s}} \qquad (2.10)$$

This equation shows that if the temperature drop across the sample (ΔT_s) is much larger than that across the Cu (ΔT_{Cu}) and interfaces (ΔT_i), then the measured value is close to the real value of Seebeck coefficient. Among them, ΔT_{Cu} can be ignored due to its high thermal conductivity and the small distance between the thermocouple probe and the Cu/sample surface. In order to reduce the errors due to the interface temperature drop, two changes have been made to the set-up that minimizes these drops: (1) applying a high pressure at the interface, and (2) using a soft interstitial

material (Ag foil) (Khounsary, Chojnowski & Assoufid et al., 1997).

1: High pressure at the interface
The pressure at the interface is controlled by the screw and measured by the weight scale. The influence of pressure on the extracted value of the Seebeck coefficient for the same Si/SiGe NWAs is given in Fig. 2.8 (a). The measured value of the Seebeck coefficient increases with increasing pressure because the temperature drop across the interface decreases. The pressure is limited to 250 N to prevent the collapse of the NWAs.

2. Soft interstitial material (Ag foil).
A thin layer (~0.25 mm) of Ag foil is malleable and a good thermal conductor. Adding Ag foil between semiconductor and Cu decreases the thermal contact resistance. The results of the measurements, on the same Si/SiGe NWA sample, are given in Fig. 2.8 (b). These measurements show that ΔT is higher when no Ag foil is used. The difference between ΔT without (x) and with (+) Ag foil is lost across the contact interface. Fig. 2.8 (b) shows that approximately 50% of ΔT is lost across the interfaces at high heater power levels.

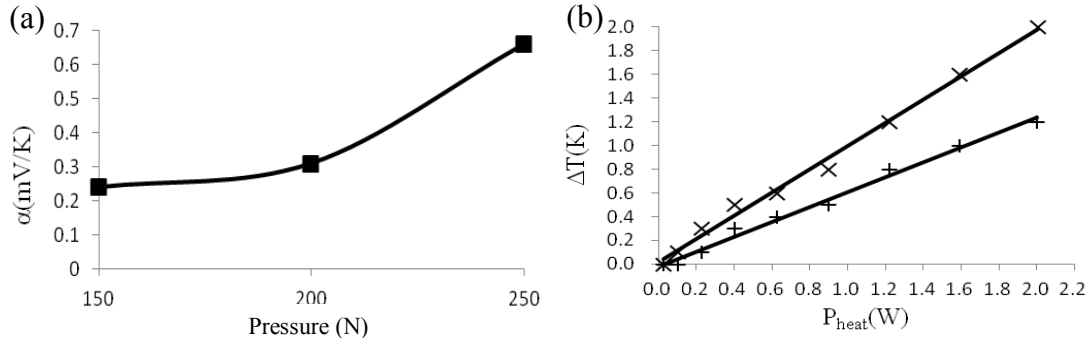


Figure 2.8 (a): Measured Seebeck coefficient as a function of pressure. The markers are measurement values, and the solid line is a guide to the eye only. (b): Temperature difference measurement ΔT as a function of heater power P_{heat} for a Si/SiGe NWAs sample between two Cu blocks. ×: measurement without Ag foil, + measurement with Ag foil. The solid lines are guides to the eye only.

Using these improvements, the Seebeck coefficient of the same Si/SiGe sample has been re-measured. A pressure of 250 N is applied and Ag foil is placed between $Si/Si_{0.8}Ge_{0.2}$ sample and Cu. We notice that the measured Seebeck coefficient has increased to a value of~1.12 mV/K, which is very close to the theoretically expected value (~1.1 mV/K) at room temperature. Thus, Ag foil and large pressure are good choices to increase the contact conductance, making the measurements more accurate.

2.5.2: Schottky barrier height and ideality factor measurement

In practice, the specific contact resistance R_c between metal and semiconductor is strongly related to the Schottky barrier height and ideality factor. Fortunately, the Schottky barrier height and ideality factor of Cu-Si contact can be measured by using

the current flow mechanism of Cu-lightly doped Si contact. The depletion width is wide when the Si is lightly doped. The only way the carriers can get into the metal is by thermionic emission over the Schottky barrier height$\emptyset_B$. The ideal current flow is given by I (Schroder, 1998):

$$I = AA^*T^2 \exp\left(-\frac{e\emptyset_B}{kT}\right)\left[\exp\left(\frac{eV}{kT}\right) - 1\right] \quad (2.11)$$

With A the contact area, A^* the Richardson's constant, T the temperature, $\emptyset_B$ the Schottky barrier height, V the applied voltage, k and e are the Boltzmann constant and the unit charge respectively. Taking account of ideality factor (n_0) (Schroder, 1998), (Gholami & Khakbaz, 2011):

$$I = AA^*T^2 \exp\left(-\frac{e\emptyset_B}{kT}\right)\exp\left(\frac{eV}{n_0kT}\right)\left[1 - \exp\left(-\frac{eV}{kT}\right)\right] \quad (2.12)$$

Eq. (2.12) can be approximated for $V \gg kT/e$ to:

$$I = AA^*T^2 \exp\left(-\frac{e\emptyset_B}{kT}\right)\exp\left(\frac{eV}{n_0kT}\right) \quad (2.13)$$

Thus, there is a linear relationship between ln(I) and V, the slope is $\frac{e}{n_0kT}$ and the constant term is $\ln(AA^*T^2 \exp\left(-\frac{e\emptyset_B}{kT}\right))$. Therefore, the ideality factor (n_0) can be extracted from the slope and Schottky barrier height ($\emptyset_B$) can be extracted from the constant term. The main weakness of this approach is the uncertainty in A*. We have to construct a Schottky diode structure: one Cu-Si Ohmic contact and one Cu-Si Schottky contact. $\emptyset_B$ and n_0 of the Cu-Si Schottky contact can then be measured. In our experiment, one contact surface has high doping density applied via spin-on-doping (SOD, see Chapter 4), and the other surface, which is protected by a SiO_2layer in the SOD process, is still lightly doped. Thus, the heavily doped surface will give an Ohmic contact with Cu, and the other a Schottky contact with Cu.

The measurement set-up is shown in Fig. 2.9.

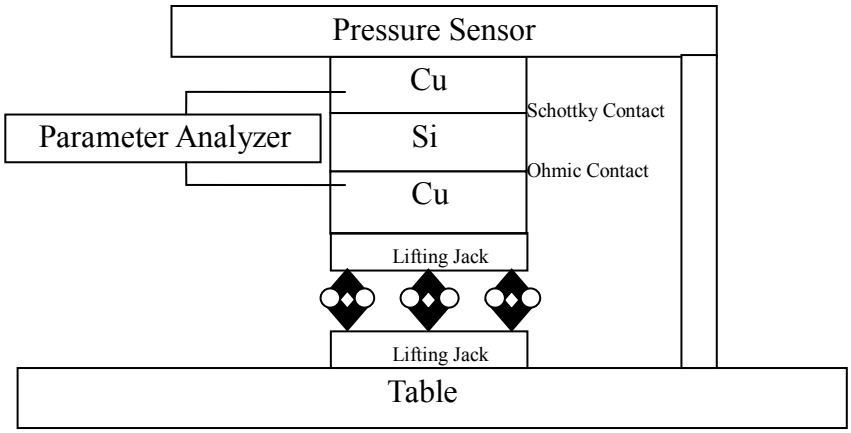


Figure 2.9: Schottky barrier height and ideality factor measurement set-up.

As given in Fig. 2.9, the pressure is fixed at 400 N by adjusting the lifting platform in the measurement process, which is measured by the pressure sensor from

Tedea-Huntleigh (Model: 1042) (Vishay, 2014). The parameter analyzer, which is from Agilent (Model: 4155B) (Keysight.com, 2014), provides a sweeping voltage, and meanwhile, it also records the corresponding current. A typical measurement is given in Fig. 2.10.

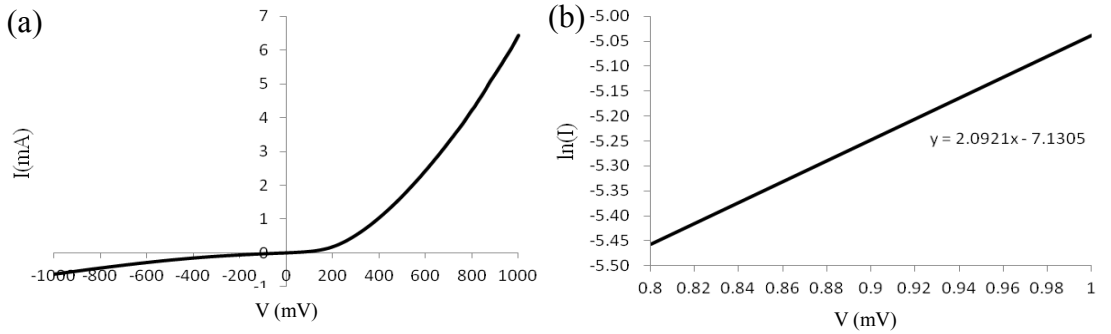


Figure 2.10. (a): I-V characteristic of n-type Si (1-10Ω · cm) bulk. (b): The natural logarithm of the current for V > 0.8 V in order to satisfy $V \gg kT/e$.

The linear relationships between ln(I) and V allows us to extract the ideality factor n_0 = 18.46 and the Schottky barrier height $\emptyset_B$ = 0.64 eV with the contact area 4 cm^2 and the Richardson's constant of n-type Si 112$\frac{A}{cm^2 \cdot K^2}$.

2.5.3: Output power measurement

As given in Section 1.4, a parameter to characterize the performance of the TEG, is the output power P_{out} as a function of load resistanceR_L . P_{out} is measured at constant heat flux to allow comparison between the different test structures. The output power is calculated from:

$$P = V_R^2/R_L \tag{2.14}$$

V_R is the voltage across the TEG for different values of R_L .

The measurement set-up is given in Fig. 2.11.

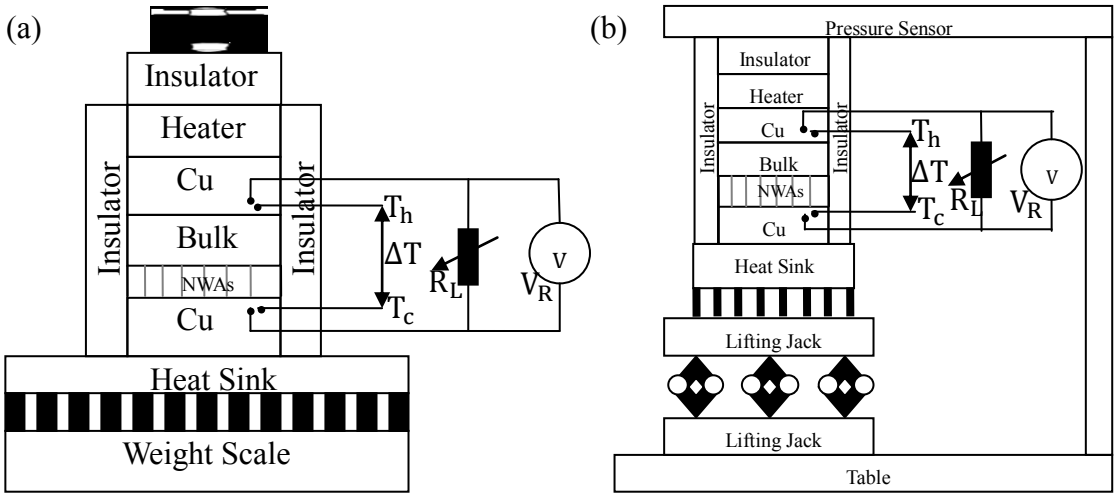


Figure 2.11: One-leg output power measurement set-up.(a): Original set-up. (b): Enhanced set-up.

As given in Fig. 2.11, two output power measurement set-ups have been used in our research. The output power measurement set-up given in Fig. 2.11 (a) is the original set-up, and the main drawback of this set-up is that the pressure from the screw is concentrated on a small area, so the samples between two Cu blocks always collapse if the pressure is over 250 N. The measurement set-up given in Fig. 2.11(b) was developed from Fig. 2.11(a). The pressure is controlled by a lifting jack, and it is uniformly distributed. The pressure is measured by a pressure sensor, which is the same as the pressure sensor given in Fig. 2.9, and the pressure can be increased to 400 N in this set-up. So the contact quality between Cu and sample is better in contrast to the one in Fig. 2.11 (a).

The small Cu blocks used in Fig. 2.11(a) and (b) are with an area of 2 cm×2 cm and a thickness of 0.5 cm. The heater in Fig. 2.11 (a) is a power resistor from Vishay (Model: RH025) (Vishay, 2014), and the heater in Fig. 2.11 (b) is a power resistor from Vishay (Model: RH050) (Vishay, 2014). The thermometer and voltmeter are the same as the ones used in Fig. 2.6 (b). A 10 cm×10 cm black metal heat sink with cooling fins is used to cool the cold side. The sides of the TEG structure are insulated with a 0.5 cm thick layer of polystyrene insulator and the setup is placed in a glove box at atmospheric pressure and room temperature to prevent influences from external air flow variations.

The output power measurement set-up given in Fig. 2.11 only measures one piece of the thermoelectric material and the set-up given in Fig. 2.12 can measure the Seebeck coefficient and output power of a TEG which is composed of two pieces of thermoelectric materials.

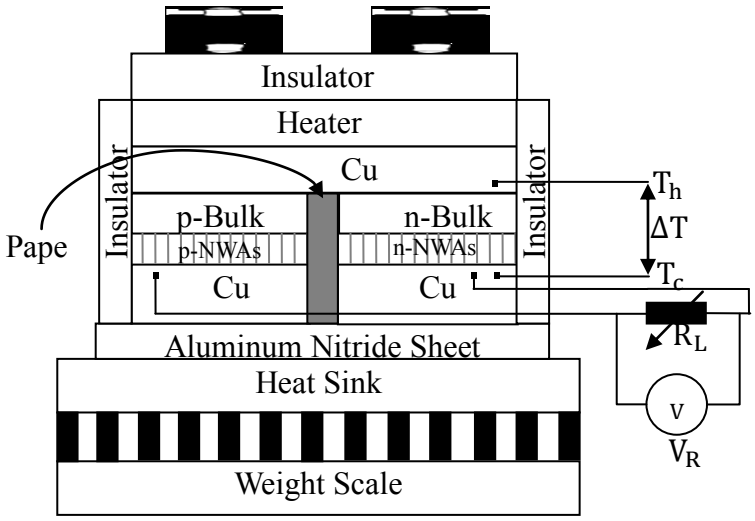


Figure 2.12: Two-leg output power measurement set-up.

Two small Cu blocks, with an area of 2 cm×2 cm and thickness of 0.5 cm are used as independent bottom contacts. A larger Cu block is used at the hot side to form the electric contact between the two semiconductor samples. This places the two semiconductor samples electrically in series and thermally in parallel. An aluminum nitride layer is used as efficient thermal conductor and electrical insulator. This

ensures that the cold temperature T_c is the same for both TEG legs. In order to improve this feature, the samples are placed very close together and are insulated electrically and thermally by a sheet of paper. A 10 cm×10 cm black metal heat sink with cooling fins is used to cool the cold side. The sides of the TEG structure are insulated with a 0.5 cm thick layer of polystyrene and the setup is placed in a glove box at atmospheric pressure and room temperature to prevent influences from external air flow variations. Heat is provided by a power resistor from Vishay (Model: RH025) (Vishay, 2014).

The Seebeck coefficient is measured by gradually increasing ΔT by increasing the input voltage of heater, as well as recording corresponding ΔV.The output power is measured by changing the value of variable resistanceR_L .

2.6 :Conclusion

The literatures reviewed in this chapter refer to the key component of a TEG: Si or $Si_{1-x}Ge_x$ NWs. Section 2.2 demonstrates the excellent thermoelectric characteristics of Si NWs and $Si_{1-x}Ge_x$ alloy which both will be used in this research. Section 2.3 introduces the importance of matrix material which can boost TEG's output power, and this method is very beneficial for this research's future enhancement. Section 2.4 illustrates Si and $Si_{1-x}Ge_x$ NWs etching method (MACE). This section introduces the working principles of MACE and the factors which affect NWs quality. MACE is also the method to prepare Si and $Si_{1-x}Ge_x$ NWs in this research. Section 2.5 introduces kinds of measurement techniques which are used in this research to characterize thermoelectric material, Cu-Si contact and TEG's output power.

Chapter 3: Theoretical calculations, simulations and predictions

This chapter gives theoretical calculations, simulations and predictions which are related to the TEG's performance. In the first section, we will present the theoretical descriptions of ZT for the different thermoelectric materials: Si bulk, SiGe bulk Si/SiGe bulk and Si NWAs. In the second section, we will present the theoretical output power model for a TEG further. In the third section, we will summarize the methods to improve the TEG's performance.

3.1: Figure-of-merit (ZT)

According to the descriptions in Chapter 1, ZT of thermoelectric materials determines the efficiency of a TEG if T_h and $T_c$are given, and $ZT = \frac{\alpha^2 \sigma T}{\lambda}$ is a function of the Seebeck coefficient (α), electrical conductivity (σ) and thermal conductivity (λ). Furthermore, the power factor ($\alpha^2\sigma$) and thermal conductivity (λ) of thermoelectric material are both related to the output power of a TEG, which will be discussed in Section 5.3.

3.1.1:ZT of bulk

In this section we will derive the Seebeck coefficient, electrical conductivity and thermal conductivity model.

1: Seebeck coefficient model
The Seebeck coefficient consists of two terms: one is a purely electronic contribution and the other one is the phonon-drag current. The purely electronic contribution is a result of charge carriers flowing towards the cold end of the bulk due to the temperature gradient. Phonon-drag current is a result of a net current of phonons flowing towards the cold end of the bulk, pulling the charge carriers along with them.

(1): Purely electronic contribution:
The carrier flux through bulk can be described by the Bløtekjær Model (Wanger, 2007):

$$j_v = -S_v \mu_v v \nabla_r \Phi_v - \mu_v v \frac{k}{e}\left(\frac{5}{2} - \ln\frac{v}{N_{c,v}}\right)\nabla_r T \qquad (3.1)$$

With j_v the current density inside n- or p-type bulk, S_v the carrier charge sign ($S_v = -1$ for n-type bulk and $S_v = 1$ for p-type bulk), μ_v is the mobility of electrons or holes, v is the concentration of electrons or holes, Φ_v is the electrochemical potential of electrons or holes, e the unit charge, k the Boltzman

constant, V the voltage, $N_{c,V}$the effective density states in the conduction/valence band and T the temperature,

In 1-dimension this becomes:

$$J_n = \mu_n ne\frac{d\Phi_n}{dx} - \mu_n nk\left(\frac{5}{2} - \ln\frac{n}{N_c}\right)\frac{dT}{dx} = \sigma_n\frac{dV}{dx} + \alpha_{ne}\sigma_n\frac{dT}{dx} \quad (3.2)$$

$$J_p = -\mu_P pe\frac{d\Phi_p}{dx} - \mu_P pk\left(\frac{5}{2} - \ln\frac{p}{N_V}\right)\frac{dT}{dx} = -\sigma_p\frac{dV}{dx} - \alpha_{pe}\sigma_p\frac{dT}{dx} \quad (3.3)$$

With $J_{n,p}$ the electron and hole current density inside n- and p-type bulk, respectively. $\mu_{n,p}$ is the electron/hole mobility, n/p the electron/hole concentration, $\Phi_{n,p}$ the electrochemical potential of electrons/holes, x the distance along the transport direction, $\sigma_{n,p}$ the electron/hole electrical conductivity and $\alpha_{ne,pe}$ the electron/hole electronic contribution to the Seebeck coefficient. The first term in eq. (3.2 and 3.3) is Ohm's law where the current is generated by a voltage difference. The second term is the Seebeck effect - the current is generated by a temperature difference.

The electronic contribution of the Seebeck coefficient obtained from eq. (3.2 and 3.3), is given by:

$$\alpha_{ne} = -\frac{\mu_n nk(\frac{5}{2}-\ln\frac{n}{N_c})}{\mu_n ne} = -\frac{k}{e}(\frac{5}{2} + r - \ln\frac{n}{N_c}) \quad (3.4)$$

$$\alpha_{pe} = -\frac{\mu_p pk(\frac{5}{2}-\ln\frac{p}{N_v})}{\mu_p pe} = +\frac{k}{e}(\frac{5}{2} + r - \ln\frac{p}{N_v}) \quad (3.5)$$

for electrons and holes respectively. r is the scattering factor which is added into eq.(3.4 and 3.5) in order to represent different scattering mechanisms. For example, $r = -\frac{1}{2}$ represents acoustic phonon scattering and $r = \frac{3}{2}$ represents ionized impurity scattering (Li,2006). In this section, r is taken as 0 which represents neutral impurity scattering (Pichanusakorn&Bandaru,2009).

(2): Phonon-drag current:
Due to the thermal gradient, phonons will diffuse from the hot to the cold end. Phonon-carrier interactions will cause the carriers to gain additional momentum. This term, caused by the net movement of the phonon is referred to as the phonon drag effect. It can be modeled as an additional driving force for the carries within the expressions for the Seebeck coefficient (Wanger, 2007).

The phonon drag contribution to the Seebeck coefficient is given by α_{phonon} (Emin, 2006):

$$\alpha_{phonon} = \frac{k}{e}\left(\frac{s^2\tau_r}{D}\right)F = \frac{ks^2\tau_r F}{\mu kT} = \frac{s^2\tau_r F}{\mu T} \quad (3.6)$$

With s the sound velocity, τ_r the relaxation time for the dissipation of the sound wave's momentum through their interactions with atoms (τ_r increases with decreasing temperature), F the fraction of the carrier's momentum that is transferred to the sound waves, and D the diffusion constant. The other constants are as defined before.

As shown in eq. (3.6), the phonon drag contribution to the Seebeck coefficient increases with decreasing temperature, and it is typically appreciable when T < 200 K (Wanger, 2007). The phonon drag effect contributes about 4 mV/K to the Seebeck coefficient at 50 K in high quality Si bulk with a doping density of less than $10^{17}cm^{-3}$ (Emin, 2006).

In our research, we only focus on the Seebeck coefficient for T > 300K, therefore, the phonon drag contribution to the Seebeck coefficient can be ignored in our research.

Thus, the Seebeck coefficient is determined by eq. (3.4 and 3.5) and is dependent on temperature and carrier concentration.

(3): Seebeck coefficient of Si bulk

Using full ionization, the carrier concentration of Si bulk can be approximated by $n \approx N_D$ and $p \approx N_A$(Anderson & Deng et al., 2008). This approximation is valid for most cases except for lightly doped Si bulk at high temperatures, which will be introduced in next section.

The effective density states in the conduction band N_c and in the valence band N_v are both temperature dependent as eq. (3.7 and 3.8) (Anderson & Deng et al., 2008):

$$N_c = 2\left[\frac{2\pi m_e^* kT}{h^2}\right]^{3/2} \quad (3.7)$$

$$N_v = 2\left[\frac{2\pi m_h^* kT}{h^2}\right]^{3/2} \quad (3.8)$$

With h the Planck constant ($6.626 \times 10^{-34} J \cdot s$), m_e^* the effective mass of electrons ($9.8388 \times 10^{-31}kg$) and m_h^* the effective mass of holes ($10.37929 \times 10^{-31}kg$).

Using eq. (3.4, 3.5, 3.7 and 3.8) the Seebeck coefficient of bulk Si as a function of temperature and carrier concentration is given in Fig 3.1.

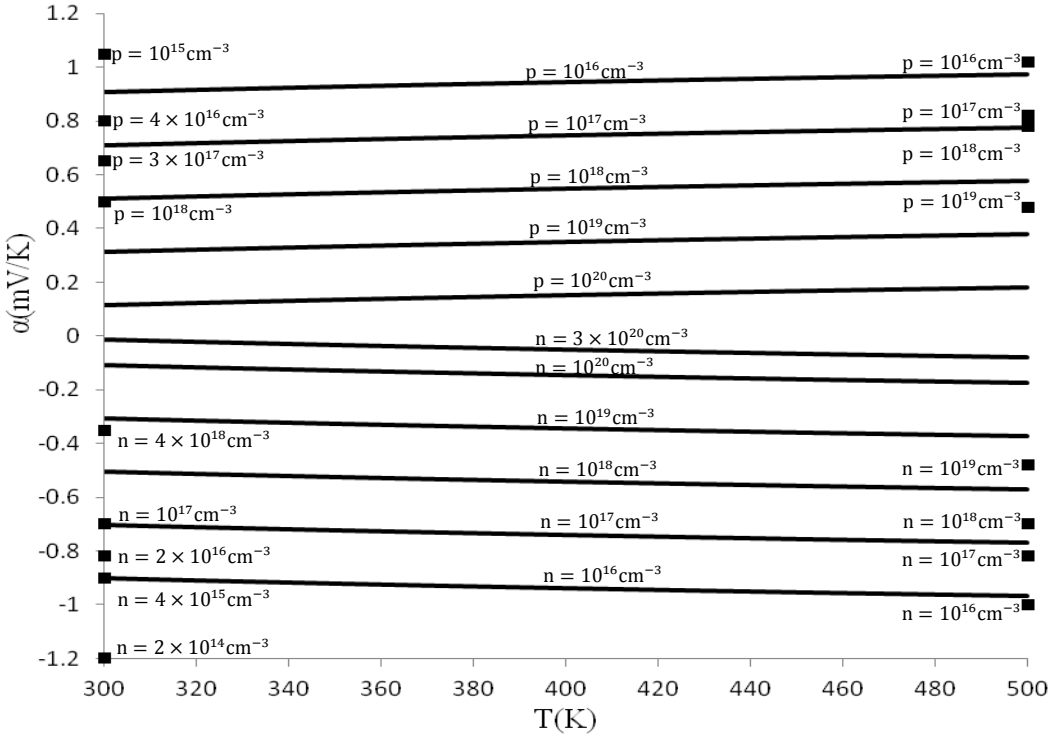


Figure 3.1: n-type and p-type Si bulk's Seebeck coefficient as a function of temperature and carrier concentration. The solid lines are theoretical Seebeck coefficient of Si gotten via eq.(3.4 and 3.5), and the square points are Seebeck coefficients measured by Geballe&Hull (Geballe&Hull,1955) and Slack&Hussain (Slack&Hussain, 1991).

As the solid lines given in Fig 3.1, Si bulk's Seebeck coefficient increases with temperature and decreases with carrier concentration. The measured Seebeck coefficients at room temperature (T=300K) are from (Slack & Hussain, 1991), and they are quite consistent with the theoretical values. The measured Seebeck coefficients T=500K are from (Geballe & Hull, 1955), and the measured Seebeck coefficients at T=500K are also consistent with theoretical values.

(4): Seebeck coefficient of $Si_{1-x}Ge_x$ bulk

The Seebeck coefficient for $Si_{1-x}Ge_x$ bulk is also given by eq. (3.4 and 3.5), but the effective densities of states in $Si_{1-x}Ge_x$ bulk are different from Si bulk.

For p-type $Si_{1-x}Ge_x$ bulk, the effective density of states in the valence band is given by (Zhang,Zeng&Luo,1996)(Zhang, Li & Luo et al., 1998) :

$$N_v = 2\left(\frac{2\pi kTm_{HH}^*}{h^2}\right)^{3/2} + 2\left(\frac{2\pi kTm_{LH}^*}{h^2}\right)^{3/2}\exp\left(\frac{E_{LH}-E_{HH}}{kT}\right) \qquad (3.9)$$

$E_{LH} - E_{HH}$ is the energy difference between light hole and heavy hole band, and is closely related to the Ge fraction (x) (Zhang, Zeng & Luo, 1996).

$$E_{LH} - E_{HH} = -0.155x(eV) \qquad (3.10)$$

m_{HH}^* and m_{LH}^* are respectively heavy and light hole effective mass, both strongly dependent on Ge fraction x(Zhang,Zeng&Luo,1996) ,(Zhang, Li & Luo et al., 1998).

$$\frac{m_0}{m^*_{HH}} = \frac{1-x}{0.336} + \frac{x}{0.21} \quad (3.11)$$

$$\frac{m_0}{m^*_{LH}} = \frac{1-x}{0.234} + \frac{x}{0.141} \quad (3.12)$$

With m_0 the free electron's mass (9.11×10^{-31} kg).

Thus, N_v is strongly dependent on temperature and Ge fraction.

For n-type $Si_{1-x}Ge_x$ bulk, the effective density of states in conduction band is given by (Zhang, Zeng & Luo, 1996):

$$N_C = 2\left(\frac{2\pi kTm^*_{nx}}{h^2}\right)^{3/2}\left[4 + 2\exp\left(\frac{E^{4-}_{cx} - E^{2-}_{cx}}{kT}\right)\right] + 8\left(\frac{2\pi kTm^*_{nL}}{h^2}\right)^{3/2}\exp\left(\frac{E^{4-}_{cx} - E_{cL}}{kT}\right) \quad (3.13)$$

m^*_{nx} and m^*_{nL} are the effective density of state mass in the X and L minima of the conduction band, respectively. Their values are $0.33m_0$ and $0.22m_0$, respectively. E_{cx} and E_{cL} are the energy at the bottom of the X and L energy valley respectively, 4- and 2- denote fourfold and twofold degeneracy respectively (Zhang, Zeng & Luo, 1996).

$$E^{4-}_{cx} - E^{2-}_{cx} = -0.6x(eV) \quad (3.14)$$

$$E^{4-}_{cx} - E_{cL} = -1.0709 + 1.366x - 0.1615x^2\ (eV) \quad (3.15)$$

Thus, the effective density of states in the conduction band (N_C) is also strongly related to temperature and Ge fraction.

According to eq. (3.4, 3.5, 3.9 and 3.13), the Seebeck coefficient of $Si_{1-x}Ge_x$ bulk is dependent on temperature, carrier concentration and Ge fraction. Ge fractions of the $Si_{1-x}Ge_x$ bulk used in our research are 20%, 30% and 40%. Among them, we will present the Seebeck coefficient of $Si_{0.8}Ge_{0.2}$ in Fig. 3.2.

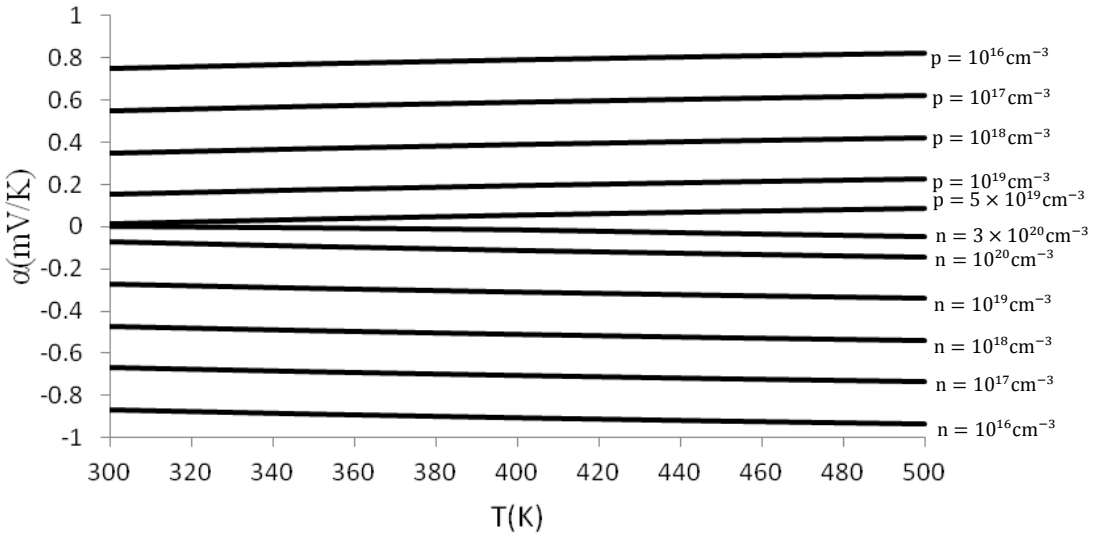


Figure 3.2: Seebeck coefficient of $Si_{0.8}Ge_{0.2}$ bulk as a function of temperature and carrier concentration.

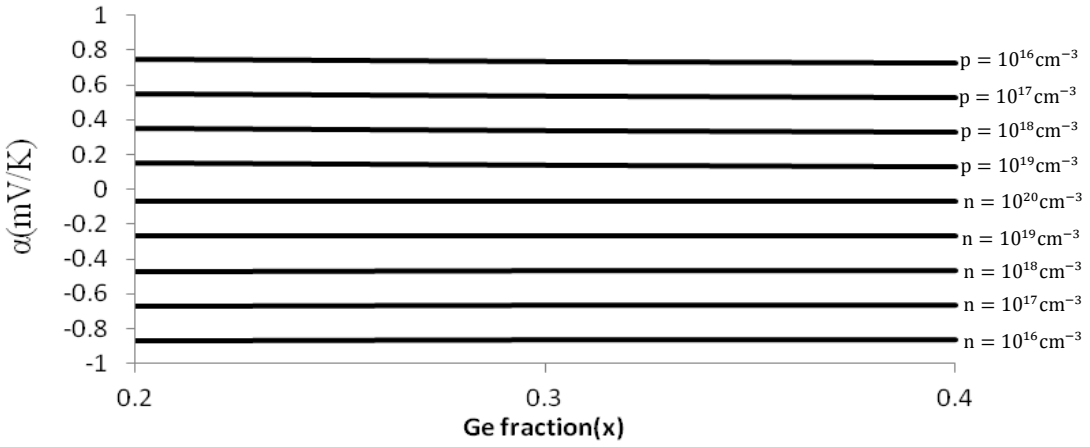


Figure 3.3: Seebeck coefficient of $Si_{1-x}Ge_x$ bulk as a function of Ge fraction(x) and carrier concentration.

As given in Fig. 3.2, the Seebeck coefficient of $Si_{0.8}Ge_{0.2}$ bulk increases with temperature and decreases with carrier concentration. As shown in Fig. 3.3, the Seebeck coefficient does not have appreciable difference with different Ge fraction. Furthermore, there is no appreciable difference with Si under the same conditions.

2: Electrical conductivity model

The electrical conductivity of bulk is determined by carrier concentration and mobility, and is given by (Pierret & Huang, 2004):

$$\sigma = e(n\mu_n + p\mu_p) \tag{3.16}$$

(1): Electron/hole mobility of Si bulk

At room temperature (T=300K), the carrier mobility can be given by eq. (3.17), this mobility model is an empirical formula, and it is based on experimental data and theoretical calculations (Pierret & Huang, 2004).

$$\mu = \mu_{min} + \frac{\mu_0}{1+(\frac{N}{N_{ref}})^{\alpha}} \tag{3.17}$$

With N the doping density (N_A or N_D), μ_{min}, μ_0 N_{ref} and α are all fitting parameters.

The relationship between these parameters and temperature is given by (Pierret & Huang, 2004):

$$A = A_{300}(\frac{T}{300})^{\eta} \tag{3.18}$$

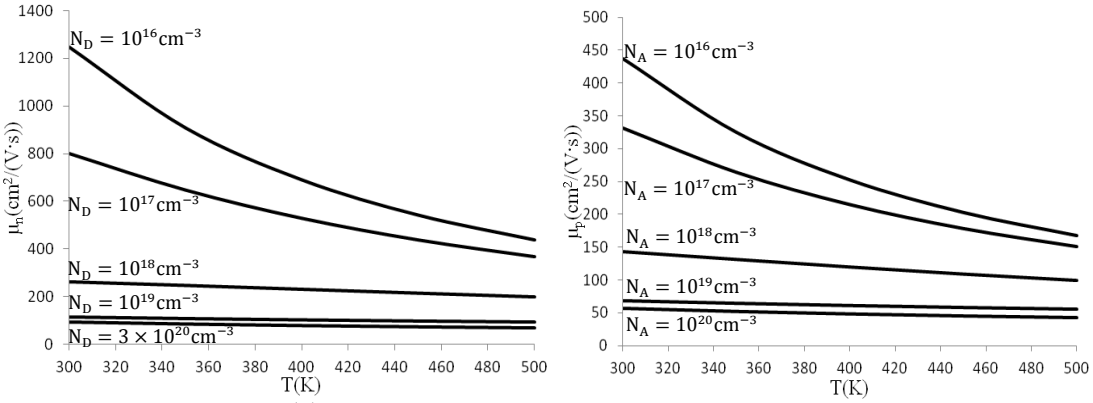
With A denoting μ_{min},μ_0, N_{ref} or α, A_{300} is the value of these parameters at T=300K, T is the temperature and η is a temperature dependent parameter. The detailed values of these parameters for Si bulk are given in Table 3.1 (Pierret &

Huang, 2004).

Parameters	Electrons (T=300K)	Holes (T=300K)	Temperature Parameter (ŋ)
$N_{ref}(cm^{-3})$	1.3×10^{17}	2.35×10^{17}	2.4
$\mu_{min}(cm^2/V \cdot s)$	92	54.3	-0.57
$\mu_0(cm^2/V \cdot s)$	1268	406.9	-2.33(Electrons),-2.23(Holes)
α	0.91	0.88	-0.146

Table 3.1: Parameters for electrons and holes (Pierret & Huang, 2004)

Thus, the carrier mobility is determined by temperature and doping density. The mobility as a function of temperature and doping density is shown in Fig. 3.4. The carrier mobility decreases with temperature and doping density. For Si, the electron mobility is higher than the hole mobility at the same temperature and doping density.



(a) (b)

Figure 3.4: Carrier mobility of bulk Si as a function of temperature and doping density for (a) electron and (b) hole.

(2): Carrier concentration of Si bulk

According to the doping density, Si bulk can be divided into two types: non-degenerate and degenerate. n-type Si is non-degenerate if $E_c - E_f > 2.3kT$. Otherwise, it is degenerate. E_c is conduction band, and E_f is Fermi level. p-type Si is non-degenerate if $E_f - E_v > 2.3kT$. Otherwise, it is degenerate Si. E_v is valence band (Anderson, Anderson & Deng et al., 2008).

The intrinsic carrier concentration is a significant temperature dependent parameter in the carrier concentration calculation. It is given by (Anderson, Anderson & Deng et al., 2008):

$$n_i = 5.71 \times 10^{19}(\frac{T}{300})^{2.365}\exp(-6733/T)\ cm^{-3} \qquad (3.19)$$

With T the temperature.

①: Non-degenerate Si

The n-type Si bulk used in our research is non-compensated, so its electron

concentration is given by (Anderson, Anderson & Deng et al., 2008):

$$n = \frac{N_D}{2} + [(\frac{N_D}{2})^2 + n_i^2]^{1/2} \quad (3.20)$$

The hole concentration is given by (Anderson, Anderson & Deng et al., 2008):

$$p = \frac{n_i^2}{n} \quad (3.21)$$

With N_D the donor doping density and n_i the intrinsic carrier concentration.

If$N_D \gg n_i$, (3.20) can be simplified as:

$$n = N_D \quad (3.22)$$

But this simplification is not valid for lightly doped Si at high temperatures. Because n_i increases dramatically with increasing temperature, hence its influence cannot be ignored for lightly doped Si at high temperatures: Eq. (3.22) is an excellent approximation of eq. (3.20) except of low carrier concentration ($N_D < 10^{15}$ cm^{-3}) at high temperatures ($T \geq 450K$).

The p-type Si bulk used in our research is also non-compensated, so its hole concentration is given by (Anderson, Anderson & Deng et al., 2008):

$$p = \frac{N_A}{2} + [(\frac{N_A}{2})^2 + n_i^2]^{1/2} \quad (3.23)$$

The electron concentration is given by (Anderson, Anderson & Deng et al., 2008):

$$n = \frac{n_i^2}{p} \quad (3.24)$$

With N_A the acceptor doping density.

If$N_A \gg n_i$, (3.23) can be simplified as:

$$p = N_A \quad (3.25)$$

The same as for the electron density, this simplification is not valid for lightly doped Si ($N_D < 10^{15}$ cm^{-3}) at high temperature ($T \geq 450K$).

②: Degenerate Si

Non-degenerate Si which has been discussed in Section ① is lightly doped, and its band gap E_g is considered as a constant which is not related to doping density. Degenerate Si whose band gap narrowing effects become apparent is heavily doped and the band gap narrowing effects strengthen with the increase of doping density.

For n-type non-compensated degenerate Si, the electron concentration (n) can be approximated as N_D, because it is heavily doped. The hole concentration (p) can be observed via the product of electron concentration and hole concentration is given by (Anderson, Anderson & Deng et al., 2008):

$$np = \frac{N_D}{N_C}[\exp(\Delta E_g^*/kT)]n_i^2 \quad (3.26)$$

With n,p respectively the electron and hole concentration, N_D the donor doping density, N_c the effective density states in conduction band, ΔE_g^* the apparent band-gap narrowing caused by heavily doping, k Boltzman constant, T the temperature and n_i the intrinsic carrier concentration.

The apparent band-gap narrowing ΔE_g^* is doping density dependent, and it is given by (Anderson, Anderson & Deng et al., 2008):

$$\Delta E_g^* = 18.6 \ln\left(\frac{N_D}{7\times10^{17}}\right) \text{ meV} \quad (N_D \geq 7 \times 10^{17}\text{cm}^{-3})$$

$$\Delta E_g^* = 0 \quad (N_D < 7 \times 10^{17}\text{cm}^{-3}) \quad (3.27)$$

For n-type Si, ΔE_g^* has a saturation value of 100meV (Anderson, Anderson & Deng et al., 2008).

For p-type non-compensated degenerate Si, the hole concentration (p) can be approximated as N_A. The electron concentration (n) can be gotten via the product of electron concentration and hole concentration is given by (Anderson, Anderson & Deng et al., 2008).

$$np = \frac{N_A}{N_V}[\exp(\Delta E_g^*/kT)]n_i^2 \quad (3.28)$$

The doping dependent band-gap narrowing ΔE_g^* is given by (Anderson, Anderson & Deng et al., 2008):

$$\Delta E_g^* = 9[\ln(\frac{N_A}{10^{17}}) + \sqrt{(\ln(\frac{N_A}{10^{17}}))^2 + 0.5}] \text{ meV} \quad (N_A \geq 10^{17}\text{cm}^{-3})$$

$$\Delta E_g^* = 0 \quad (N_A < 10^{17}\text{cm}^{-3}) \quad (3.29)$$

(3): Electrical conductivity of Si bulk

Using the electron and hole mobility from Section (1), electron and hole concentration from Section (2), we can calculate Si bulk's electrical conductivity as a function of temperature (T) and doping density (N_A or N_D), see Fig. 3.5.

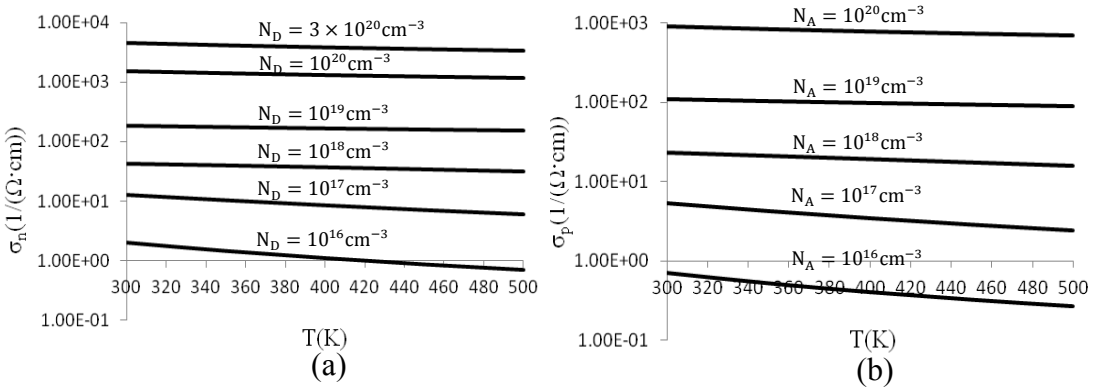


Figure 3.5: Electrical conductivity of bulk Si as a function of temperature and doping density for (a) n-type and (b) p-type Si.

As shown in Fig. 3.5, the electrical conductivity of n-type Si bulk is higher than p-type Si bulk under the same conditions. The electrical conductivity of Si increases with doping density, and it decreases with increasing temperature, because carrier mobility decreases with increasing temperature.

(4): Electrical conductivity of $Si_{1-x}Ge_x$ bulk

Electrical conductivity of bulk $Si_{1-x}Ge_x$ also can be described by eq. (3.16), but the carrier mobility model must be changed. Its carrier mobility and electrical conductivity are related to doping density, Ge fraction and temperature.

The carrier mobility of $Si_{1-x}Ge_x$ bulk can be derived by linear approximation (Sze&Ng,2006):

$$\mu_{Si_{1-x}Ge_x} = (1-x)\mu_{Si} + x\mu_{Ge} \tag{3.30}$$

The carrier motility of Si and Ge bulk which are doping density and temperature dependent must be obtained firstly in order to get the carrier mobility of $Si_{1-x}Ge_x$ bulk.

The carrier mobility of Si bulk has been given in Section (1), and the carrier mobility of Ge bulk will be discussed in the following.

① Carrier mobility of Ge bulk as a function of doping density

The measurement results of carrier mobility of Ge bulk at room temperature (T=300K) are given in Fig. 3.6. The carrier mobility of Ge bulk decreases with increasing doping density when $N_{A/D} > 10^{16}cm^{-3}$(Pierret & Huang, 2004), because the carrier mobility is determined by two scattering mechanisms: one is phonon scattering which is independent of doping density, and the other one is ionized impurity scattering which is doping density dependent: the ionized impurity scattering increases with the amount of scattering centers which is positively related to the doping density. Thus, the carrier mobility decreases with increasing doping density under the same temperature due to more ionized impurity scatterings (Pierret & Huang, 2004), (Zeghbroeck,2007).

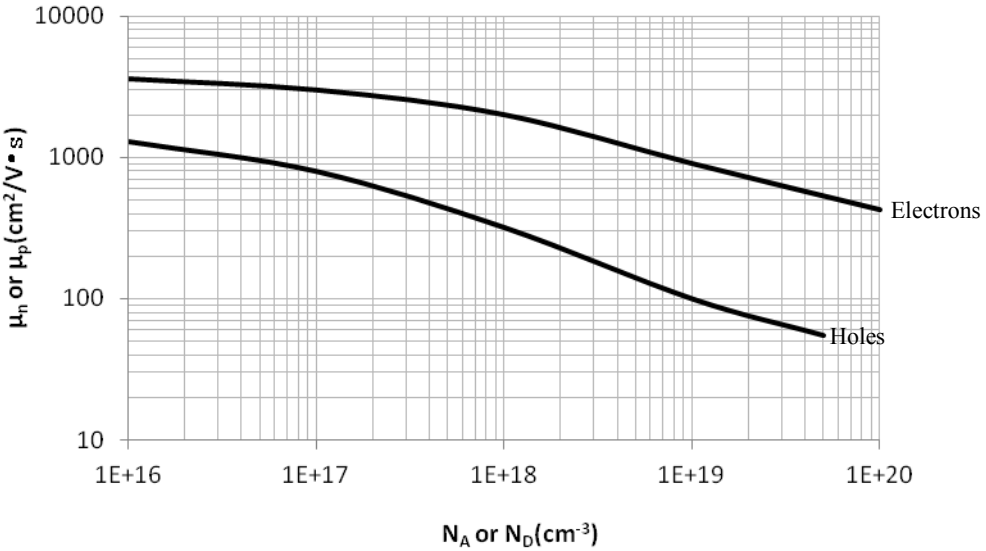


Figure 3.6: Carrier mobility of bulk Ge as a function of doping density at room temperature (T=300K) (Pierret & Huang, 2004).

② Carrier mobility of Ge bulk as a function of temperature

Phonon scattering and ionized impurity scattering are both temperature dependent: phonon scattering increases with increasing temperature, but ionized impurity scattering decreases with increasing temperature.

As the model given, the carrier mobility due to ionized impurity scattering is proportional to $T^{1.5}/(N_{A/D})^{\Gamma}$(Zeghbroeck,2007). The electron mobility of Ge due to phonon scattering is proportional to $T^{-1.7}$, and the hole mobility of Ge due to phonon scattering is proportional to $T^{-2.3}$(Zeghbroeck,2007). Normally, these two scatterings are present at the same time, and it is a very good approximation to combine their influences using Matthiessen's Rule, as given in eq. (3.31 and 3.32), (Fischetti & Laux, 1996)(Zeghbroeck,2007).

$$\frac{1}{\mu_n} = \frac{1}{A_n T^{-1.7}} + \frac{(N_D)^{\Gamma n}}{B_n T^{1.5}} \tag{3.31}$$

$$\frac{1}{\mu_p} = \frac{1}{A_p T^{-2.3}} + \frac{(N_A)^{\Gamma p}}{B_p T^{1.5}} \tag{3.32}$$

Eq. (3.31) is for electrons and eq. (3.32) is for holes.$\Gamma n(>0)$,$\Gamma p(>0)$ A_n, B_n, A_p and B_p are constants which can be derived via carrier mobility of bulk Ge at room temperature.

As the model given in eq. (3.31 and 3.32), the carrier mobility decreases with increasing doping density under the same temperature, which is consistent with the data given in Fig.3.6. It is also found that the carrier mobility is independent of doping

density if $N_{A/D} \leq 10^{14}cm^{-3}$, because the low doping density makes ionized impurity scattering ignorable, and the carrier mobility is only determined by Phonon scattering (Pierret & Huang, 2004). Thus, eq.(3.31 and 3.32) can be approximated as:

$$\frac{1}{\mu_n} = \frac{1}{A_n T^{-1.7}} \tag{3.33}$$

$$\frac{1}{\mu_p} = \frac{1}{A_p T^{-2.3}} \tag{3.34}$$

According to data given in (Pierret & Huang, 2004), Ge bulk's electron mobility is $4000cm^2/V \cdot s$ and hole mobility is $2000cm^2/V \cdot s$ when $N_{A/D} \leq 10^{14}cm^{-3}$ at room temperature (T=300K). Thus, the value of A_n is 6.5×10^7, and the value of A_p is 9.96×10^8.

Once A_n and A_p have been observed, eq. (3.31 and 3.32) can be re-written as eq. (3.35 and 3.36) at room temperature (T=300K).

$$\frac{1}{\mu_n} = \frac{1}{4000} + \frac{(N_D)^{\Gamma n}}{5196.152 \times B_n} \tag{3.35}$$

$$\frac{1}{\mu_p} = \frac{1}{2000} + \frac{(N_A)^{\Gamma p}}{5196.152 \times B_p} \tag{3.36}$$

Fig. 3.6 has already given measured $\mu_{n/p}$ as a function of $N_{A/D}$ at room temperature, so the values of $\Gamma_{n/p}$ and $B_{n/p}$ can be derived by regression analysis in Excel: $\Gamma n = 0.4779$, $\Gamma p = 0.5051$, $B_n = 3.21 \times 10^8$ and $B_p = 9.62 \times 10^7$. Therefore, Ge bulk's carrier mobility is doping density and temperature dependent, which is given in eq. (3.37 and 3.38).

$$\mu_n = \frac{1}{\frac{1}{6.5 \times 10^7 \times T^{-1.7}} + \frac{(N_D)^{0.4779}}{3.21 \times 10^8 \times T^{1.5}}} \tag{3.37}$$

$$\mu_P = \frac{1}{\frac{1}{9.96 \times 10^8 \times T^{-2.3}} + \frac{(N_A)^{0.5051}}{9.62 \times 10^7 \times T^{1.5}}} \tag{3.38}$$

In order to verify the accuracy of the models described by eq.(3.37 and 3.38), the measured carrier mobility which is given in Fig. 3.6 and the theoretical carrier mobility which are described by eq. (3.37 and 3.38) will be plotted together in Fig. 3.7. These two theoretical models and measured values are very consistent. Furthermore, as given in Fig. 3.8, these two theoretical models also describe the relations between carrier mobility and temperature: for the lightly doped Ge bulk, carrier mobility decreases with increasing temperature, because phonon scattering is the main mechanism to determine the carrier mobility; for the heavily doped Ge bulk, the carrier mobility slightly increases with increasing temperature due to more ionized impurity scattering.

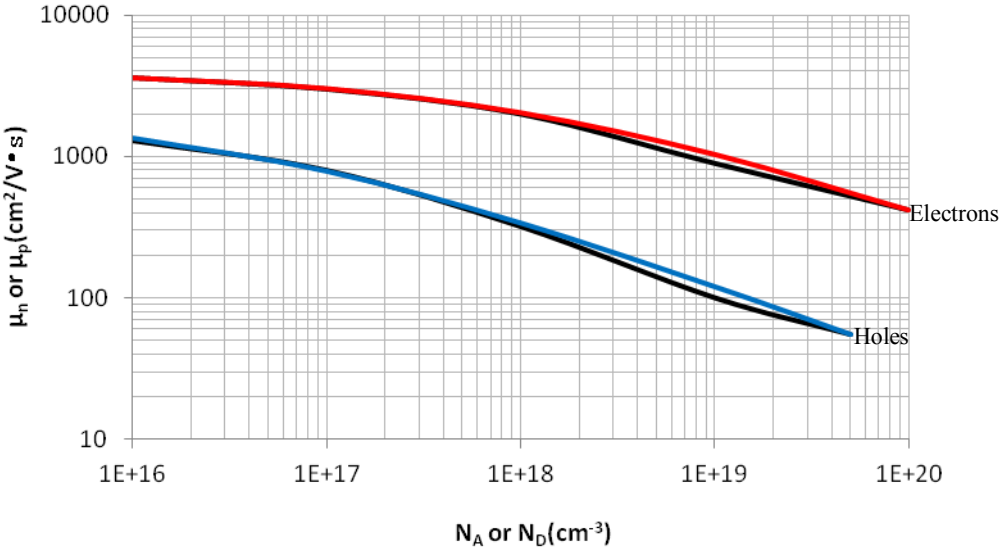


Figure 3.7: Carrier mobility of bulk Ge as a function of doping density at room temperature (T=300K). The black solid line is measured value (Pierret & Huang, 2004). The red and blue solid lines are theoretical values.

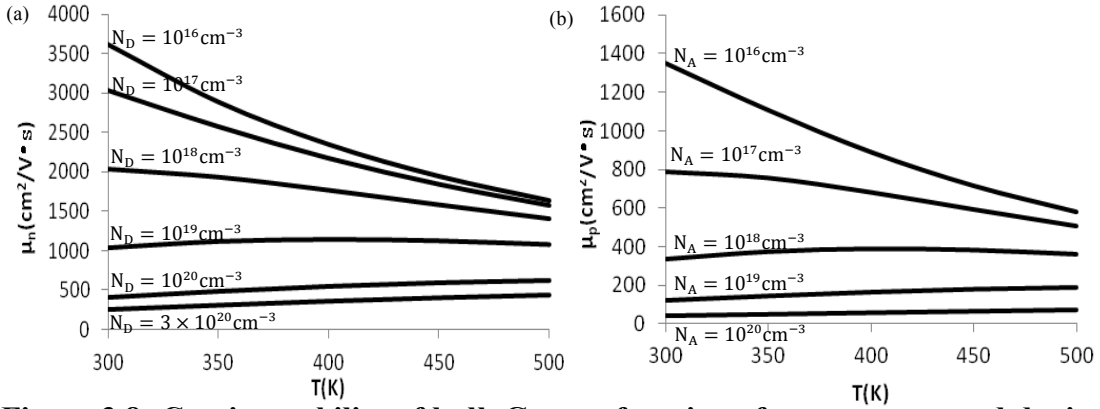


Figure 3.8: Carrier mobility of bulk Ge as a function of temperature and doping density for (a) electron and (b) hole.

③ carrier mobility and electrical conductivity of $Si_{1-x}Ge_x$ bulk

As described by eq. (3.30), the mobility of $Si_{1-x}Ge_x$ bulk is derived by the linear approximation. $Si_{0.8}Ge_{0.2}$ bulk is taken as the example here.

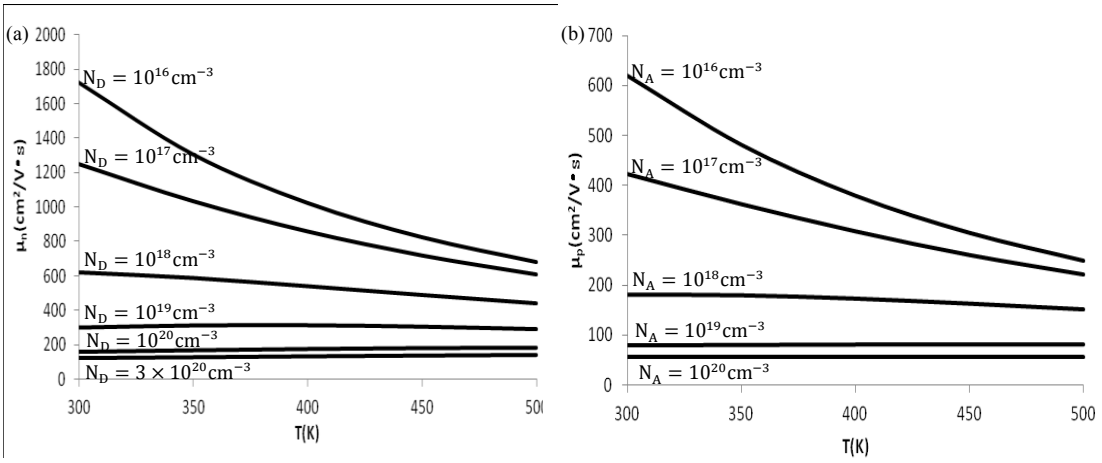


Figure 3.9: Carrier mobility of $Si_{0.8}Ge_{0.2}$ bulk as a function of temperature with different doping densities for (a) electron and (b) hole.

As given in Fig. 3. 9, electron mobility is higher than hole mobility under the same temperature and doping density. Carrier mobility decreases with increasing doping density due to more ionized impurity scattering. Carrier mobility decreases with increasing temperature for lightly doped $Si_{0.8}Ge_{0.2}$ bulk due to the ignorable ionized impurity scattering, and carrier mobility increases slightly with increasing temperature for the heavily doped $Si_{0.8}Ge_{0.2}$ bulk due to more ionized impurity scattering. Carrier mobility also increases with increasing Ge fraction, because Ge bulk's carrier mobility is higher than Si bulk's carrier mobility under the same temperature and doping density.

Then, the electrical conductivity of $Si_{0.8}Ge_{0.2}$ bulk can be gotten straightforwardly, which is given in Fig. 3.10.

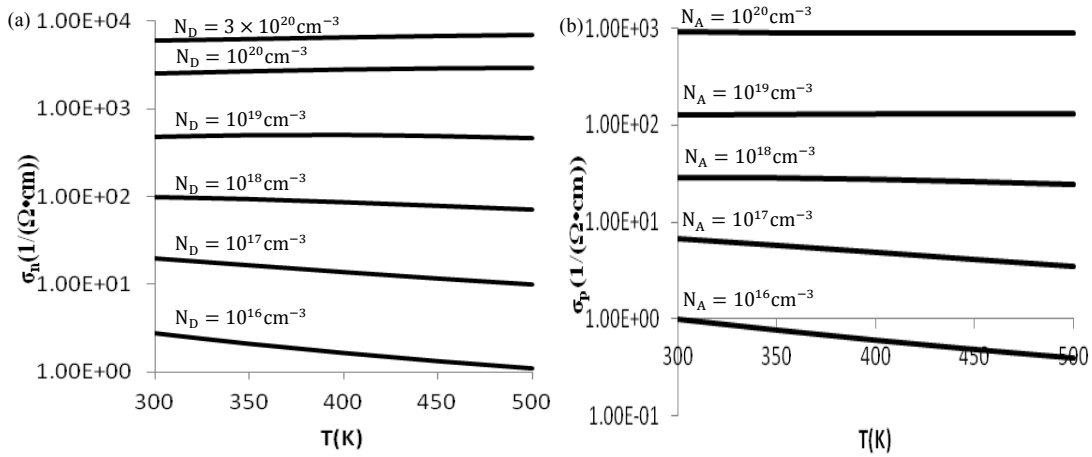


Figure 3.10: Electrical conductivity of bulk $Si_{0.8}Ge_{0.2}$ as a function of temperature and doping density for (a) n-type and (b) p-type.

As shown in Fig. 3.10, $Si_{0.8}Ge_{0.2}$ bulk's electrical conductivity increases with doping density due to more carriers, and it decreases with temperature, especially for the lightly doped $Si_{0.8}Ge_{0.2}$ bulk, because strong phonon scattering makes the carrier mobility smaller.

3: Thermal conductivity model

The thermal conductivity consists of two portions: one is the lattice thermal conductivity and the other one is the electronic portion of the thermal conductivity. The total thermal conductivity of bulk is the sum of lattice thermal conductivity and the electronic portion of thermal conductivity (Vo, Williamson & Lordi et al., 2008).

(1): Lattice thermal conductivity of Si bulk:
The lattice thermal conductivity, λ_L of Si bulk is strongly related to the temperature. See Fig. 3.11(Glassbrenner&Slack,1964).

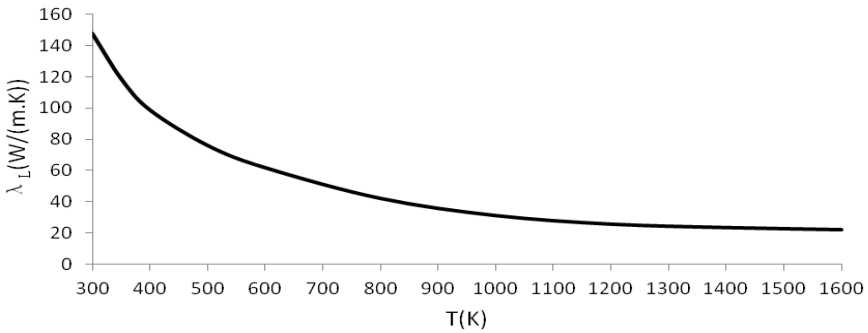


Figure 3.11: Lattice thermal conductivity of bulk Si as a function of temperature (Glassbrenner&Slack. 1964).

(2): Electronic portion of Si bulk's thermal conductivity:
The electronic portion of the thermal conductivity describes the free electrons' ability to conduct heat. This is described by the Wiedemann-Franz law, given by (Rowe,1995):

$$\lambda_e = \frac{\pi^2 k^2}{3e^2}\sigma T \tag{3.39}$$

As indicated in eq. (3.39), the electronic portion of the thermal conductivity is determined by doping density and temperature, given in Fig. 3.12.

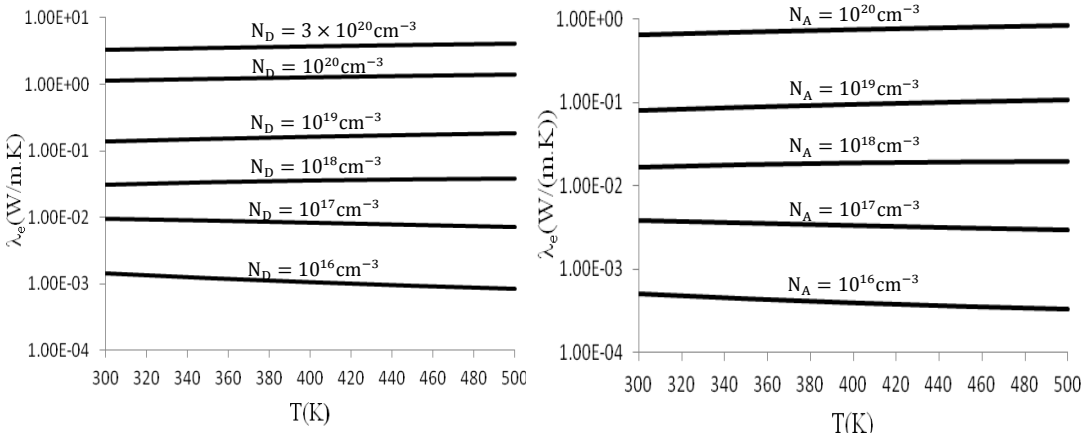
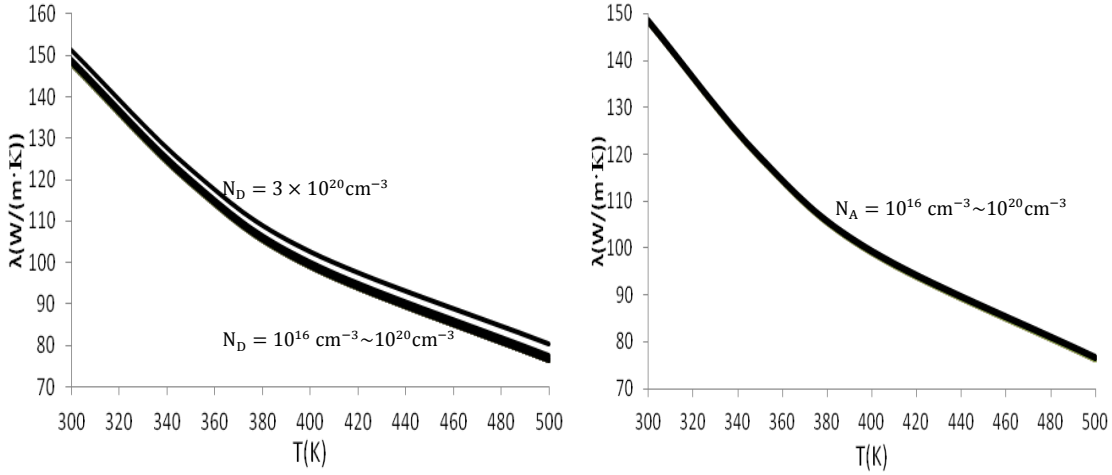


Figure 3.12: Electronic portion of thermal conductivity for (a) n-type Si bulk and (b) p-type Si bulk.

(3): Thermal conductivity of Si bulk:

Thermal conductivity is the sum of λ_L and λ_e. For the given doping density and temperature, the electronic contribution to the thermal conductivity is negligible. The thermal conductivity given in Fig. 3.13 is thus close to lattice thermal conductivity given in Fig. 3.11.



(a) (b)

Figure 3.13: Thermal conductivity of bulk Si as a function of temperature and doping density for (a) n-type and (b) p-type.

Accurate measurement of the thermal conductivity is quite difficult, but some accurate measurements at different temperatures, have been done by Shanks et al. (Shanks, Maycock & Sidles et al., 1963), which are given in Table 3.2.

T(K)	$\lambda\ (\frac{W}{m \cdot K})$ Measurement (Shanks, Maycock & Sidles et al., 1963)	$\lambda\ (\frac{W}{m \cdot K})$ Used in theoretical ZT model (Ioffe.ru, 1964), (Hyperphysics.phy-astr.gsu.edu, 2014)
300	142.2	148
400	97.4	98.9
500	69.2	76.2

Table 3.2: Thermal conductivity of bulk Si at different temperatures .

(4): Lattice thermal conductivity of $Si_{1-x}Ge_x$:

There are two kinds of three phonon processes: N-process, in which the crystal momentum is conserved, and U-process, in which the total momentum is changed by a reciprocal lattice vector. N-process and U-process can be characterized by relaxation times given by τ_N and τ_P (Abeles, 1963):

$$\tau_N^{-1} = B_1 f^2 \quad (3.40)$$

$$\tau_P^{-1} = B_2 f^2 \quad (3.41)$$

Where

$$\frac{B_1}{B_2} = \Lambda \quad (3.42)$$

With f the phonon frequency, B_1 and B_2 are independent of f and the ratio Λ is independent of temperature.

The lattice thermal resistivity due to three phonon an-harmonic scattering is given by W_p (Abeles, 1963):

$$W_p = 10^5\pi^3 3^{-1}4^{-1/3}\hbar^3 k^{-3}m^{-1}\gamma_1^2 TM^{-1}\delta^{-1}\theta^{-3} \quad (3.43)$$

With m the unit atomic mass ($m = 1.66 \times 10^{-27}kg$) ,$\gamma_1$ a parameter determined by fitting the theoretical curve to the measured values, T the temperature, M the atomic weight, δ the cube root of the atomic volume, it is equal to half of the lattice parameter for Si and Ge, θ the Debye temperature, $\hbar$ and k are respectively reduced Planck and Boltzmann constants.

The Debye temperature is given by θ (Abeles, 1963):

$$\theta = \frac{\beta}{M^{\frac{1}{2}}\delta^{\frac{3}{2}}} \quad (3.44)$$

With β the constant within a given covalent crystal system. In SiGe alloy, β is $1.52 \times 10^{-8}K \cdot cm^{3/2}$.

If (3.44) is substituted into (3.43), the expression of W_P becomes (Abeles, 1963):

$$W_P = 1.75 \times 10^{-1}\gamma_1^2\beta^{-3}M^{1/2}\delta^{7/2}T \quad (W^{-1} \cdot K \cdot cm) \quad (3.45)$$

The disorder of the lattice is taken into account as follows. An atom of the virtual crystal is replaced by an atom of the alloy. This atom acts as a virtual impurity and scatters phonons. In general, the virtual impurity atom differs from the atoms of the virtual crystal in its mass, in its size and in the coupling forces to its neighbors. The disorder scattering relaxation time is given by τ_P (Abeles, 1963):

$$\tau_P^{-1} = \omega^4\delta^3\Gamma/4\pi v^3 \quad (3.46)$$

In the case of a mixture of two kinds of atoms, Γ is given by (Abeles, 1963):

$$\Gamma = x(1-x)[(\Delta M/M)^2 + \epsilon(\Delta\delta/\delta)^2] \quad (3.47)$$

With x the fraction of Ge. $M = xM_{Ge} + (1-x)M_{Si}$, $\delta = x\delta_{Ge} + (1-x)\delta_{Si}$, $\Delta M = M_{Ge}\text{-}M_{Si}$, $\Delta\delta = \delta_{Ge} - \delta_{Si}$.

The total lattice thermal resistivity includes three phonon an-harmonic scattering and disorder of the lattice is given by W (Abeles, 1963):

$$W = W_P\left(1 + \frac{5}{9}\Lambda\right)\left[\frac{\arctan(U)}{U} + \frac{(1-\frac{\arctan(U)}{U})^2}{(\frac{1+\Lambda}{5\Lambda})U^4 - \frac{1}{3}U^2 + 1 - \frac{\arctan(U)}{U}}\right]^{-1} \quad (3.48)$$

Where

$$U^2 = U_0^2(1 + \frac{5}{9}\Lambda)^{-1} \quad (3.49)$$

$$U_0^2 = (\frac{9}{2}\pi)^{1/3}\pi^2\hbar k^{-2}\delta\Gamma\theta^{-1}W_P^{-1} \quad (3.50)$$

If eq. (3.50) is substituted into eq. (3.49), U is given by eq. (3.51) (Abeles, 1963):

$$U = 8.69 \times 10^6 \times (1 + \frac{5}{9}\Lambda)^{-1/2}\gamma_1^{-1}\beta\Gamma^{1/2}\delta^{-1/2}T^{-1/2} \quad (3.51)$$

The lattice thermal conductivity is the reciprocal of lattice thermal resistivity, and it is given by λ (Abeles, 1963):

$$\lambda = \frac{1}{W} \tag{3.52}$$

Thus, thermal conductivity as a function of Ge fraction and temperature are plotted in Fig. 3.14.

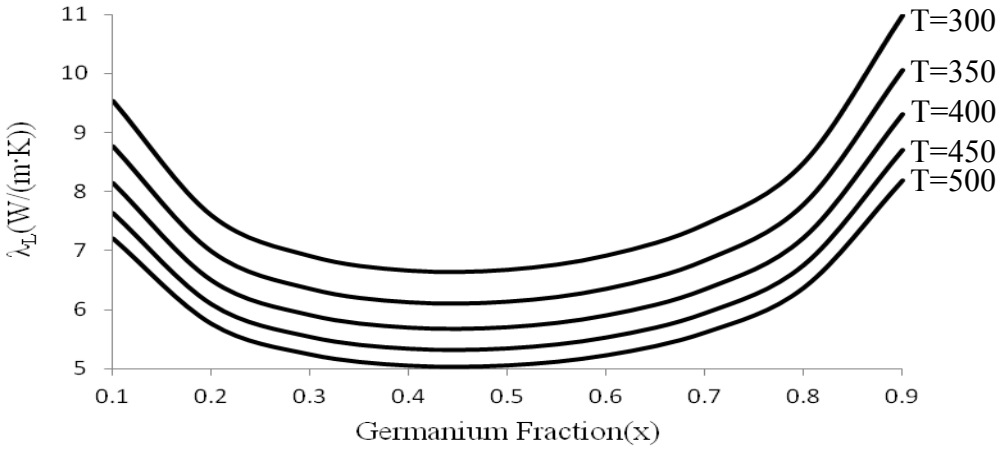


Figure 3.14: Lattice thermal conductivity of $Si_{1-x}Ge_x$ as a function of Ge fraction and temperature.

Fig. 3.14 indicates the thermal conductivity of $Si_{1-x}Ge_x$ as a function of Ge fraction at different temperatures. The theoretical lines are calculated from (3.45), (3.47), (3.48), (3.50) and (3.52) with $\gamma_1 = 1.77, \beta = 1.52 \times 10^{-8} K \cdot cm^{3/2}, \Lambda = 2.5, \epsilon = 39$ M and δ are determined by the linear approximation: $M_{Si} = 28.09$, $M_{Ge} = 72.6$, $\delta_{Si} = 2.7155 \times 10^{-8}$ cm, $\delta_{Ge} = 2.82875 \times 10^{-8}$cm.

As indicated in Fig. 3.14, the lattice thermal conductivity reaches a minimum value when the Ge fraction is 50%. The lattice thermal conductivity of $Si_{0.8}Ge_{0.2}$ at room temperature (T=300K) is ~7.59$\frac{W}{K \cdot m}$, while the lattice thermal conductivity of Si at room temperature (T=300K) is 145$\frac{W}{K \cdot m}$. Thus, the lattice thermal conductivity of $Si_{0.8}Ge_{0.2}$ is only 5.2% of Si's lattice thermal conductivity at room temperature. So, the lattice thermal conductivity has the largest drop from Si to SiGe alloy, but the difference between different alloy fractions beyond 20% is not very big.

(5): Electronic portion of $Si_{1-x}Ge_x$ bulk's thermal conductivity

The electronic portion of the thermal conductivity is given by Wiedemann-Franz law. As given in eq. (3.39), the electronic portion of thermal conductivity is$\frac{\pi^2 k^2}{3e^2} T\sigma$, and$\frac{\pi^2 k^2}{3e^2}$ is2.44487×10^{-8}.

Taking $Si_{0.8}Ge_{0.2}$ as an example, the electronic portion of the thermal conductivity as a function of temperature and doping density is given in Fig. 3.15.

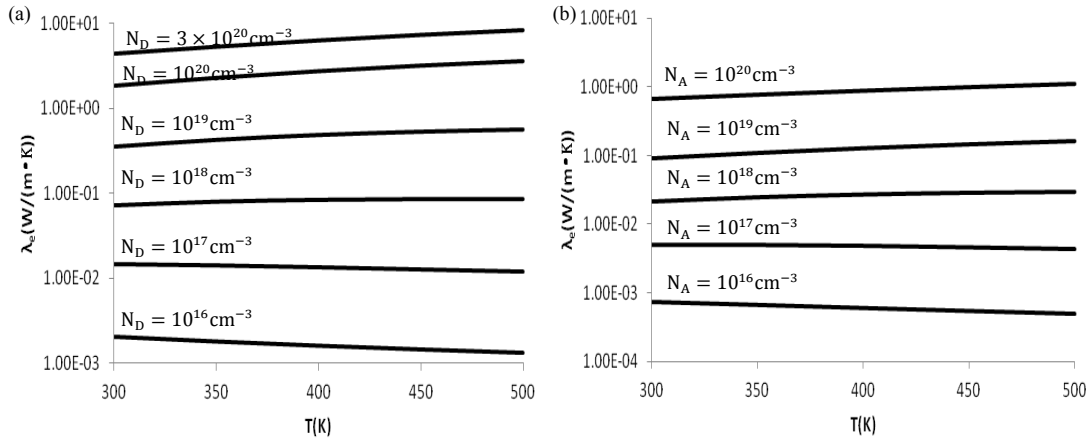


Figure 3.15: $Si_{0.8}Ge_{0.2}$electronic portion of thermal conductivity as a function of temperature and doping density for (a) n-type bulk and (b) p-type bulk.

The lattice thermal conductivity of $Si_{1-x}Ge_x$ is of the order of $\sim 1\frac{W}{K\cdot m}$ at room temperature. As shown in Fig. 3.15, the electronic portion of thermal conductivity is also of the same order of magnitude if the sample is very heavily doped, so the electronic portion cannot be ignored in this circumstance.

(6): Thermal conductivity of $Si_{1-x}Ge_x$ bulk

The same as Si bulk, the thermal conductivity is also the sum of lattice thermal conductivity and electronic portion of thermal conductivity. For $Si_{0.8}Ge_{0.2}$ bulk the total thermal conductivity is given in Fig. 3.16 .

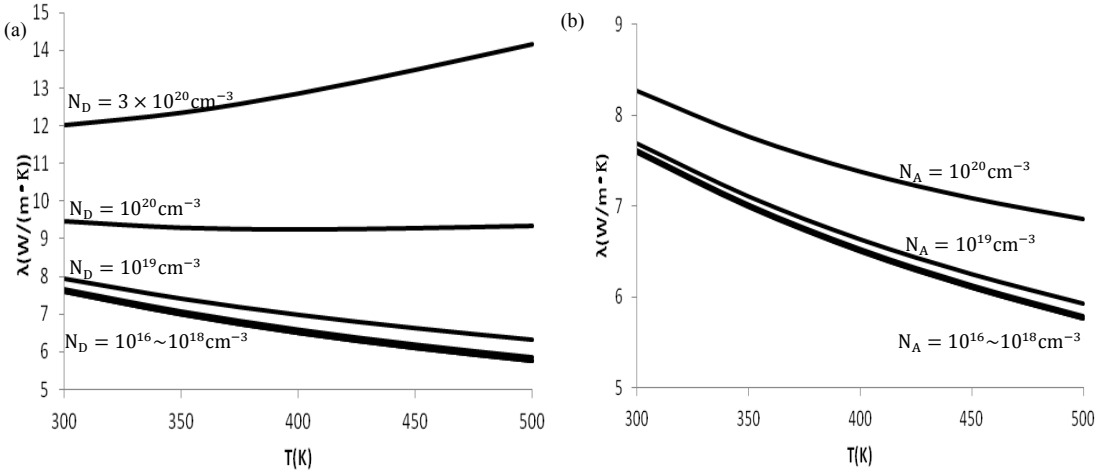


Figure 3.16: Thermal conductivity of bulk $Si_{0.8}Ge_{0.2}$ as a function of temperature and doping density for (a) n-type and (b) p-type.

From Fig 3.16 it is apparent that the electronic contribution to the thermal conductivity becomes important at doping densities higher than 10^{19} cm^{-3} for both p- and n-type material.

4: ZT of bulk

(1): ZT of Si bulk

Putting together Seebeck coefficient α from Fig.3.1, electrical conductivity σ from

Fig. 3.5 and thermal conductivity λ from Fig.3.13, ZT as a function of doping density and temperature, based on eq. (1.13), is given in Fig. 3.17.

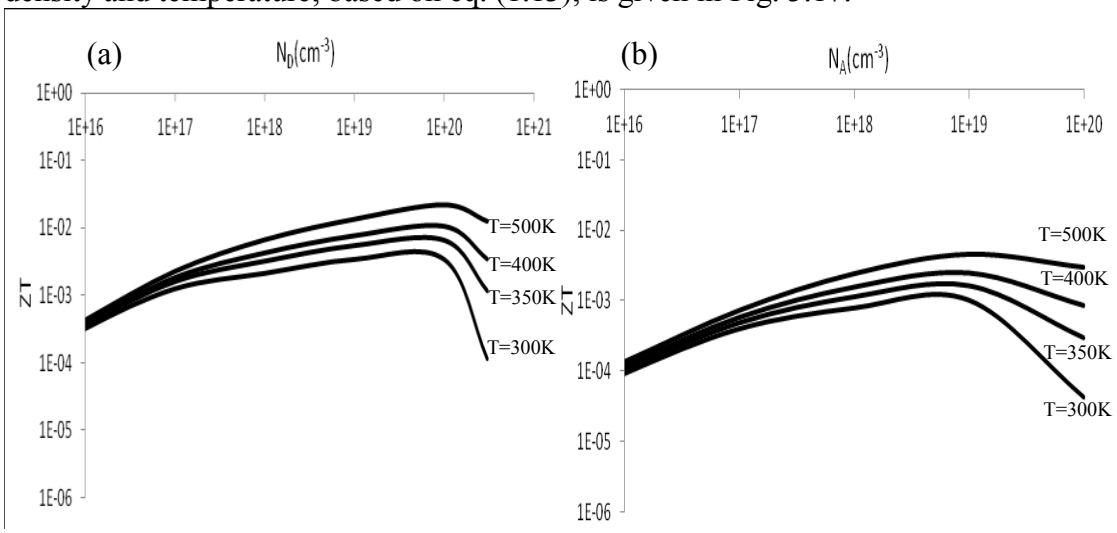


Figure 3.17: ZT of Si bulk as a function of doping density and temperature for (a) n-type and (b) p-type.

As shown in Fig. 3.17, Si bulk's ZT is a doping density and temperature dependent function. p-type Si bulk reaches the highest ZT when its doping density is $\sim 10^{19} \mathrm{cm}^{-3}$. n-type Si bulk reaches the highest ZT when its doping density is $\sim 10^{20} \mathrm{cm}^{-3}$. ZT of n-type Si bulk is higher than the one of p-type Si bulk under the same conditions.

(2): ZT of $\mathrm{Si}_{1-x}\mathrm{Ge}_x$ bulk

$\mathrm{Si}_{1-x}\mathrm{Ge}_x$ bulk is a better thermoelectric material compared with Si bulk, because of its lower thermal conductivity, and its theoretical ZT model is also based on its Seebeck coefficient model, electrical conductivity model and thermal conductivity model.

Taking $\mathrm{Si}_{0.8}\mathrm{Ge}_{0.2}$ as an example: its ZT is a function of doping density and temperature is given in Fig. 3.18.

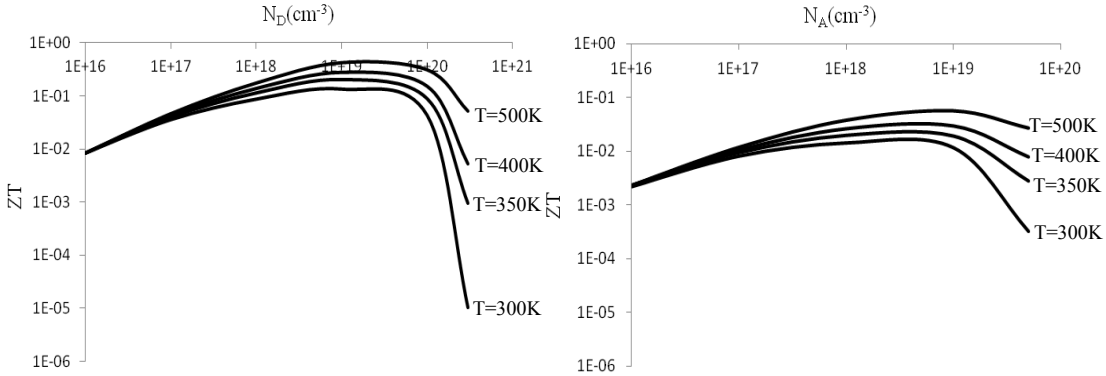


Figure 3.18: ZT of $\mathrm{Si}_{0.8}\mathrm{Ge}_{0.2}$ as a function of doping density and temperature for (a) n-type and (b) p-type bulk.

As shown in Fig. 3.18, p-type $\mathrm{Si}_{0.8}\mathrm{Ge}_{0.2}$ bulk reaches the highest ZT when the

doping density is $\sim 10^{19}\mathrm{cm}^{-3}$; n-type $Si_{0.8}Ge_{0.2}$ bulk also reaches the highest ZT when the doping density is $\sim 10^{19}\mathrm{cm}^{-3}$. ZT of n-type $Si_{0.8}Ge_{0.2}$ bulk is higher than p-type $Si_{0.8}Ge_{0.2}$ bulk's ZT under the same conditions.

(3): ZT of Si/ $Si_{1-x}Ge_x$bulk

Instead of using pure $Si_{1-x}Ge_x$ bulk, a Si/ $Si_{1-x}Ge_x$ bulk is used in this work. A linearly graded relaxed $Si_{1-x}Ge_x$ layer, with a graded Ge faction, was deposited first to overcome the lattice mismatch between Si and SiGe, followed by a constant composition layer. The Si/ $Si_{1-x}Ge_x$ bulk used in our experiment is shown in Fig. 3.19. The thickness of the linearly graded relaxed p-type SiGe layer is 3 μm, followed by a constant composition p-type $Si_{1-x}Ge_x$ layer with a thickness of 3 μm(Xu, Li & Myronov et al., 2012). Ge fractions in the constant composition p-type SiGe layer are 20%, 30% and 40%.

Constant Composition p-type $Si_{1-x}Ge_x$ Layer (3μm)
Linearly Graded Relaxed p-type $Si_{1-x}Ge_x$ Layer (3μm)
p-type Si Substrate (1-10Ω· cm) (500 μm)

Figure 3.19: The structure of Si/$Si_{1-x}Ge_x$ bulk.

① Thermal conductivity of Si/ $Si_{1-x}Ge_x$bulk

When the thermal conductivity and thickness of the Si bulk substrate are λ_1 and L_1 respectively, that of the linearly graded $Si_{1-x}Ge_x$ bulk layer λ_2 and L_2respectively and that of the constant $Si_{1-x}Ge_x$ bulk layer λ_3 and L_3respectively, then, according to Fourier's law:

$$q=\lambda_1 A\frac{\Delta T1}{L_1}=\lambda_2 A\frac{\Delta T2}{L_2}=\lambda_3 A\frac{\Delta T3}{L_3}=\lambda A\frac{\Delta T_1+\Delta T_2+\Delta T_3}{L_1+L_2+L_3} \tag{3.53}$$

With$\Delta T1$, $\Delta T2$ and $\Delta T3$ temperature differences of the Si bulk substrate, linearly graded $Si_{1-x}Ge_x$ bulk layer and constant $Si_{1-x}Ge_x$ bulk layer respectively, A the area and λ the thermal conductivity of the whole sample (Si/ $Si_{1-x}Ge_x$ bulk).

Therefore, the thermal conductivity of the Si/ $Si_{1-x}Ge_x$ bulk is given by:

$$\lambda=\frac{\frac{q}{A}}{\frac{\Delta T_1+\Delta T_2+\Delta T_3}{L_1+L_2+Lh_3}}=\frac{\frac{q}{A}}{\frac{qL_1}{A\lambda_1}+\frac{qL_2}{A\lambda_2}+\frac{qL_3}{A\lambda_3}}=\frac{(L_1+L_2+L_3)\lambda_1\lambda_2\lambda_3}{L_1\lambda_2\lambda_3+L_2\lambda_1\lambda_3+L_3\lambda_1\lambda_2} \tag{3.54}$$

Given the thermal conductivity of Si and $Si_{0.8}Ge_{0.2}$ and assuming that the thermal conductivity of the linearly graded SiGe bulk (λ_2) layer is approximated by the thermal conductivity of $SiGe_{x/2}$ then we can calculate the thermal conductivity of the material sandwich based on eq. (3.54), given in Fig. 3.20.

As given in Fig 3.20, the thermal conductivity only depends on temperature for the lightly doped sample. However, the thermal conductivity has an obvious increase when the doping density increased to $\sim 10^{18}\mathrm{cm}^{-3}$, because the influence of the

electronic portion of the thermal conductivity can no longer be ignored for heavily doped material.

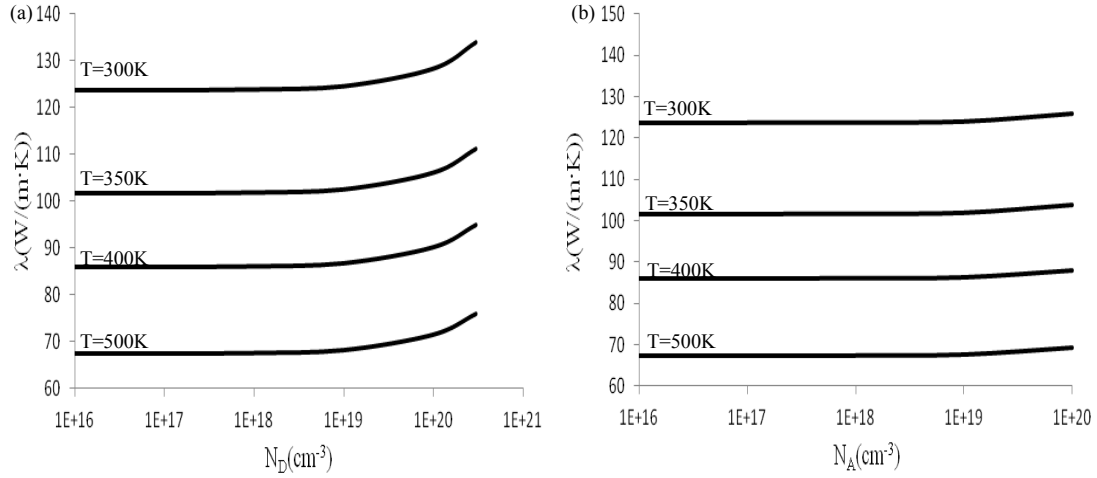


Figure 3.20: Thermal conductivity as a function of doping density and temperature for (a) n-type Si/$Si_{0.8}Ge_{0.2}$ bulk and (b) p-type Si/$Si_{0.8}Ge_{0.2}$ bulk.

These calculations show that the introduction of a relatively thin $Si_{1-x}Ge_x$ layer on top of bulk Si has only a small influence on the overall thermal conductivity.

② Seebeck coefficient of Si/ $Si_{1-x}Ge_x$bulk

Similar to the thermal conductivity, taking the Seebeck coefficients of Si bulk substrate, linearly graded $Si_{1-x}Ge_x$ bulk and constant $Si_{1-x}Ge_x$ bulk to be α_1, α_2 andα_3, respectively, the Seebeck coefficient of Si/ $Si_{1-x}Ge_x$ bulk is given by:

$$\alpha = \frac{\alpha_1\Delta T_1+\alpha_2\Delta T_2+\alpha_3\Delta T_3}{\Delta T_1+\Delta T_2+\Delta T_3} \tag{3.55}$$

With ΔT_1 the temperature difference of Si bulk substrate, ΔT_2 the temperature difference of linearly graded $Si_{1-x}Ge_x$ bulk and ΔT_3 the temperature difference of constant $Si_{1-x}Ge_x$ bulk.

The ratio of $\Delta T_1, \Delta T_2$ and ΔT_3 is given by:

$$\Delta T_1 : \Delta T_2 : \Delta T_3 = \frac{L_1}{\lambda_1} : \frac{L_2}{\lambda_2} : \frac{L_3}{\lambda_3} \tag{3.56}$$

Therefore, the Seebeck coefficient of Si/ $Si_{1-x}Ge_x$ bulk can be re-written as:

$$\alpha = \frac{\alpha_1\frac{L_1}{\lambda_1}+\alpha_2\frac{L_2}{\lambda_2}+\alpha_3\frac{L_3}{\lambda_3}}{\frac{L_1}{\lambda_1}+\frac{L_2}{\lambda_2}+\frac{L_3}{\lambda_3}} \tag{3.57}$$

The Seebeck coefficient of Si/$Si_{0.8}Ge_{0.2}$ bulk as a function of carrier concentration and temperature is given in Fig. 3.21. The Seebeck coefficient increases with temperature, and decreases with carrier concentration.

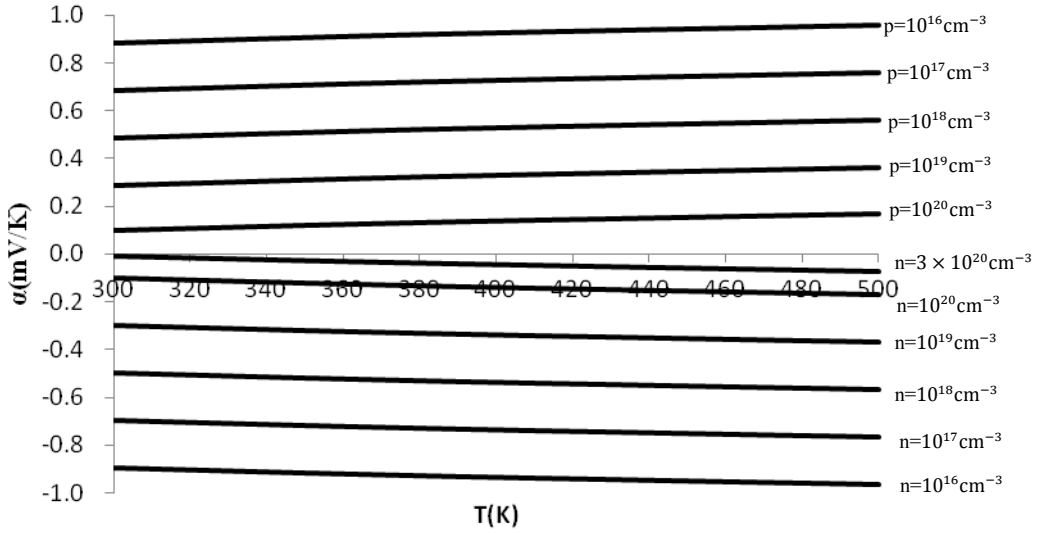


Figure 3.21: Seebeck coefficient as a function of doping density and temperature for n-type and p-type Si/$Si_{0.8}Ge_{0.2}$ bulk.

No apparent change with pure Si bulk can be observed.

③Electrical conductivity of Si/ $Si_{1-x}Ge_x$bulk

Taking the electrical conductivity of Si bulk substrate, linearly graded $Si_{1-x}Ge_x$ bulk and constant $Si_{1-x}Ge_x$ bulk as σ_1,$\sigma_2$and σ_3, respectively, the total resistance of Si/ $Si_{1-x}Ge_x$ bulk is given by:

$$R = \frac{1}{\sigma_1}\frac{L_1}{A} + \frac{1}{\sigma_2}\frac{L_2}{A} + \frac{1}{\sigma_3}\frac{L_3}{A} = \frac{1}{\sigma}\frac{L_1+L_2+L_3}{A} \tag{3.58}$$

With σ the electrical conductivity of Si/ $Si_{1-x}Ge_x$ bulk and A the area.

The electrical conductivity of Si/ $Si_{1-x}Ge_x$ bulk is given by:

$$\sigma = \frac{L_1+L_2+L_3}{\frac{L_1}{\sigma_1}+\frac{L_2}{\sigma_2}+\frac{L_3}{\sigma_3}} \tag{3.59}$$

The electrical conductivity of Si/$Si_{0.8}Ge_{0.2}$ bulk as a function of doping density and temperatures is given in Fig. 3.22.

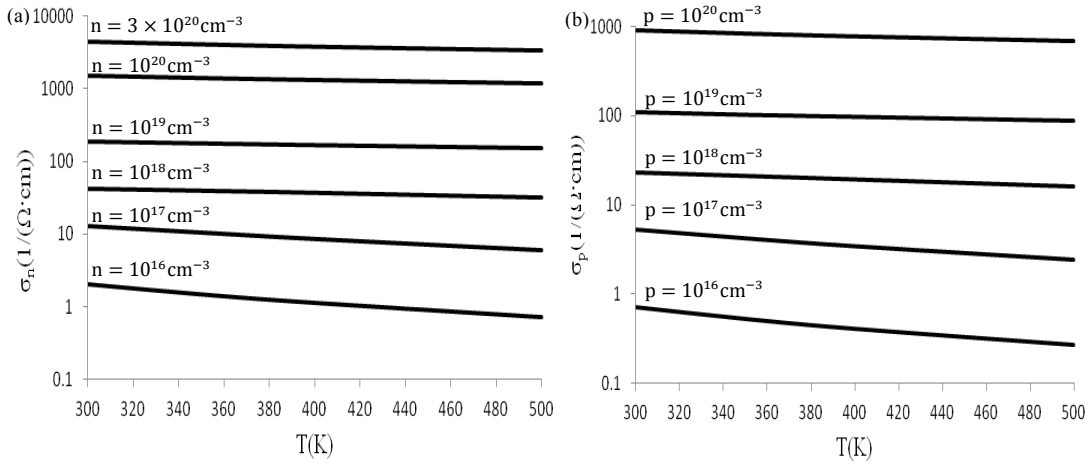


Figure 3.22: Electrical conductivity as a function of doping density and temperature for (a) n-type Si/$Si_{0.8}Ge_{0.2}$ bulk and (b) p-type Si/$Si_{0.8}Ge_{0.2}$ bulk.

④ ZT of Si/ $Si_{1-x}Ge_x$ bulk

According to the Seebeck coefficient, electrical conductivity and thermal conductivity model, we can get Si/$Si_{0.8}Ge_{0.2}$ bulk's ZT model, given in Fig. 3.23.

As shown in Fig. 3.23, Si/$Si_{0.8}Ge_{0.2}$ bulk's ZT is a doping density and temperature dependent function. p-type Si/$Si_{0.8}Ge_{0.2}$ bulk reaches the highest ZT when its doping density is~$10^{19}cm^{-3}$. n-type Si/$Si_{0.8}Ge_{0.2}$ bulk also reaches the highest ZT when its doping density is~$10^{20}cm^{-3}$. ZT of n-type Si bulk is higher than the one of p-type Si bulk under the same conditions.

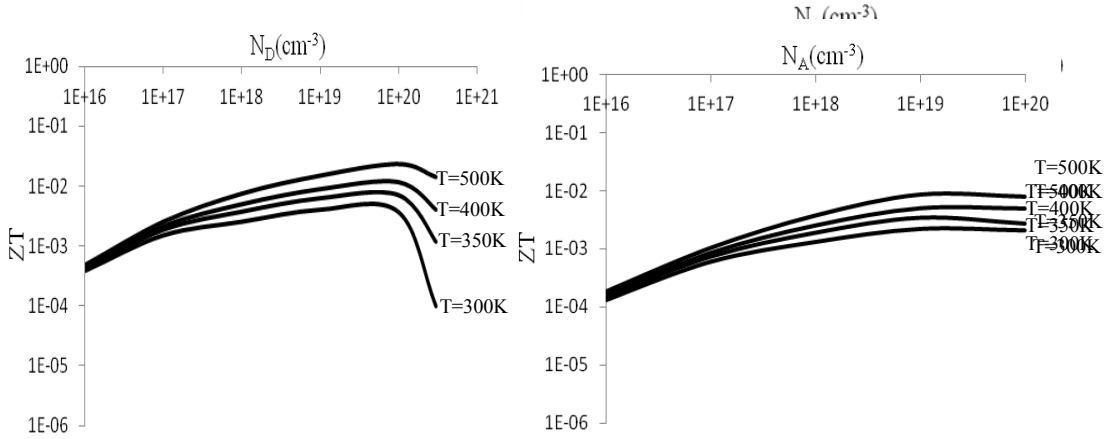


Figure 3.23: ZT as a function of doping density and temperature for (a)n-type Si/$Si_{0.8}Ge_{0.2}$ bulk and (b)p-type Si/$Si_{0.8}Ge_{0.2}$ bulk.

3.1.2: ZT of Si NWs at room temperature (T=300K)

As a kind of promising thermoelectric material, Si NWs have already been introduced roughly in Section 2.2 due to its much lower thermal conductivity(λ) and higher Seebeck coefficient(α) (Hochbaum, Chen & Delgado et al., 2008), (Krali & Durrani, 2013).

Seebeck coefficient (α) of Si NWs can be increased by quantum confinement of electrons without excessively affecting electrical conductivity (σ) and furthermore, thermal conductivity (λ) may be reduced independently of the other parameters by either increased surface scattering of phonons or modification of the density-of-states (Krali & Durrani, 2013).

According to the data measured by Krali & Durrani (Krali & Durrani, 2013), Seebeck coefficient of Si NWs is related to temperature and NWs length under fixed doping density. It is observed maximum $\alpha_{NWs} \sim 3\alpha_{bulk}$ at room temperature with the length of NWs is$35\mu m$, and the NWs are fabricated by MACE.

According to the descriptions about Si NWs thermal conductivity in Section 2.2, Si NWs thermal conductivity is NWs diameter, porosity and fabrication method dependent. According to the data given in (Hochbaum, Chen & Delgado et al., 2008), Si NWs thermal conductivity is reduced to $8W/m \cdot K$ at room temperature, which is much smaller than Si bulk's thermal conductivity($\sim 150W/m \cdot K$) at room temperature.

It is supposed that the electrical conductivity (σ) of Si NWAs is the same as Si bulk's thermal conductivity. Thus, its relation with doping density obeys the same rule as Si bulk's thermal conductivity.

Therefore, ZT of the Si sample, which is with $35\mu m$ NWs on the top of $465\mu m$ bulk, as a function of doping density can be gotten at room temperature(T=300K) via the methods described in eq. (3.54, 3.57 and 3.59).

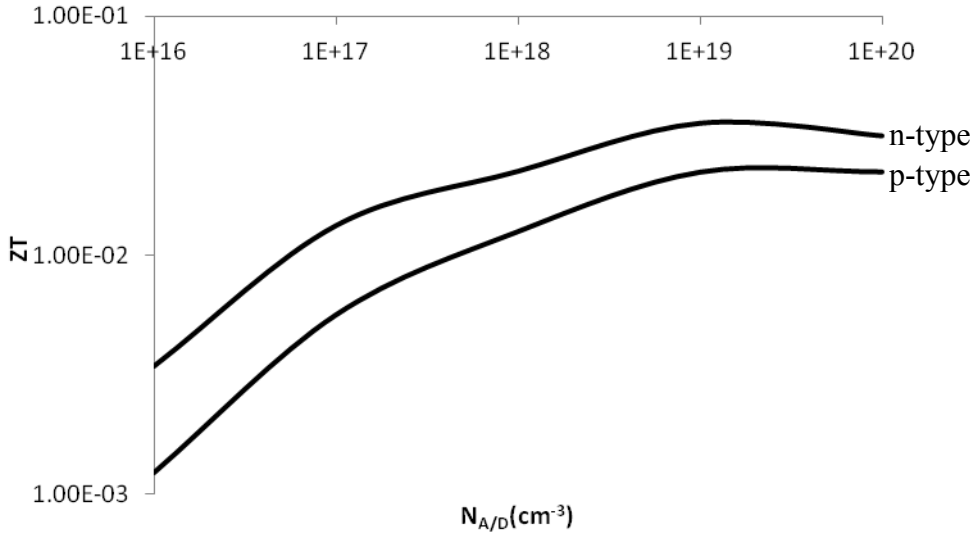


Figure 3.24: ZT of Si bulk/NWs sample as a function of doping density at room temperature.

ZT of n-type sample is higher than the one of p-type, furthermore, the maximum ZT is gotten when doping density is $\sim 10^{19} cm^{-3}$. These two properties are the same as the ones of Si bulk and $Si_{0.8}Ge_{0.2}$ bulk.

3.1.3: Conclusions

We have presented theoretical ZT model of Si bulk as a function of temperature and doping density. Theoretical ZT model Si/$Si_{1-x}Ge_x$bulk as a function of temperature, doping density and Ge fraction also has been given. In addition, theoretical ZT model of Si bulk/NWs as a function of doping density at room temperature has been presented.

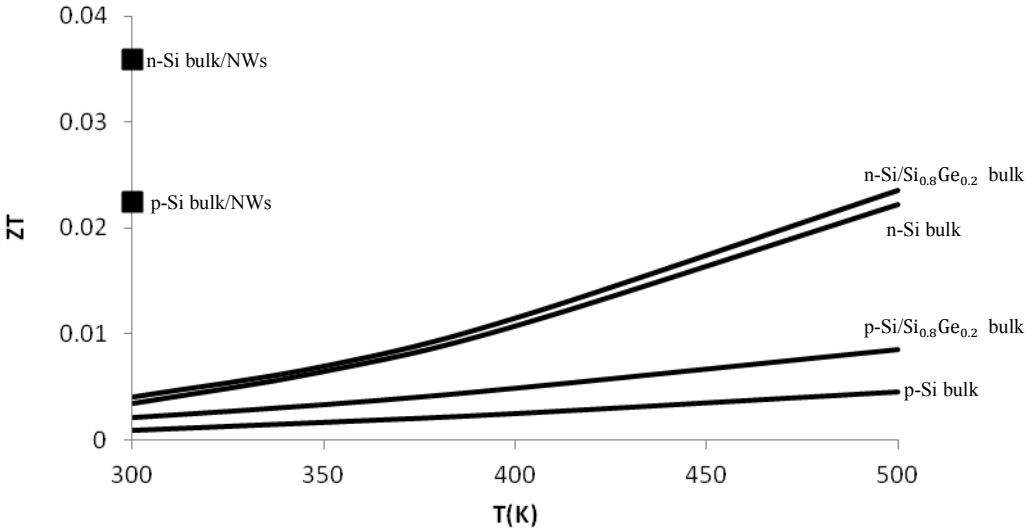


Figure 3.25: Highest ZT of Si bulk, Si/$Si_{0.8}Ge_{0.2}$ bulk and Si bulk/NWs as a function of temperature. The doping density of n-Si bulk and n-Si/$Si_{0.8}Ge_{0.2}$ bulk with highest ZT is$10^{20}cm^{-3}$, and the doping density of remaining samples with highest ZT is$10^{19}cm^{-3}$.

As the summaries given in Fig.3.25, ZT of n-type sample is always higher than the one of p-type under the same circumstance due to electron's higher mobility; the applications of Si NWs and $Si_{0.8}Ge_{0.2}$ bulk boost ZT due to their lower thermal conductivity, in addition, Si NWs have higher Seebeck coefficient due to electrons confinement; furthermore, ZT of Si/$Si_{0.8}Ge_{0.2}$ bulk is slightly higher than the one of Si bulk due to the extremely thin layer of $Si_{1-x}Ge_x$ layer in contrast to Si layer, and ZT of Si bulk/NWs is much higher than the one of Si bulk because of long Si NWs. However, ZT of Si bulk/NWs is much lower than 1 which has been realized by Si NWs. The reason is that the length of NWs in Si bulk/NWs sample is 35μm, which only accounts for 7% of the total thickness of Si bulk/NWs sample.

This section demonstrates that the poor thermoelectric property of Si bulk can be improved by the application of Si NWs and $Si_{1-x}Ge_x$ alloy from the aspects of ZT.

3.2: TEG's theoretical output power

As described in Chapter1, instead of ZT, we use output power to characterize the TEG's performance in our research. In this Section, we will present the theoretical

output power for the different material structures investigated: Si bulk, Si/SiGe bulk and Si bulk/NWs. Moreover, as the measurement set-up shown in Fig. 2.11, due to the fragile character of the Si NWAs under shear strain, the set-up for power measurements includes Cu blocks for the electrical and temperature probes. This means that at the interfaces, electrical and thermal contact resistances will occur which will restrict power output. In this section, we will discuss more accurate output power model which is with multi-layer in order to characterize the influences of thermoelectric material and the interfaces between Cu block and thermoelectric material.

The TEG measured by the set-up shown in Fig.2.11, is modeled as a five-layer structure: Cu block-intermediate layer-thermoelectric material (Si bulk, Si/SiGe bulk and Si bulk/NWs)-intermediate layer-Cu block, which is shown in Fig. 3.26. It is assumed that the intermediate layer is with thickness of$1\mu m$, and its electrical conductivity and thermal conductivity are $\sigma_i$and λ_i, but with 0 Seebeck coefficient. The influence of Cu block is ignored due to its extremely high electrical and thermal conductivity as well as its extremely low Seebeck coefficient.

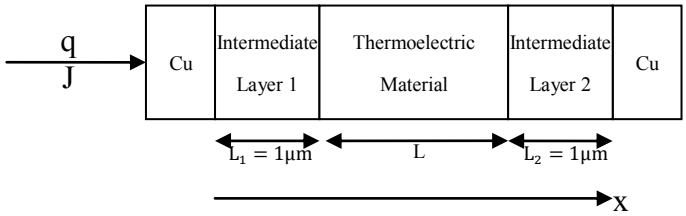


Figure 3.26: Schematic of five-layer structure with cross section area of $2cm \times 2cm$.

The output power model is given by eq. (1.26), which is determined by α, σ_{TEG} and ΔT. σ_{TEG} reflects the overall electrical conductivity of 2 intermediate layers and 1 thermoelectric material layer. According to eq. (3.59), overall electrical conductivity σ_{TEG} can be described by each layer's thickness and electrical conductivity. α is the Seebeck coefficient, and it is equal to thermoelectric material's Seebeck coefficient, because Seebeck coefficient of intermediate layer is supposed as 0. ΔT is the temperature difference across the thermoelectric material, which is determined by heat flux q and its thermal conductivity λ_{TE}, because the temperature difference across the intermediate layers cannot generate any Seebeck voltage.

Therefore, the output power of TEG which is shown in Fig.3.26 is:

$$P = \frac{\alpha_{TE}^2 \left(\frac{L+L_1+L_2}{\frac{L_1}{\sigma_i}+\frac{L}{\sigma_{TE}}+\frac{L_2}{\sigma_i}}\right)^2 \left(\frac{qL}{A\lambda_{TE}}\right)^2 R_L}{R_L^2 \left(\frac{L+L_1+L_2}{\frac{L_1}{\sigma_i}+\frac{L}{\sigma_{TE}}+\frac{L_2}{\sigma_i}}\right)^2 + \left(\frac{L}{A}\right)^2 + 2R_L \left(\frac{L+L_1+L_2}{\frac{L_1}{\sigma_i}+\frac{L}{\sigma_{TE}}+\frac{L_2}{\sigma_i}}\right)\left(\frac{L}{A}\right)} \quad (3.60)$$

With α_{TE} the Seebeck coefficient of thermoelectric material, σ_{TE} the electrical conductivity of thermoelectric material, λ_{TE} the thermal conductivity of

thermoelectric material, σ_i the electrical conductivity of intermediate layer, R_L the load resistance, A the cross section area(2cm×2cm).

Firstly, it is supposed that thermoelectric material is a 500μm thick n-type Si bulk whose doping density is $10^{19}\mathrm{cm}^{-3}$. At room temperature, its Seebeck coefficient α_{TE} is $0.3\mathrm{mV/K}$, its electrical conductivity σ_{TE} is $185\frac{1}{\Omega\cdot\mathrm{cm}}$, and its thermal conductivity λ_{TE} is $1.48\frac{\mathrm{W}}{\mathrm{cm}\cdot\mathrm{K}}$. The thickness L is 500μm, L_1 is 1μm, and L_2 is 1μm. Eq. (3.60) is simplified as:

$$P=\frac{0.09\left(\frac{502}{\frac{2}{\sigma_i}+\frac{500}{185}}\right)^2\left\{\frac{q\times10^{-4}\times500}{4\times1.48}\right\}^2 R_L}{R_L^2\left(\frac{502}{\frac{2}{\sigma_i}+\frac{500}{185}}\right)^2+\left(\frac{500\times10^{-4}}{4}\right)^2+2R_L\left(\frac{502}{\frac{2}{\sigma_i}+\frac{500}{185}}\right)\left(\frac{500\times10^{-4}}{4}\right)} \tag{3.61}$$

As the output power model given in eq. (3.61), the output power as a function of load resistance R_L depends on the electrical conductivity of intermediate layer σ_i and heat flux q,which is supposed as 1W.

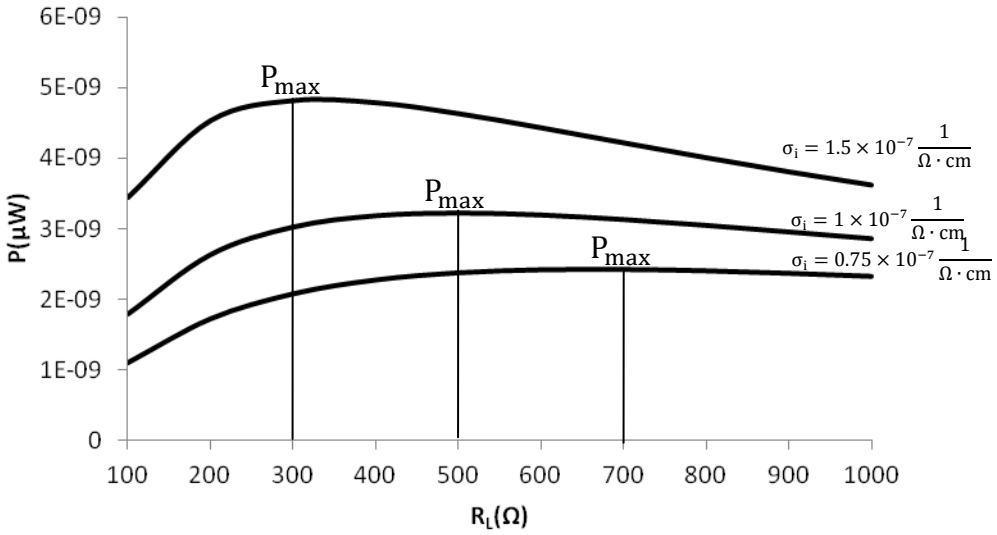


Figure 3.27: TEG's output power as a function of load resistance with different electrical conductivities of intermediate layers.

As the figure shown in Fig. 3.27, TEG's output power increases with the increasing of intermediate layer's electrical conductivity, furthermore, the load resistance R_L which matches TEG's maximum output power P_{max} increases with the decreasing of intermediate layer's electrical conductivity. Thus, the electrical conductivity of intermediate layer affects TEG's output power and internal resistance.

Secondly, it is supposed that the electrical conductivity of intermediate layer is fixed at $1.5\times10^{-7}\frac{1}{\Omega\cdot\mathrm{cm}}$, and the heat flux q is set at 1W. The thermoelectric material is

n-type $Si/Si_{0.8}Ge_{0.2}$ bulk whose doping density is $10^{19}cm^{-3}$. Its thickness is 506μm, electrical conductivity is $186\frac{1}{\Omega\cdot cm}$, thermal conductivity is $1.25\frac{W}{K\cdot cm}$, and Seebeck coefficient is 0.3mV/K. TEG's output power as a function of load resistance is simplified as:

$$P=\frac{0.09\left(\frac{508}{\frac{2}{1.5\times10^{-7}}+\frac{506}{186}}\right)^2\left\{\frac{10^{-4}\times506}{4\times1.25}\right\}^2R_L}{R_L^2\left(\frac{508}{\frac{2}{1.5\times10^{-7}}+\frac{506}{186}}\right)^2+\left(\frac{506\times10^{-4}}{4}\right)^2+2R_L\left(\frac{508}{\frac{2}{1.5\times10^{-7}}+\frac{506}{186}}\right)\left(\frac{506\times10^{-4}}{4}\right)} \quad (3.62)$$

Thirdly, it is still supposed that the electrical conductivity of intermediate layer is fixed at$1.5\times10^{-7}\frac{1}{\Omega\cdot cm}$, and the heat flux q is set at 1W. The thermoelectric material is n-type Si/Si NWAs whose doping density is $10^{19}cm^{-3}$. Its thickness is 500μm, (465 μm bulk + 35μm NWAs) electrical conductivity is $186\frac{1}{\Omega\cdot cm}$, thermal conductivity is $0.67\frac{W}{K\cdot cm}$, and Seebeck coefficient is 0.66mV/K. TEG's output power as a function of load resistance is simplified as:

$$P=\frac{0.4356\left(\frac{502}{\frac{2}{1.5\times10^{-7}}+\frac{500}{186}}\right)^2\left\{\frac{10^{-4}\times500}{4\times0.67}\right\}^2R_L}{R_L^2\left(\frac{502}{\frac{2}{1.5\times10^{-7}}+\frac{500}{186}}\right)^2+\left(\frac{500\times10^{-4}}{4}\right)^2+2R_L\left(\frac{502}{\frac{2}{1.5\times10^{-7}}+\frac{500}{186}}\right)\left(\frac{500\times10^{-4}}{4}\right)} \quad (3.63)$$

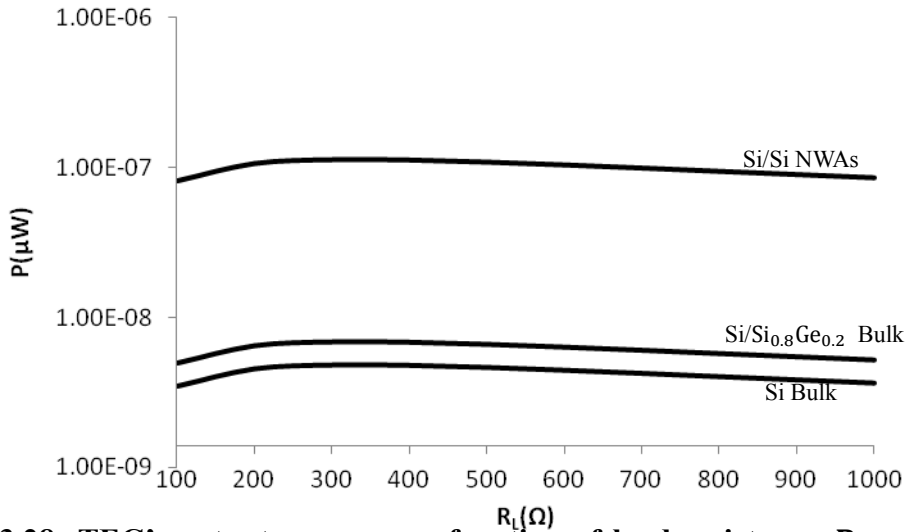


Figure 3.28: TEG's output power as a function of load resistance R_L with the same intermediate layer and different thermoelectric materials.

As the figure shown in Fig.3.28, these three TEGs have the same intermediate layer whose electrical conductivity is $1.5\times10^{-7}\frac{1}{\Omega\cdot cm}$, furthermore, they have different

thermoelectric materials which have almost the same electrical conductivity$\sim 185\frac{1}{\Omega\cdot cm}$, so the internal resistances of these three TEGs are almost the same. But the thermal conductivity of thermoelectric material is decreased by the application of $Si/Si_{0.8}Ge_{0.2}$ bulk and Si/Si NWAs, which causes higher temperature difference across the thermoelectric material. The Seebeck coefficient is increased by the application of Si/Si NWAs, so TEG's output power is increased by higher Seebeck voltage without affecting internal resistance.

From the figures shown in Fig. 3.27 and 3.28, it can be concluded that TEG's output power depends on intermediate layer and thermoelectric material at the same time: intermediate layer mainly affects the internal resistance of TEG, and thermoelectric material with the same doping density mainly affects the Seebeck voltage of TEG.

3.2.1: Temperature distribution in TEG

Temperature distribution in TEG can be split into two parts: one is the temperature distribution at the Cu-thermoelectric material boundary interface which is a sudden temperature drop, and the other one is the temperature distribution inside the thermoelectric material.

The temperature distribution at the Cu-thermoelectric material boundary interface can be demonstrated using COMSOL (Uk.comsol.com, 2014) simulations. As shown in Fig. 3.26, heat is transferred from hot Cu to cold Cu via Cu-thermoelectric material boundary interfaces(intermediate layers) and thermoelectric materials which are heated from an original low temperature to a final steady state high temperature if the heat flux into the setup is constant. The TEG is considered at equilibrium when it reaches a final steady high temperature. At steady state we focus on the temperature drop at the Cu-thermoelectric material boundary interfaces.

Due to surface roughness, the Cu-thermoelectric material contact surfaces touch only at discrete locations in real systems, interspersed with void spaces. The void spaces are usually filled with air (Cooper, Mikic & Yovanovich, 1969). Thus some heat flow through contact points and some across the voids (Chapman, 1987), (Gmelin, Asen-Palmer & Reuther et al., 1999). This creates an apparent temperature drop between the two materials at the contacts. The temperature drop is governed by the heat flux and thermal contact resistance, which is given by (Chapman, 1987):

$$\frac{q}{A} = \frac{\Delta T}{R_{tc}} \tag{3.64}$$

With q the heat flux, A the contact area, ΔT the temperature drop at the contact and R_{tc} is thermal contact resistance.

The utility of the thermal contact resistance concept depends on the availability of reliable numerical values. Metallic contact resistance depends on the metals involved, the surface roughness, the contact pressure, the material occupying the void spaces,

and the temperature (Chapman, 1987).

A simple model was written in COMSOL to demonstrate the temperature drop that occurs at the interface of two solid objects, shown in Fig.3.29. One small Cu block is placed on a big table. The table's temperature is constant (293.15 K), because it is very large ($200\times200\times5mm^3$) compared to the Cu block ($20\times20\times5mm^3$). A thermal contact resistance layer is assigned between Cu and table, with a layer thickness of 0.005 m and thermal conductivity of $100\ W/(m\cdot k)$. Finally, the Cu block's temperature can reach a steady state by a constant input heat flux (80 W). Actually, this model is similar to our real set-up in the lab, because the TEG is also placed on a big table in our lab. The simulation results are shown in Fig.3.30.

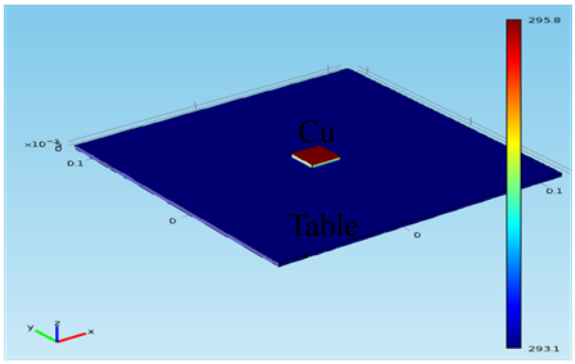


Figure 3.29: Model in COMSOL.

As shown in Fig.3.30, the table's temperature is a constant, kept at 293.15 K along the red line shown in the left graph. There is a sudden temperature drop at the Cu-table contact, the temperature drops from 303.27 K to 293.15 K due to the thermal contact resistance. The temperature also varies along the red line inside the Cu block, the temperature drops from 305.77 K to 303.27 K due to the finite thermal conductivity of Cu which is $401\frac{W}{m\cdot K}$.

If eq. (3.64) is applied at the Cu-table interface, as shown in eq. (3.65), then we obtain a heat flux of 80.96 W, which is the same as heater's power (Chapman, 1987).

$$q = \frac{1}{R_{tc}}A(T1 - T2) = \frac{100\frac{W}{m\cdot K}}{0.005m} \times 0.0004cm^2 \times (303.27K - 293.15K) = 80.96\ W \quad (3.65)$$

(b)

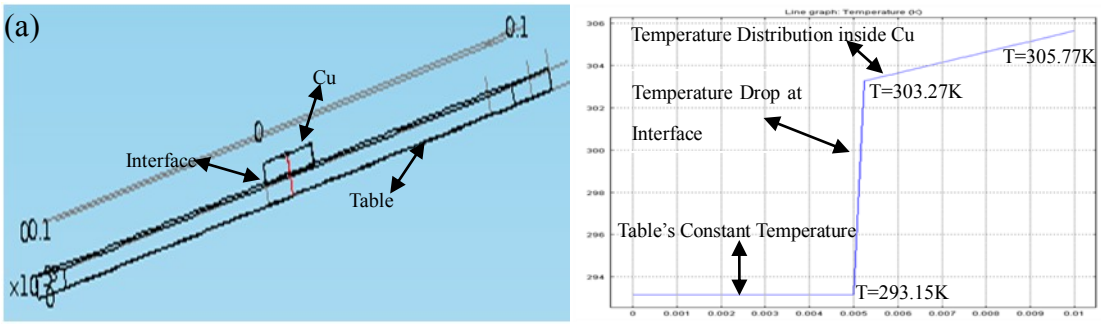


Figure 3.30: COMSOL simulation of temperature distribution. (a): the cross section of Fig. 3.29; (b) the temperature distribution along the red solid line in (a).

The second point is the tempeature distribution inside thermoelectric material, which has already been given in eq. (1.20). It is supposed that thermoelectric material is n-type Si bulk whose doping density is 10^{19}cm^{-3} with thickness of 500μm, together with q=1W, $T_c = 300\text{K}$,$\sigma_i = 1.5 \times 10^{-7}\frac{1}{\Omega\cdot\text{cm}}$ and the currency density given in eq.(1.25) give the temperature distribution in thermoelectric material in Fig 3.31.

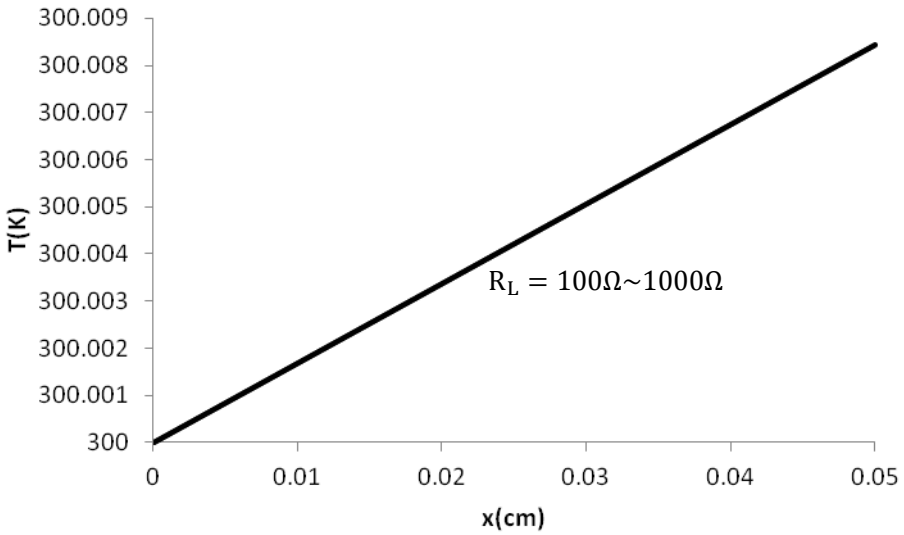


Figure 3.31: Temperature distribution along thermoelectric material which is n-type Si bulk whose doping density is10^{19}cm^{-3}, as well as with thickness of $500\mu\text{m}$ and area of4cm^2. The intermediate layer's electrical conductivity is$1.5 \times 10^{-7}\frac{1}{\Omega\cdot\text{cm}}$.

As the figure given in Fig. 3.31, the temperature along thermoelectric material is linear distribution, and it is independent of load resistance R_L this is because the Thompson effect is ignored.

3.2.2: Voltage distribution in TEG

The voltage distribution in TEG is given by eq. (1.22), and the current density J is

given by eq. (1.25), so the voltage distribution in TEG depends on load resistance R_L and intermediate layer's electrical conductivity σ_i under fixed heat flux and thermoelectric material.

The voltage distribution in TEG with different load resistance R_L and different intermediate layer's electrical conductivity σ_i is shown in Fig. 3.32.

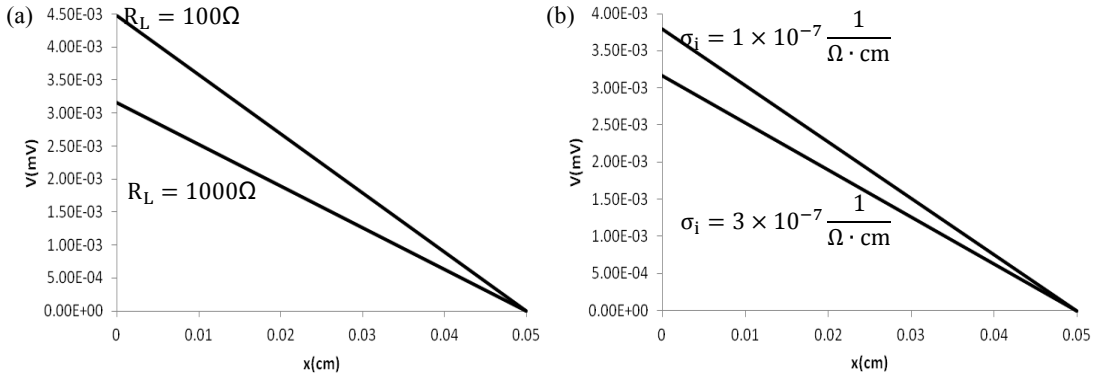


Figure 3.32: The voltage distribution in TEG whose thermoelectric material is n-type Si bulk with doping density of $10^{19}cm^{-3}$, as well as thickness of$500\mu m$, area of $4cm^2$ and the heat flux is 1W. (a): as a function of load resistance with $\sigma_i = 1.5 \times 10^{-7} \frac{1}{\Omega \cdot cm}$; (b): as a function of intermediate layer's electrical conductivity σ_i with $R_L = 500\Omega$.

As shown in Fig. 3.32, the voltage distribution in thermoelectric material is strongly dependent on the load resistance and intermediate layer's electrical conductivity.

As the figures shown in Fig. 3.27 and 3.32(b), intermediate layer's electrical conductivity affects TEG's output power and voltage distribution inside TEG, and it is determined by the contact between Cu and thermoelectric material. Taking Si as the example of thermoelectric material, the contact resistance which reflects the intermediate layer's electrical conductivity will be researched in the following.

The electrical contact between Cu and Si can be divided into two types: Ohmic and Schottky contact. The classification can be identified by the energy band diagram given in Fig. 3.33(Turner&Rhoderick,1968).

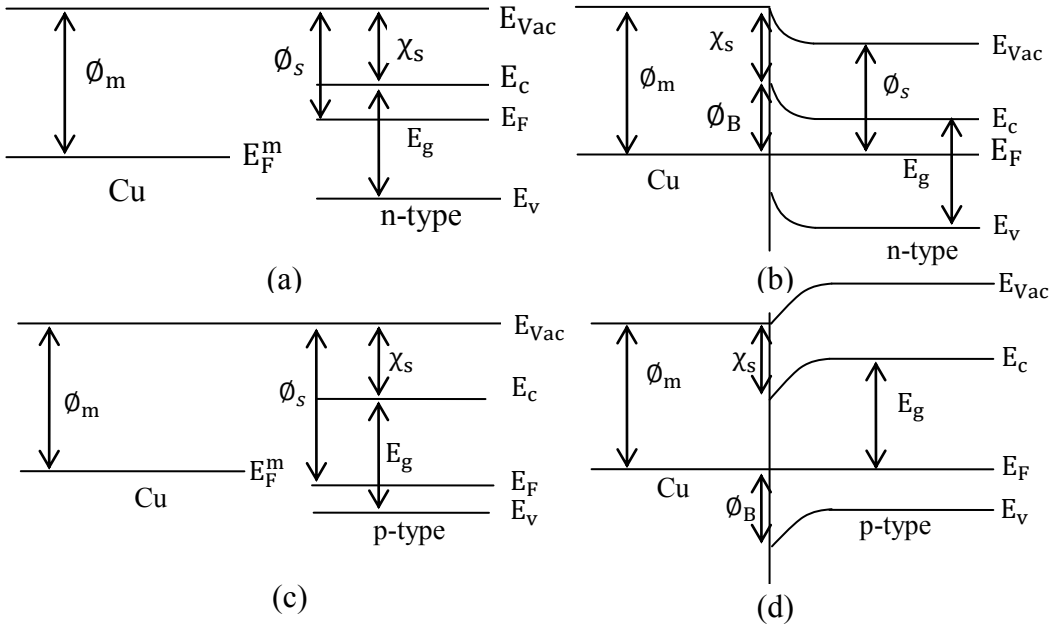


Figure 3.33: (a): Energy band diagrams of Cu and n-type Si; (b): Schottky contact at Cu/n-type Si contact; (c): Energy band diagrams of Cu and p-type Si; (d): Schottky contact at Cu/p-type Si contact (Turner & Rhoderick, 1968).

$\emptyset_m$ is Cu's work function. $\emptyset_s$ is Si's work function. χ_s is the electron affinity. $\emptyset_B$ is the Schottky barrier height. E_g is the band gap.

1: Ohmic contact

A Cu-Si contact results in an Ohmic contact if the Schottky barrier height is zero or negative. In such case, the carriers are free to flow in or out of the semiconductor with minimal resistance (Anderson, Anderson & Deng et al., 2008). The contact will also behave as Ohmic if the barrier is thin enough, discussed in next section.

An Ohmic contact between Cu and n-type Si can be formed if $\emptyset_m < \emptyset_s$; the Ohmic contact between Cu and p-type Si can be formed if $\emptyset_m > \emptyset_s$. The work function of Cu is 4.65 eV; the electron affinity of Si is 4.05 eV and the energy gap of Si is 1.12 eV at room temperature (Anderson, Anderson & Deng et al., 2008).

For n-type Si, the work function is given by Fobelets (Fobelets, 2010):

$$\emptyset_s = 4.05 - kTln\left(\frac{n}{N_c}\right) \tag{3.66}$$

For p-type Si, the work function is given by Fobelets (Fobelets, 2010):

$$\emptyset_s = 4.05 + 1.12 + kTln\left(\frac{p}{N_v}\right) \tag{3.67}$$

At room temperature, the variation of $\emptyset_s$ as a function of carrier concentration is given in Fig. 3.34.

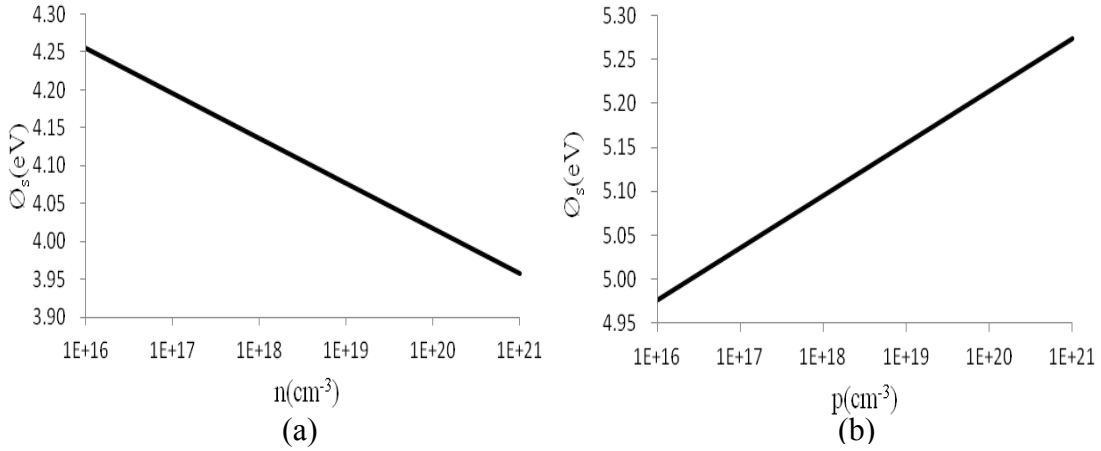


Figure 3.34: Si's work function as a function of carrier concentration at room temperature. (a): n-type Si ;(b): p-type Si.

As shown in Fig. 3.34, the work function of n-type Si decreases with increasing carrier concentration. Thus, an Ohmic contact between Cu and n-type Si is not possible. The work function of p-type Si increases with increasing carrier concentration, again hindering Ohmic contact formation.

2: Schottky contact:

A Cu-Si contact results in a Schottky contact if the Schottky barrier is positive. As analyzed above, the contact between Cu and Si is always a Schottky contact. Fortunately, an Ohmic contact can be achieved when the carrier concentration is high enough. High carrier concentration causes the depletion region width to become smaller, allowing the carriers to tunnel through the barrier, and thus decreasing the contact resistance (Turner&Rhoderick,1968).

.

Three different current flow mechanisms can occur in Schottky contacts: thermionic emission (TE), thermionic-field-emission (TFE) and field emission (FE) (Yu, 1970).

Before introducing the above three current flow mechanisms, one useful characteristic energy (E_{00}) must be defined in advance (Yu, 1970) :

$$E_{00} = \frac{eh}{4\pi}\sqrt{\frac{N}{m^*\epsilon}} \tag{3.68}$$

With N the doping density which is equal to carrier concentration approximately, m^* the carrier effective mass, ϵ Si's dielectric constant, e unit charge and h Planck's constant respectively.

(1): TE ($kT/E_{00} \gg 1$):

The depletion width is wide when the Si is lightly doped. The only way the carriers can get into the metal is by thermionic emission over the Schottky barrier height $\emptyset_B$. The ideal current flow is given by Schroder (Schroder, 1998), (Turner & Rhoderick, 1968):

$$I = AA^*T^2 \exp\left(-\frac{e\emptyset_B}{kT}\right)\left[\exp\left(\frac{eV}{kT}\right) - 1\right] \tag{3.69}$$

With A the contact area, A^* the Richardson's constant, T the temperature, $\emptyset_B$ the Schottky barrier height, V the applied voltage, k and e are the Boltzmann constant and the unit charge respectively.

The corresponding specific contact resistance R_c is given by:

$$R_c = \frac{\partial V}{\partial J}|_{V\to 0} = \frac{k}{A^* T e}\exp\left(\frac{e\emptyset_B}{kT}\right) \tag{3.70}$$

As indicated in eq. (3.70), the ideal specific contact resistance for TE is strongly dependent on Schottky barrier height at room temperature. It is independent of doping density.

(2): TFE ($kT/E_{00}\sim 1$):
The Si is heavily doped, so that the depletion width is narrower. Thermionic emission and field emission happen at the same time (Padovani & Stratton, 1966). The ideal specific contact resistance R_c is given by Yu (Yu, 1970):

$$R_c = \frac{\partial V}{\partial J}|_{V\to 0} = \left[\frac{k}{A^* T e}\right]\frac{kT}{\left[\sqrt{\pi(\emptyset_B + U_F)E_{00}}\right]}\cosh\left(\frac{E_{00}}{kT}\right)\left[\sqrt{\coth\left(\frac{E_{00}}{kT}\right)}\right]\exp\left(\frac{\emptyset_B + U_F}{E_0} - \frac{U_F}{kT}\right) \tag{3.71}$$

E_0 is a measure of the tunneling probability in the TFE region, it is given by Yu (Yu, 1970):

$$E_0 = E_{00}\coth\left(\frac{E_{00}}{kT}\right) \tag{3.72}$$

For n-type Si, U_F is (Yu, 1970):

$$U_F = E_F - E_C \tag{3.73}$$

For p-type Si, U_F is (Yu, 1970):

$$U_F = E_V - E_F \tag{3.74}$$

Eq. (3.71) is valid if $\frac{\cosh^2\left(\frac{E_{00}}{kT}\right)}{\sinh^3\left(\frac{E_{00}}{kT}\right)} < \frac{2(\emptyset_B + U_F)}{3E_{00}}$.

As indicated in eq. (3.71), the ideal specific contact resistance in the TFE case is strongly dependent on the Schottky barrier height and E_{00} which depends on doping density.

(3): FE ($kT/E_{00} \ll 1$):
The Si is degenerately doped. The depletion width is thin, so that the current is based on carrier tunneling. The specific contact resistance is given by Yu (Yu, 1970):

$$R_c = \frac{\partial V}{\partial J}|_{V\to 0} = \left[\frac{A^* T \pi e}{k\sin(\pi C_1 kT)}\exp\left(\frac{-\emptyset_B}{E_{00}}\right) - \frac{A^* C_1 e}{C_1^2 k^2}\exp\left(\frac{-\emptyset_B}{E_{00}} - C_1 U_F\right)\right]^{-1} \tag{3.75}$$

With C_1 is given by Yu (Yu, 1970):

$$C_1 = \frac{1}{2E_{00}} \ln\left(\frac{4\emptyset_B}{U_F}\right) \tag{3.76}$$

Eq. (3.75) is valid if $1 - C_1 kT > kT(\sqrt{2f_1})$, f_1 is given by Yu (Yu, 1970):

$$f_1 = \frac{1}{4E_{00}U_F} \tag{3.77}$$

As indicated in eq. (3.75), the ideal specific contact resistance R_c for FE is also strongly dependent on Schottky barrier height and E_{00} which depends on doping density.

The ideal specific contact resistance as a function of doping density and Schottky barrier heights is given in Fig. 3.35.

The solid lines in Fig. 3.35 are based on eq. (3.70, 3.71 and 3.75). The solid lines have discontinuity between TE and TFE region, the reason is that R_c has a sudden drop from TE region to TFE region. For example, R_c of Cu and n-type Si is 16.55 $\Omega \cdot cm^2$ if the Schottky barrier height is 0.6 eV and doping density is $4 \times 10^{17} cm^{-3}$ (TE region). R_c of Cu and n-type Si is 4.64 $\Omega \cdot cm^2$ if the Schottky barrier height is 0.6 eV and doping density is increased to $5 \times 10^{17} cm^{-3}$ (TFE region). The markers in Fig. 3.35 are the measurement values from Yu (Yu, 1970). The measurement values are consistent with the theoretical model.

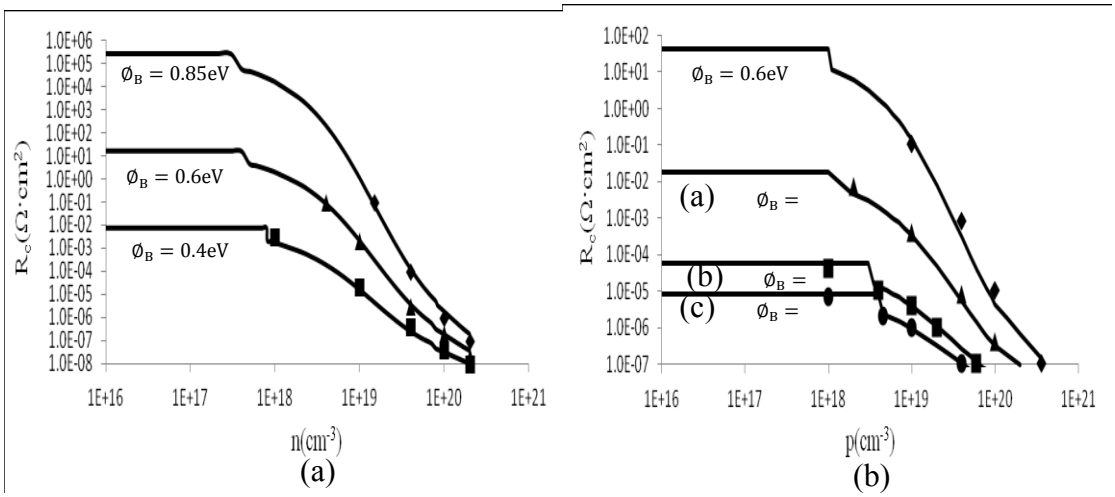


Figure 3.35: Ideal specific contact resistance as a function of doping density with different Schottky barrier heights. (a): Cu and n-type Si contact, $m^* = 0.26m_0$, $\epsilon = 11.8\epsilon_0$,T=300K, A=4 cm^2 , $A^* = 200\frac{A}{cm^2 \cdot K^2}$, $N_C = 2.8 \times 10^{19} cm^{-3}$. (b): Cu and p-type Si contact, $m^* = 0.6m_0$, $\epsilon = 11.8\epsilon_0$, T=300K, A=4$cm^2$, $A^* = 79\frac{A}{cm^2 \cdot K^2}$, $N_V = 3.1 \times 10^{19} cm^{-3}$ (Chang, Fang & Sze, 1971).

As indicated in Fig. 3.35, the doping density has no influence on R_c if the current flow mechanism is TE. R_c decreases with increasing doping density if the current

flow mechanism is TFE or FE. The Schottky barrier height plays an important role in R_c: R_c increases with an increasing Schottky barrier height if the doping density is a constant, but its influence decreases with increasing doping density.

As shown in Fig. 3.35, R_c is a function of doping density and Schottky barrier height. Actually, this is an ideal situation, because the ideality factor (n_0) is ignored in this model. The ideality factor (n_0) incorporates all those unknown effects making the contact non-ideal. Thus, n_0 is always larger than 1 (Schroder, 1998).

Eq. (3.69) describes the ideal current flow by TE. If the ideality factor (n_0) is taken into account, the current flow can be given by Schroder (Schroder, 1998):

$$I = AA^*T^2 \exp\left(-\frac{e\emptyset_B}{kT}\right)\left[\exp\left(\frac{eV}{n_0 kT}\right) - 1\right] \quad (3.78)$$

If we compare eq. (3.69) and eq. (3.78), the ideality factor (n_0) has a big influence on the current magnitude, the actual current is always smaller than the ideal current because $n_0 > 1$. The difference between actual and ideal current increases with increasing ideality factor (n_0), for constant applied voltage (V). The difference also increases with the increase of applied voltage (V) if the ideality factor (n) is a constant.

The corresponding specific contact resistance R_c is given by:

$$R_c = \frac{\partial V}{\partial J}\Big|_{V\to 0} = \frac{n_0 k}{A^* Te} \exp\left(\frac{e\emptyset_B}{kT}\right) \quad (3.79)$$

Thus, the specific contact resistance R_c is also increased by an ideality factor n_0.

Based on the analysis of ZT and contact resistance, the doping density in thermoelectric material needs to be sufficiently high. However, MACE cannot be effectively be used on Si with high doping density which will be discussed in Chapter 4. Therefore, in order to improve both the doping density for good ZT and low R_c, spin-on-doping will be used.

3.3: Spin-on-doping (SOD)

As a thermoelectric material, lightly doped Si does not have a good performance. The first reason is that its ZT, which is a doping density dependent parameter, is low. The second reason is the existence of large contact resistance between Cu and Si. Increasing the doping density of lightly doped Si via SOD is an important way to enhance the TEG's performance via higher ZT and smaller contact resistance.

The SOD process consists of two stages: dopants source spinning and thermal diffusion into Si.

1: Dopant source

The dopant source is boron for p-type Si, and phosphorus for n-type Si. The dopant source, which provides doping ingredients in a thermal diffusion process, can be solid, liquid or gaseous. Amongst these techniques, the use of spin-on-glass (SOG) films which contain dopants and which are deposited on processed Si (Mathiot, Lachiq & Slaoui et al., 1998), is an attractive approach because coating with glass films is a simple process and causes no damage. The doped SOG solution, which contains ethyl alcohol as a solvent is dropped onto the Si surface and rotated at high speed to make a homogenous layer. It is subsequently baked on a hot plate to remove the solvents. The SOD can be diluted with methanol or isopropanol to modify viscosity and obtain controlled film thickness (Mathiot, Lachiq & Slaoui et al., 1998).

2: Thermal diffusion

Currently, rapid thermal processing (RTP) and classical isothermal processing (CIP) are most common thermal diffusion methods. RTP can be used to reduce thermal redistribution of impurities at high temperature. For small devices this is an important consideration and as a result most engineers make use of low temperature process. Some ion implants require high temperature of ~1000℃ thus RTP is a promising technology (Usami, Ando & Tsunekane et al., 1992). RTP uses radiation from a tungsten halogen lamp as a heat source (Zagozdzon-Wosik, Grabiec & Lux, 1994), (Usami, Ando & Tsunekane et al., 1992). Typically, RTP consists of a rise in temperature in a few seconds, then a plateau at a temperature with time duration from a few seconds to a few minutes, followed by a rapid cool off in a matter of seconds. In this process, problems include temperature measurement and thermal uniformity of the wafer. Excessive temperature gradients across the wafer cause thermoplastic stress that may lead to wafer warpage or slip (Hebb & Jensen, 2014). CIP is performed in an open tube furnace under argon (Ar) flow in the same temperature range as RTP for a typical duration from minutes to hours. The open tube furnace design consists of a cylindrical cavity surrounded by heating coilsthat are embedded in a thermally insulating matrix. Temperature can be controlled via feedback from a thermocouple. Its temperature distribution is more uniform.

Diffusion of the dopants from the SOD into the Si is done by one of these two methods, and the extremely high temperature pushes the dopants diffuse into Si under the protection of Ar or N_2 flow, leaving a silica film layer behind due to the impossible full protection of Ar or N_2 flow. Finally, the doping density of Si is increased by dopants diffusion, and the deposited silica-film glass is removed by a 5 minutes buffered HF etching.

3. Parameters that influences the SOD process of phosphorous

The recipe of the SOD process influences the carrier concentration distribution, diffusion depth, sheet resistance etc.

(1): The influence of dopant concentration in the SOD solution

The influence of the dopant concentration in the SOD solution is characterized by the

sheet resistance. This can be measured on the processed wafers by using the four-point probe method after stripping the silica SOD layer in a buffered HF solution.

The sheet resistance as a function of P dopants concentration in SOD is given in Table 3.3 (Mathiot, Lachiq & Slaoui et al., 1998). The Si wafers were spun with SOD with different phosphorous concentrations at a speed of 9900 rpm/min for 15 s, followed by a prebaking at 200℃ for 15 min using a hot plate before placing them into RTP furnace. RTP was carried out at 850℃ for 25 s. All parameters except source concentration is kept constant in this experiment.

Phosphorus Concentration(cm^{-3})	Sheet Resistance(Ω/sq)
4.5×10^{19}	700
5×10^{20}	200
2×10^{21}	40

Table 3.3: Sheet resistance of Si after SOD as a function of phosphorus concentration (Mathiot, Lachiq & Slaoui et al., 1998).

Table 3.3 confirms the decrease of sheet resistance with the increase of phosphorus concentration in the SOD solution. The doping in Si is limited by the supply of phosphorous from the SOD source layer (Mathiot, Lachiq & Slaoui et al., 1998).

(2): The influence of RTP duration

The RTP thermal cycle consists of a quick rise in temperature followed by a constant temperature plateau for a few seconds to a few minutes. This time duration affects the phosphorous concentration at the Si surface, which determines the contact resistance between Cu and Si and is quite important in our research.

In the experiment of Mathiot et al (Mathiot, Lachiq & Slaoui et al., 1998), secondary ion mass spectrometry (SIMS) is used to determine the surface concentration of P in the Si substrate as a function of the RIP time duration at 850℃. The concentration of P in the SOD solution is $3 \times 10^{20} cm^{-3}$. Four different time duration of 10 s, 25 s, 60 s and 90 s were used and the P surface concentration in Fig. 3.36 can be fitted by Mathiot, Lachiq & Slaoui et al. (Mathiot, Lachiq & Slaoui et al., 1998):

$$C_{surf} = 3 \times 10^{20} \left[1 + \exp\left(-\frac{t}{7.35}\right)\right] (cm^{-3}) \quad (3.80)$$

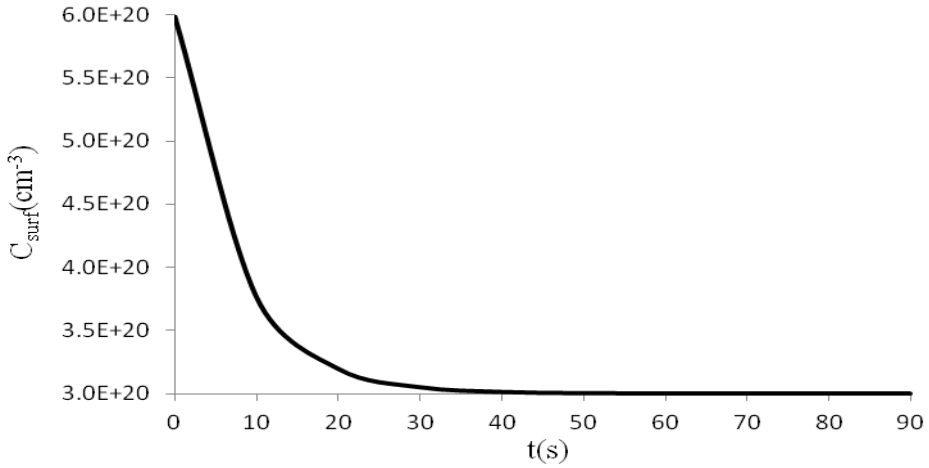


Figure 3.36: Phosphorous concentration at the Si surface as a function of RTP time duration (Mathiot, Lachiq & Slaoui et al., 1998).

As given in Fig. 3.36, the phosphorous concentration at the Si surface decreases with the increasing RTP time duration.

(3): The influence of the RTP temperature

In the experiment of Mathiot et al. (Mathiot, Lachiq & Slaoui et al., 1998), the influence of the RTP temperature is characterized by sheet resistance. Four different RTP temperatures were used and all other recipes in the SOD process were kept the same (Mathiot, Lachiq & Slaoui et al., 1998). The Si wafers were spun at a speed of 9900 rpm/min for 15 s with the same phosphorous solution of concentration $2 \times 10^{21} \mathrm{cm}^{-3}$, followed by a prebaking at 200℃ for 15 min using a hot plate before placing them into rapid thermal processing (RTP) furnace. RTP was carried out for 25 s at four different RTP temperatures. Their experimental results are given by in Table 3.4.

RTP Temperature(℃)	Sheet Resistance(Ω/sq)
850	40
900	20
950	12
1000	8

Table 3.4: Sheet resistance of Si after SOD as a function of RTP temperature (Mathiot, Lachiq & Slaoui et al., 1998)

The sheet resistance decreases sharply with an increase in the processing temperature. This behavior is caused by the diffusion and subsequent activation of phosphorous atoms into Si.

In the experiment of Hartiti et al. (Hartiti, Slaoui & Muller et al., 1992), the influence of the RTP temperature is characterized by the carrier concentration distribution profile inside Si after SOD. Carrier concentration profiles, which were obtained by an automatic resistivity Hall stripping technique (ARHS), only take the electrically active phosphorous concentration into account.

The samples were coated with a 200 nm thick phosphorous-doped silica film containing a high dopant concentration of $1 \times 10^{21} \mathrm{cm}^{-3}$. The samples were prebaked at 100℃ for 15 min using a hot plate just before placing them in the RTP furnace. The processing time in the RTP furnace is fixed at 25s, and the RTP temperature varies from 850℃ to 1000℃. According to the ARHS measurement results, which are given in Fig. 3.37, the surface concentration increases with temperature, then tends to become saturated for high temperatures. This behavior can be attributed to an increase in the solubility of phosphorous into Si when increasing the diffusion temperature. A maximum surface concentration of about $9 \times 10^{20} \mathrm{cm}^{-3}$ at 1000 ℃ is obtained, a value very close to the solid solubility of phosphorous in Si at this temperature. In contrast, a much lower surface concentrations of $1 \times 10^{20} \mathrm{cm}^{-3}$ is measured at a temperature of 850 ℃(Hartiti, Slaoui & Muller et al., 1992).

The diffusion depths extracted from the measured profiles are seen to increase when the thermal budget is increased. At the processing temperature of 850 ℃, the diffusion depth is very small (≈ 0.03 μm). At the highest temperature (1000 ℃), the diffusion depth reaches 0.35 μm(Hartiti, Slaoui & Muller et al., 1992).

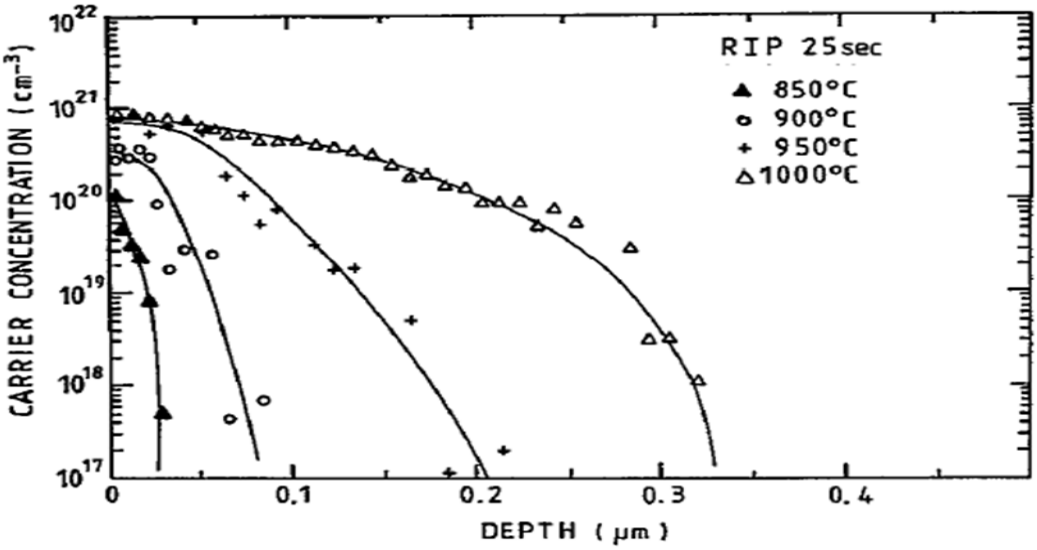


Figure 3.37: Electrically active phosphorous concentration profiles by ARHS measurement for SOG/Si samples RTP annealed for 25s at 850℃, 900℃, 950℃ and 1000℃(Hartiti, Slaoui & Muller et al., 1992).

4. Parameters that influences the SOD process of boron

Boron diffusion is done by CIP. It is assumed that the boron density in the source is sufficiently high. Firstly, the surface boron concentration is determined by the solubility of boron in Si which is temperature dependent (Vick & Whittle, 1969). As shown in Fig. 3.38, boron's solubility in Si increases with temperature. Secondly, the boron's dopant profile inside Si is temperature and diffusion time dependent, which is given in Fig. 3.39. The figures in Fig. 3.39 also demonstrate boron's solubility in Si increases with temperature, but independent of diffusion time. Boron's diffusion depth

in Si increases with temperature and diffusion time at the sam time

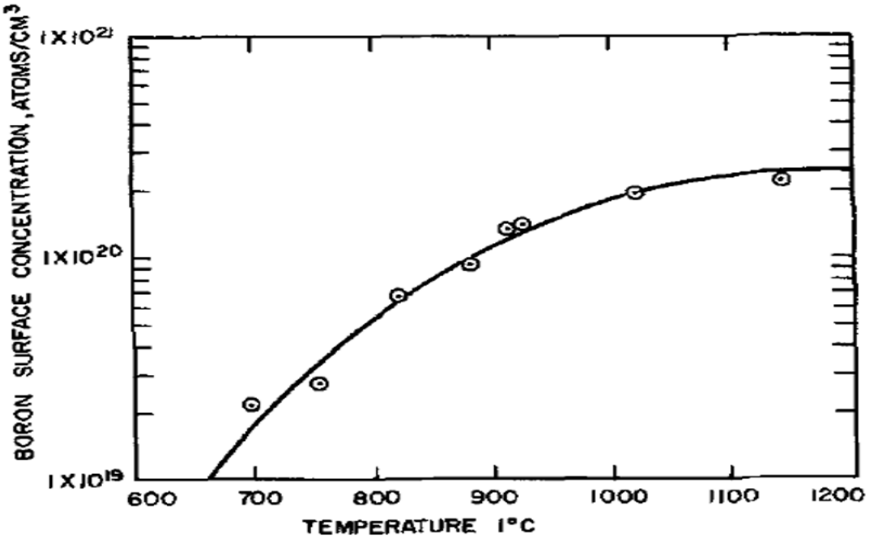


Figure 3.38: Boron's solubility in Si as a function of temperature (Vick & Whittle, 1969). The circles are the measurement values and the solid line is the regression line.

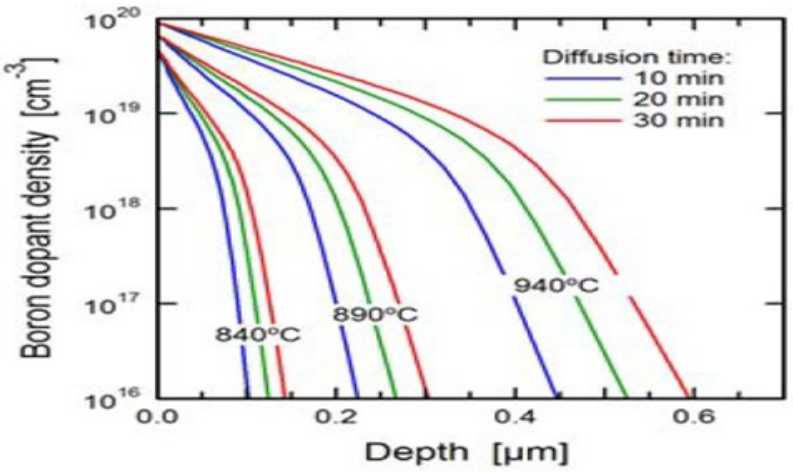


Figure 3.39: Boron's dopant profile in Si as a function of temperature and diffusion time (Wehmeier, Schraps & Wagner et al., 2013).

3.4: Conclusions

This chapter firstly describes ZT of Si bulk, which only reflects the characteristics of thermoelectric material and is dependent on temperature and doping density. Temperature and doping density affect the Seebeck coefficient, electrical conductivity and thermal conductivity of thermoelectric material. Meanwhile, the thermal conductivity can also be decreased by alloy scattering as in $Si_{1-x}Ge_x$ and by nano structures as in the Si NWAs which have limited influence on electrical conductivity. Furthermore, $Si_{1-x}Ge_x$ has little influence on Seebeck coefficient, but Si NWAs increases Seebeck coefficient due to electrons confinement.

The TEG's output power reflects the characterization of the whole TEG system, including all parasitic components. In order to describe TEG's output power accurately, TEG system is split into two parts: thermoelectric material and intermediate layer which takes account of all parasitic components. The TEG's output power is affected by the characteristics of thermoelectric material, as well as electrical conductivity of intermediate layer which is a pretty significant factor that affects TEG's output power, and it is reflected by Cu-Si contact resistance which can be increased by increasing the surface doping concentration. This will be done by spin-on-doping. The different techniques applied to n and p-type spin-on-doping was discussed.

Chapter 4: Material preparation

The materials used in our research are Si bulk and its nano-structures and Si/$Si_{1-x}Ge_x$ bulk and its nano-structures. The nanostructures are fabricated using metal assisted chemical etching (MACE). The influence of the doping density on the quality of the MACE fabricated nanowire arrays (NWAs) is studied as well as the influence of spin-on-doping and sputter coated contacts.

4.1: Si bulk and its nanostructures

As the most common material in the semiconductor industry, Si is preferred in our research due to its low cost and abundance. Of course, Si bulk is a poor thermoelectric material, and this has already been demonstrated by its low ZT. Its poor thermoelectric character can however be manipulated by the conversion of a part of the Si bulk into Si NWAs. Phonon scatterings at the nanowire boundaries reduce the thermal conductivity in the Si NWAs (Mingo, Yang & Li et al., 2003).

4.1.1: Si bulk

Four types of commercial Si bulk have been used in our research: p-type (1-5 $\Omega \cdot$ cm), p-type (0.01-0.02 $\Omega \cdot$ cm), n-type (1-10 $\Omega \cdot$ cm) and n-type (0.01-0.02 $\Omega \cdot$ cm). The bulk thickness is 500 μm and their crystal orientation is (100). Si NWAs are fabricated from these bulk materials.

4.1.2: Si NWAs

Si NWAs are fabricated by MACE, which has already been introduced in Section 2.4. As the description in Section 2.4 explains, two types of MACE are widely used. Amongst them, two-step reaction is preferred in our research for Si NWAs.

The recipe we use consists of the following steps: Ag NPs are first deposited on the Si surface in a $AgNO_3$(0.06M), HF (40%), H_2O solution, followed by an etching in an HF (40%) and oxidizing agent mixture. The etching is catalyzed by the Ag NPs. For the Si NWAs prepared for these experiments we have used a HF (40%), H_2O, H_2O_2 (0.6M) solution. After etching, the residual Ag particles are removed by a solution of concentrated HNO_3 (5M).

In the output power measurements the Si NWAs will be clamped in order to reduce the thermal and electrical contact resistance. Therefore, the NWAs must be robust enough to bear the big pressure (~10^2 N) in our experiments. As described in Section

2.4, the quality of the wires depends on the doping density in the Si bulk, the concentration of etching solutions, the etching time and temperature. In the following, we will demonstrate that the concentration of etching solution needs to be adapted for different doping density and type via the SEM pictures of NWAs All SEM pictures in this section are taken after the NWAs are being pressed in the measurement process, and the SEM pictures are all taken from the 'fresh' sides of samples via cutting the samples before picture capture in SEM.

1: p-type Si (1-5 Ω· cm) and n-type Si (1-10 Ω· cm) NWAs etching:
In this case, for lightly doped Si, the recipe is the same for p- and n-type Si. Ag NPs are deposited in a $AgNO_3$(0.06M): HF (40%): H_2O solution with a volume ratio of 2:5:13 for 15 minutes. This causes a large density of Ag nanoparticles on the Si surface. Then Si NWAs are etched in a HF (40%):H_2O:H_2O_2 (0.6M) solution with a volume ratio of 1:1:2. The etch time controls the NWAs length (Li, Xu, Durrani& Fobelets, 2011). As given in Fig. 4.1, these two types of Si NWAs are robust enough to bear a big pressure (400 N), and they do not collapse after being pressed. In addition, the Seebeck voltage measurements on the Si NWAs fabricated with this technique are stable with a low offset voltage.

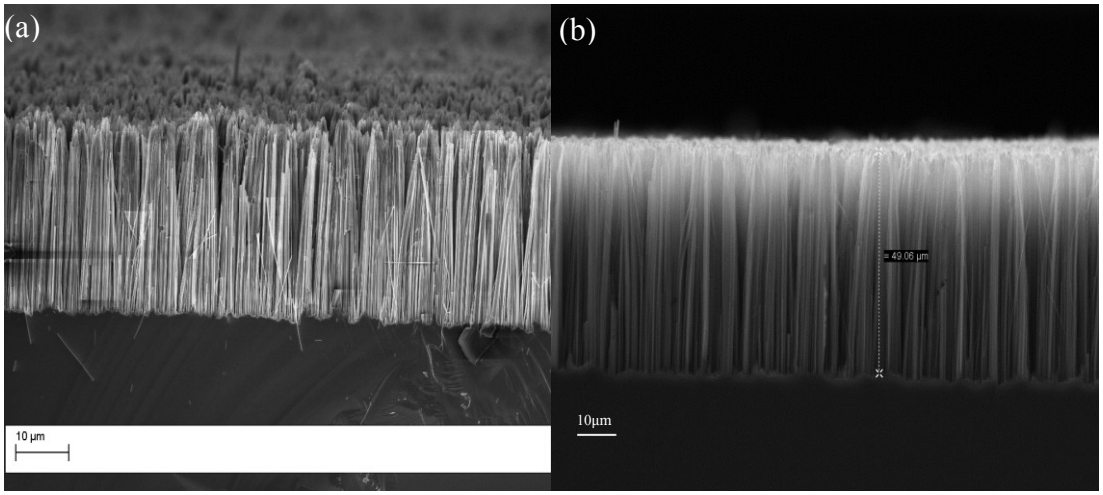


Figure 4.1: Si NWAS . (a): n-type (1-10 Ω· cm);(b): p-type (1-5 Ω· cm).

These kinds of robust NWAs always have very stable output voltage if the applied temperature difference is fixed, so that their Seebeck coefficients are easily measured.

2: p-type Si (0.01-0.02 Ω· cm) NWAs etching
If the same recipe is used to etch p-type Si (0.01-0.02 Ω· cm) NWAs as that for lightly doped Si, then the Si NWAs are not robust enough to bear the big pressure (400N). As shown in Fig. 4.2, they all collapse after being pressed.

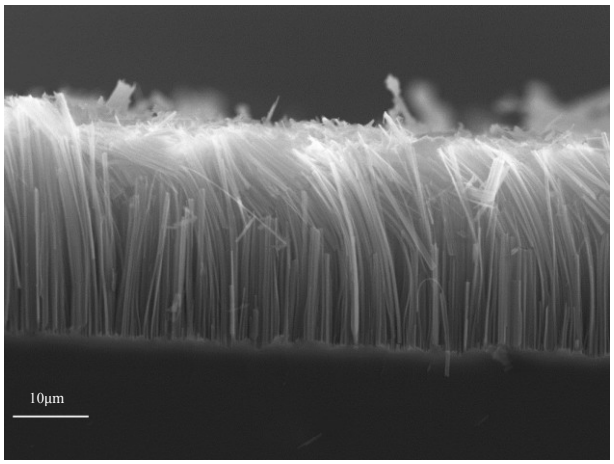


Figure 4.2: p-type Si (0.01-0.02Ω· cm) NWAs

As analyzed in Section 2.4, the amount of Ag ions in the solution must be controlled if the doping density of Si bulk is high. Otherwise, the Si NWs are very slender due to the tiny distance of two adjacent nanopits. Furthermore, the Si NWs become porous due to the lateral etching pathways on the side walls of the NWs.

Consequently, as given in Fig. 4.3, the output voltage of this kind of 'weak' Si NWA is not stable and the offset voltage is large, even if the applied temperature difference is fixed. Therefore, the Seebeck voltage cannot be determined from these samples.

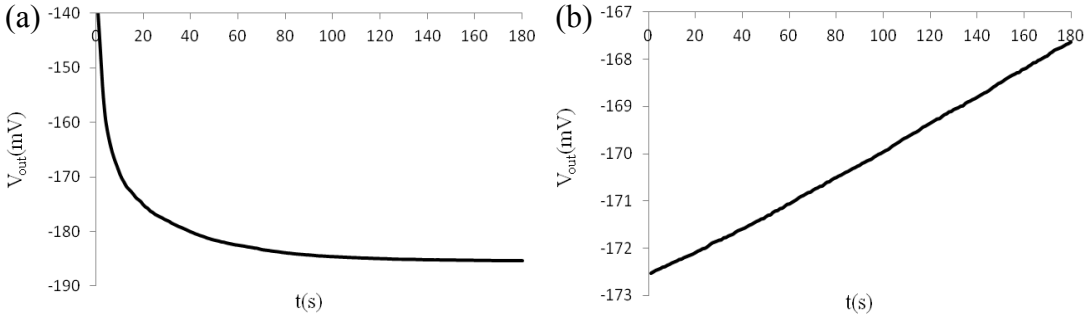


Figure 4.3: Output voltages of p-type Si NWAs as a function of time when a fixed temperature difference is applied. (a): p-type (0.01-0.02 Ω·cm), ΔT=0K;(b): p-type (0.01-0.02 Ω·cm), ΔT=9.8K.

The reason for this unstable and high voltage is the surface depletion of the Si NWs, shown in Fig. 4.4 (a). The surface charge on the SiO_2that surrounds the Si NW cores is influenced by the pH of the environment (Goyne, Zimmerman & Newalkar et al., 2002). The lab ambient has a relative humidity of ~70% with a pH of around 7. Thus the native SiO_2 surrounding the NWs has a positive surface charge density which will cause surface depletion in p-type doped wires (Kimukin, Islam & Williams, 2006). The positive surface charge density is much higher than the value measured for the Si bulk, and it is proportional to the doping density of Si (Kimukin, Islam & Williams, 2006). Thus, an unstable high output voltage, which is given in Fig. 4.3, is caused by the large amounts of NWAs positive surface charges which contact with the Cu contacts once the NWs collapse after being pressed, as shown in Fig. 4.4 (b). Furthermore, surface depletion/enhancement in Si nanowires can have a large influence on their electrical

conductivity as the depletion width, W can be of the same order of magnitude as the diameter of the nanowires. Surface depletion has led to increased Seebeck coefficients (α) for NWAs samples (Krali, Li & Fobelets et al., 2011). However, the associated reduction of the electrical conductivity of the wires leads to a lower power factor and thus poor thermoelectric performance. The problem caused by surface depletion can be solved by SOD which will be introduced in Section 4.3.

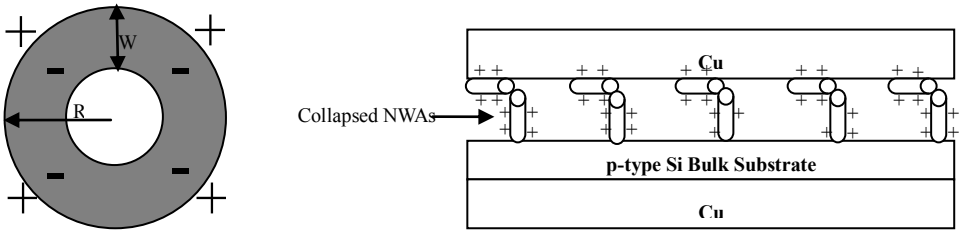


Figure 4.4 (a): Top view cross section of a single p-type Si nanowire. R is the NW radius and W is the depletion width due to the surface depletion. The white area is the remaining conduction path. (b): Schematic of collapsed p-type Si NWs which make large amounts of positive charges at the surface of the Cu contact.

In order to ensure robust, crystalline NWs the etch recipe for p-type (0.01-0.02 Ω· cm) Si NWAs is adapted to: Ag NPs are deposited in a $AgNO_3$ (0.06M): HF (40%): H_2O solution with a volume ratio of 4:10:33 for 1.5 minutes. This gives a small Ag nucleation density. The color of the Si surface changed from dark to colorful, which is like the color of rainbow due to light reflection on Si bulk surface's Ag film in the Ag deposition solution, indicating the formation of Ag nanoparticles on the surface of the Si pieces. Then Si NWAs are etched in a HF (40%):H_2O:H_2O_2 (0.6M) solution with a volume ratio of 13:37:10, the etch time controls the NWAs length. The $AgNO_3$ concentration has been decreased in this recipe, furthermore, the concentration of H_2O_2 has also been decreased, because with an increasing concentration of H_2O_2, the Si NWAs first become increasingly rough on the surface, then start to evolve porous shells surrounding the solid cores, and eventually form entirely porous NWAs (Zhang, Peng & Fan et al., 2008). Thus, the concentration of H_2O_2 must be decreased in order to avoid porous Si NWAs.

As shown in Fig. 4.5, p-type Si (0.01-0.02 Ω· cm) NWAs etched by this recipe are robust enough to bear the big pressure (400N), and they do not collapse after being pressed. Their Seebeck voltage is stable if the temperature difference is fixed.

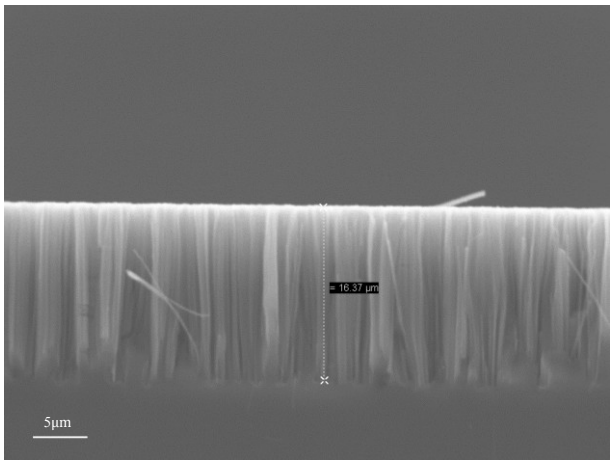


Figure 4.5: p-type Si (0.01-0.02 Ω· cm**) NWAs**

3: n-type Si (0.01-0.02 Ω·cm) NWAs etching
Two kinds of NWAs etching recipes have been introduced before, both of them can etch robust heavily doped n-type Si NWAs.

(1): n-type Si (0.01-0.02 Ω·cm) NWAs etched using heavy Ag nucleation
The n-type Si NWAs are given in Fig 4.6:

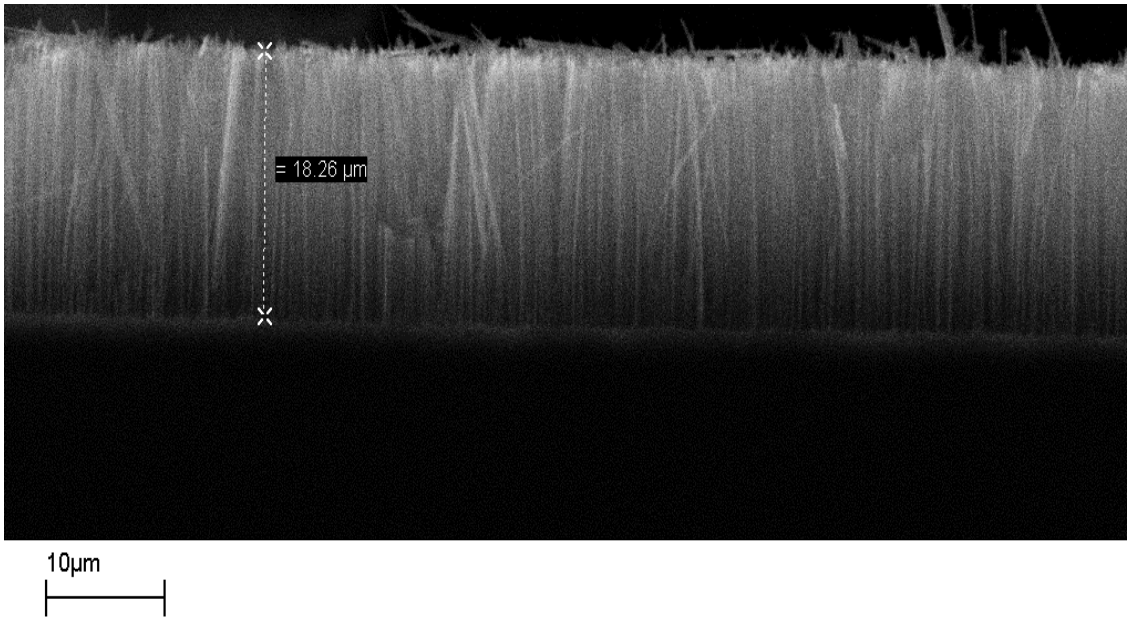


Figure 4.6: n-type Si (0.01-0.02 Ω·cm) NWAs (using heavy Ag nucleation).

As shown in Fig. 4.6, Si NWAs are robust enough to bear the big pressure (400N). Its output voltage is also very stable and the offset voltage is low if a fixed temperature difference is applied.

(b): n-type Si (0.01-0.02Ω·cm) NWAs etched by light Ag nucleation:
The n-type Si NWAs are given in Fig. 4.7:

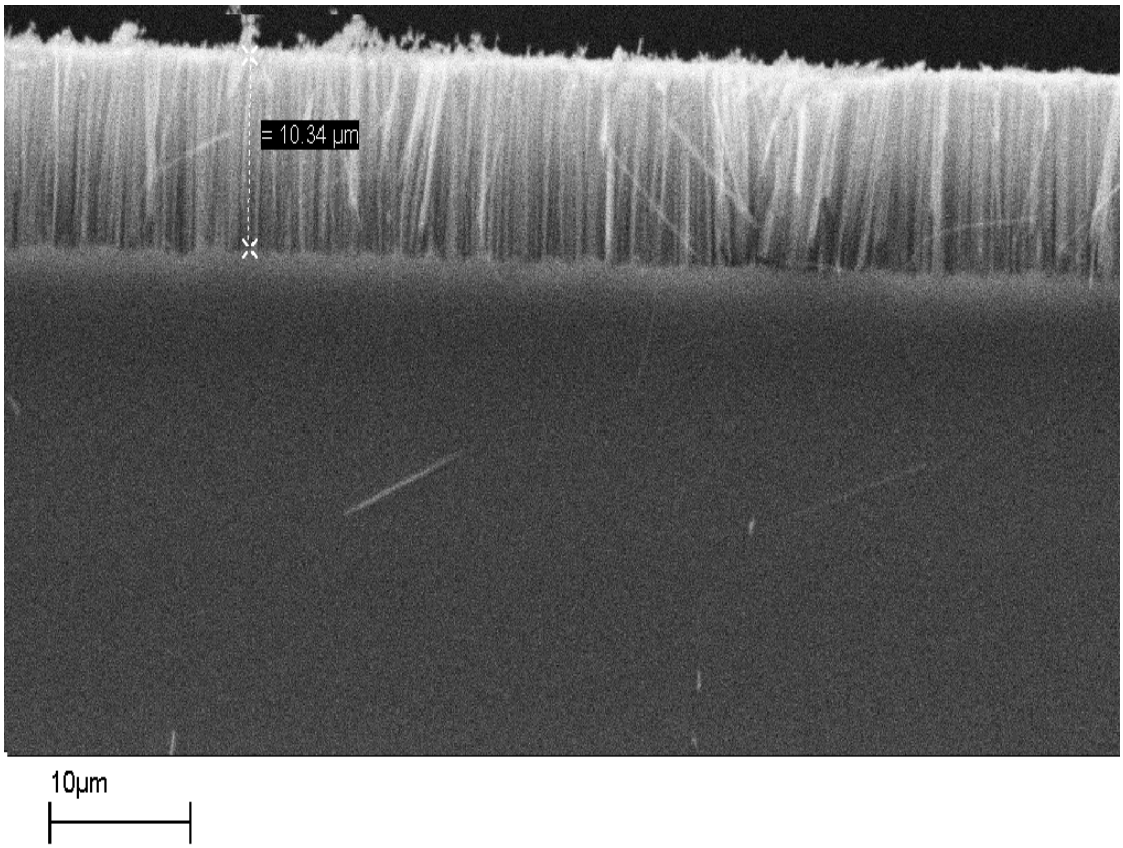


Figure 4.7: n-type Si (0.01-0.02 Ω·cm) NWAs (light Ag nucleation).

As shown in Fig. 4.7, Si nanowires are robust enough to bear the big pressure (400N). Its output voltage is very stable and the offset voltage is low, if a fixed temperature difference is applied.

4.2: Si/SiGe bulk and its nanostructures

As analyzed in Section 3.1.1, $Si_{1-x}Ge_x$ bulk has much lower thermal conductivity and higher ZT compared to Si bulk due to alloy scattering. It is traditionally used at temperatures around 1000 ℃ (Bhandari&Rowe,1980),(Slack & Hussain, 1991). It was shown that alloy scattering and interface effects in SiGe-containing nanowires reduce the thermal conductivity to very low levels in (Slack & Hussain, 1991). Therefore, the combination of $Si_{1-x}Ge_x$ and NWAs promises improvements in the thermoelectric properties of Si-based composites.

4.2.1: Si/SiGe bulk

The Si/$Si_{1-x}Ge_x$ bulk consists of a relaxed $Si_{1-x}Ge_x$ layer grown epitaxially on lightly doped p-Si (100) substrates using reduced-pressure chemical vapor deposition (Myronov, Liu & Dobbie et al., 2011). The resistivity of the p-Si substrate for the $Si_{1-x}Ge_x$-containing samples is 2.7 Ω·cm, measured by the four-point-probe (4pp)

technique (Schroder, 1998). A linearly graded relaxed $Si_{1-x}Ge_x$ layer (3μm) was deposited first to overcome the lattice mismatch between Si and $Si_{1-x}Ge_x$, followed by a 3 μm-thick constant composition layer. The $Si_{1-x}Ge_x$ layer is unintentionally p-doped.

4.2.2:Si/**SiGe** NWAs

$Si_{1-x}Ge_x$ NWAs are the nanowires etched into the $Si_{1-x}Ge_x$ layer towards the Si substrate. Two-step MACE is successfully used to etch Si NWAs However, $Si_{1-x}Ge_x$ is easily attacked by oxidizing agents such as H_2O_2, resulting in the fast removal of the $Si_{1-x}Ge_x$ layer during the etch process. We have adapted the one-step MACE process to avoid the removal of the $Si_{1-x}Ge_x$ layers during chemical etching of the $Si_{1-x}Ge_x$ NWAs. A single stage etch in a $AgNO_3$(0.06M) and HF (40%) solution with a volume ratio of 1:1 can be used for $Si_{1-x}Ge_x$ NWAs. We have demonstrated that arrays of $Si_{1-x}Ge_x$ with x up to 40% NWAs can be fabricated using this single stage method. Scanning electron microscopy (SEM) (Fig. 4.8(a)) and energy-dispersive X-ray (EDX) spectroscopy (Fig. 4.8 (b)) characterize the $Si_{1-x}Ge_x$-containing NWAs. The EDX results indicate that the $Si_{0.8}Ge_{0.2}$ NWAs are properly prepared with limited side etching using one-step MACE, even for longer etching times. EDX at the top of the NWs in the array (dot 1 in Fig. 4.8(a)) clearly indicates the presence of Ge. At ~6 μm depth (dot 2 in Fig. 4.8(a), the Ge peak is much reduced as it lies inside the Si bulk. We also demonstrated that the etch rate decreases with increasing Ge concentration for the same etch conditions, which is given in Fig. 4.8(c). For short etch time, as given in Fig. 4.8(c), the etch rate is limited by the Ge fraction. For longer etch times, the etch rate is limited by the supply of chemicals and Ag nanoparticles.

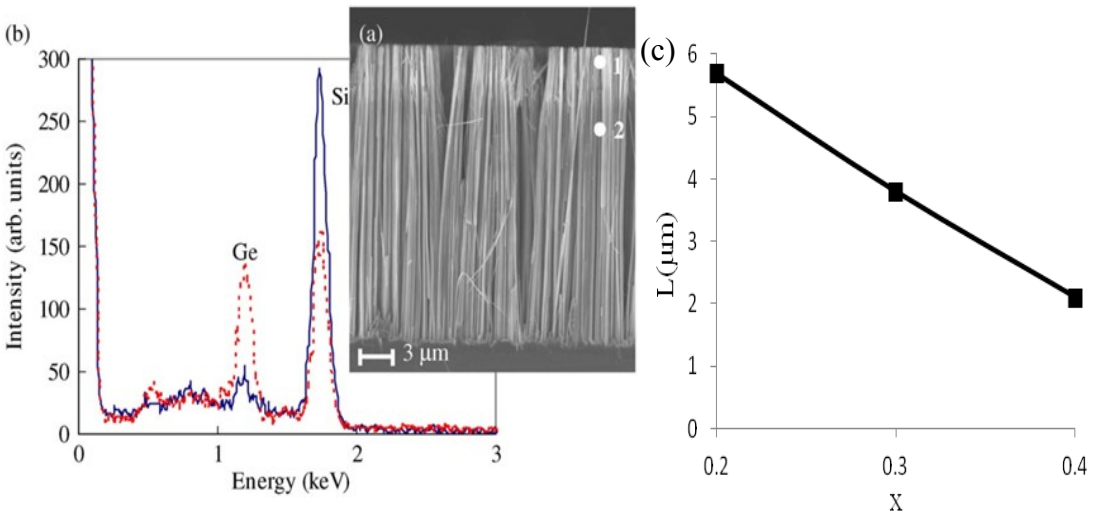


Figure 4.8. (a): SEM cross-section of $Si_{0.8}Ge_{0.2}$ NWAs. (b): EDX spectrum of $Si_{0.8}Ge_{0.2}$ NWAs taken from (a). The red line is taken from '1', and the blue line is taken from '2'. (c): The length of NWAs for an etch time of 15 min as a function of Ge fraction etched with the same chemical recipe.

4.3: Si bulk and its nano-structures with SOD and sputter coated Cu contacts

As given in Fig 1.8, the contact between Cu and semiconductor in a TEG introduces thermal and electrical contact resistances, as analyzed in Section 1.4. The TEG's output power can be improved by lowering the electrical contact resistance. The electrical contact resistance, which has already been analyzed in Section 3.2.2, is a function of Si's doping density which also determines the electrical resistance of Si, the ideality factor and the Schottky barrier height between Si and Cu.

Si's doping density is increased by SOD. The ideality factor and Schottky barrier height can be reduced by sputter coated Cu contacts on the Si's surface which improves the contact quality between Cu and Si.

4.3.1: Si bulk and its nano-structures with SOD

As given in Section 4.1.2, surface depletion/enhancement in Si nanowires can have a large influence on their electrical conductivity as the depletion width, W can be of the same order of magnitude as the diameter of the nanowires, which is given in Fig. 4.5. SOD reduces the width of the depletion region of the Si nanowires, so that the conductive area of the Si nanowires becomes bigger (Simpkins, Mastro & Eddy Jr et al., 2008). The electrical resistivity of Si NWAs and Si-Cu contact resistance are decreased by SOD, reducing electrical losses. The influence of the SOD on the output power of the TEG will be discussed in Chapter 5. Here we discuss the SOD process which is used in our experiment and the reason why NWAs etching is followed by SOD.

The process of SOD and dopants distribution profile after thermal diffusion has been introduced in Section 3.3. In our research, the p- and n-type SOD solutions used are boron and phosphorous, respectively, from Futurrex (Futurrex.com, 2014). The dopants source (Boron) of p-type Si is dropped on the Si surface and spun at 2500 rpm for 40 s, followed by a soft bake at 200 ℃ for 25 min to remove the solvents. The process is repeated at the other side of the Si – the Si NWA. The thermal diffusion is carried out in a tube furnace in Ar at a temperature of 900 ℃ for different durations. For the n-type Si, the same process is applied except for the thermal diffusion step which is carried out in a RTP furnace with N_2 flow at $\sim$1000 ℃ for 1 min. SOD has been applied several times on one n-type Si in order to get maximum doping density. Finally, the $SiO_2$is removed by buffered HF.

As explained in section 2.4 and 4.1.2, for good quality NWAs the doping concentration of the bulk should not be too high otherwise porous Si NWAs will result due to the large density of Ag NPs. Therefore, the SOD process cannot be applied before the NWAs fabrication else NWAs as in Fig. 4.3 will be obtained. The maximum doping concentration of the Si bulk surface without SOD used in our research is $\sim 10^{18}\mathrm{cm}^{-3}$ allowing MACE to be adapted for high quality Si NWs. SOD is then carried

out after the NWs have been etched.

4.3.2: Si bulk with sputter coated Cu contacts

The Cu-Si electrical contact resistance, which has been analyzed in Section 3.2.2, is a function of doping density (N_A and N_D), barrier height ($\emptyset_B$) and ideality factor (n). In this section, we will analyze the influence of SOD on barrier height and ideality factor.

The starting Si wafers used in our research are n-type Si ($1-10\ \Omega\cdot\text{cm}$), n-type Si ($0.01-0.02\ \Omega\cdot\text{cm}$), p-type Si ($1-5\ \Omega\cdot\text{cm}$) and p-type Si (0.01-0.02 $\Omega\cdot\text{cm}$). Firstly, the set-up given in Fig. 2.9 is used to measure the Schottky barrier height and ideality factor of these 4 samples and the measurement results are given in Table 4.1.

	n (1-10 Ω· cm)	p (1-5 Ω· cm)	n (0.01-0.02 Ω· cm)	p (0.01-0.02 Ω· cm)
$\emptyset_B$(eV)	0.64	0.52	0.62	0.54
n_0	18.46	21.19	21.62	15.44

Table 4.1: Ideality factor (n_0) and Schottky barrier height ($\emptyset_B$) for Cu-Si contacts at room temperature (kT=0.0258eV). The contact area is 4 cm^2, the Richardson's constant for n-type Si is 112$\frac{A}{cm^2\cdot K^2}$, and the Richardson's constant for p-type Si is 32$\frac{A}{cm^2\cdot K^2}$ (Li & Thurder, 1977).

According to the results given in Table 4.1, firstly, the Schottky barrier height of n-type Si is much larger than the one of p-type Si. Secondly, the Schottky barrier height is independent of the doping density, and this is consistent with (Smith & Rhoderick, 1971). Thirdly, the ideality factor is much bigger than 1. The large ideality factor can be associated to the poor interface between Cu and Si in the pressure contact used in this measurement set-up, and the real Cu-Si electrical contact resistance is much bigger than the ideal Cu-Si electrical contact resistance given in Section 3.2.2 due to the large ideality factor.

The poor Cu-Si contact and the occurrence of an oxide on the Cu blocks, identified by the high ideality factor and Schottky barrier height, cause a large Cu-Si electrical contact resistance which can be decreased by improving the Cu-Si contact quality. In order to improve the contact quality between Cu and Si, 300 nm Cu is sputter coated onto the two surfaces. The I-V characteristics are measured using the set-up given in Fig. 2.9. A typical measurement is shown in Fig. 4.9.

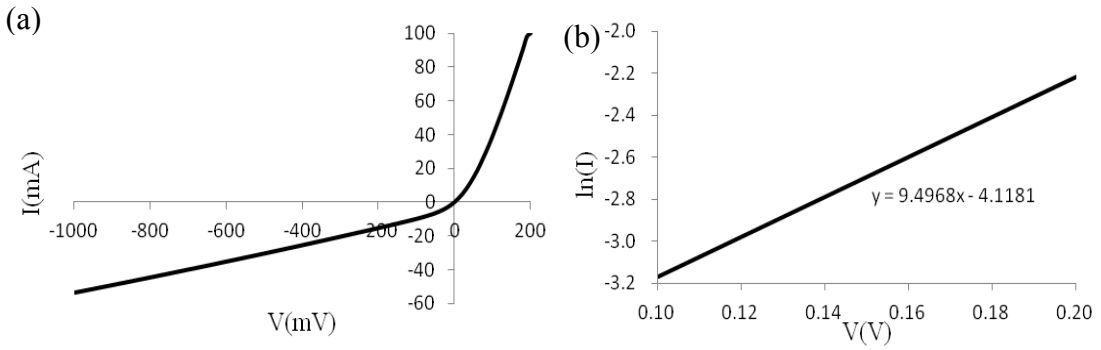


Figure 4.9 (a): I-V characteristic of n-type Si bulk (1-10 Ω · cm) with sputtered Cu contacts. (b): The natural logarithm of the current as a function of voltage.

The ideality factor (n) and Schottky barrier height ($\emptyset_B$) are extracted and given in Table 4.2. The contact area is 4 cm^2, the Richardson's constant for n-type silicon is $112\frac{A}{cm^2 \cdot K^2}$, and for p-type silicon is $32\frac{A}{cm^2 \cdot K^2}$(Li & Thurder, 1977).

	n (1-10 Ω· cm)	p (1-10 Ω· cm)
$\emptyset_B$(eV)	0.56	0.54
n_0	4	4.82

Table 4.2: n and $\emptyset_B$ are obtained at room temperature (kT=0.0258eV).

According to the results given in Table 4.2, ideality factors (n) have decreased a lot in contrast to the ideality factors in Table 4.1. The n-type Si Schottky barrier height also decreased from 0.63eV to 0.56eV, while the p-type Si Schottky barrier height did not change. The contact between Cu and heavily doped n- and p-type (0.01-0.02 Ω · cm) Si bulk samples with sputtered Cu contacts is an Ohmic contact whose I-V figure is linear, so Schottky barrier height and ideality factor cannot be gotten from its I-V figure.

According to the data in Table 4.1 and 4.2, we can obtain following conclusions: Sputter coating reduces the Cu-Si electrical contact resistance. Furthermore, the decreased magnitude of the n-type Si-Cu electrical contact resistance is much larger than for the p-type Si-Cu contact, because the Schottky barrier height of p-type Si does not change after sputter coating. These two conclusions will be demonstrated in the following.

A further improvement can be achieved by applying SOD to both surfaces of the p- and n- type Si substrates. SOD diffusion is done in the tube furnace at 900 ℃ under argon for 2 hours. Although the Schottky barrier height is independent of doping density, and thus SOD cannot change the Schottky barrier height, the depletion width induced by the Schottky barrier becomes sufficiently small for tunneling to occur. The I-V characteristics of these Si substrates with SOD on both surfaces but without sputtered Cu contacts are given in Fig. 4.10.

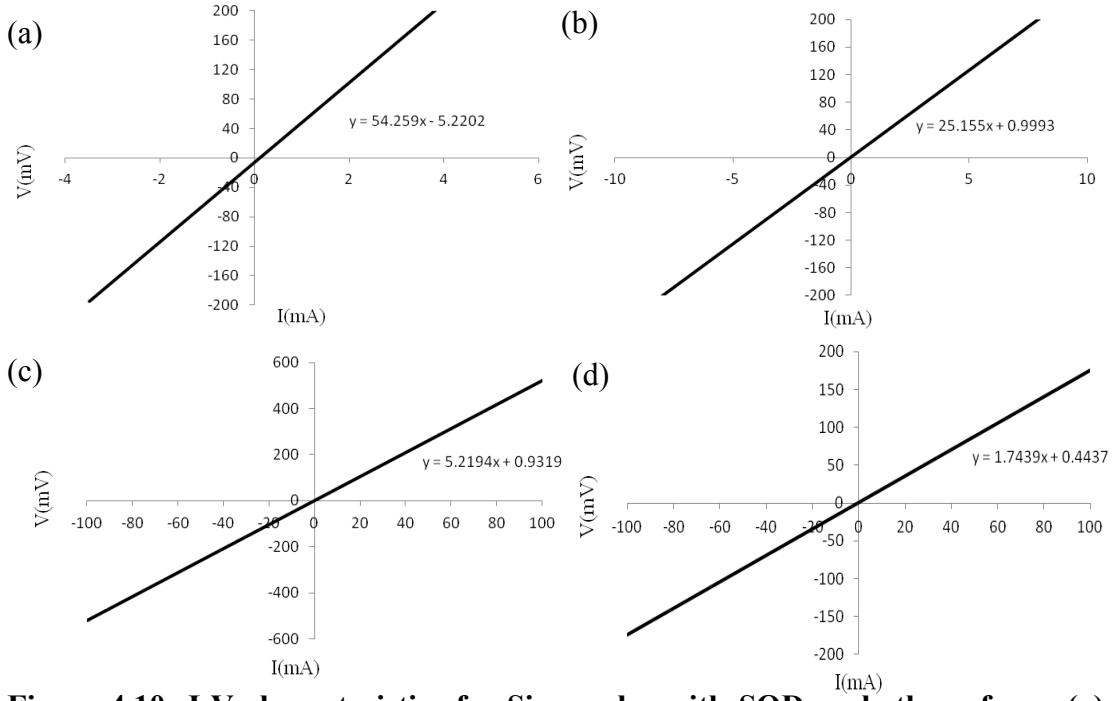


Figure 4.10: I-V characteristics for Si samples with SOD on both surfaces. (a): n-type Si bulk (1-10 Ω· cm); (b): n-type Si bulk (0.01-0.02 Ω· cm); (c): p-type Si bulk (1-5 Ω· cm); (d): p-type Si bulk (0.01-0.02 Ω· cm).

As shown in Fig. 4.10, all contacts have Ohmic performance within the measurement range which is limited by the parameter analyzer. The slope of the characteristics gives the contact resistance. Their values are summarized in Table 4.3.

	n (1-10 Ω·cm)	n (0.01-0.02 Ω·cm)	p (1-10 Ω·cm)	p (0.01-0.02 Ω·cm)
Contact Resistance(Ω)	54.25	25.15	5.219	1.743

Table 4.3: Summary of the contact resistance.

According to the data in Table 4.3, the n-type Si-Cu electrical contact resistance is much bigger than the p-type Si-Cu contact, because the Schottky barrier height of n-type Si is much bigger than of p-type Si (See Table 4.1).

The same measurements were done using sputter coated Cu contacts on SOD treated Si. I-V characteristics are given in Fig. 4.11 and the extracted contact resistance is given in Table 4.4.

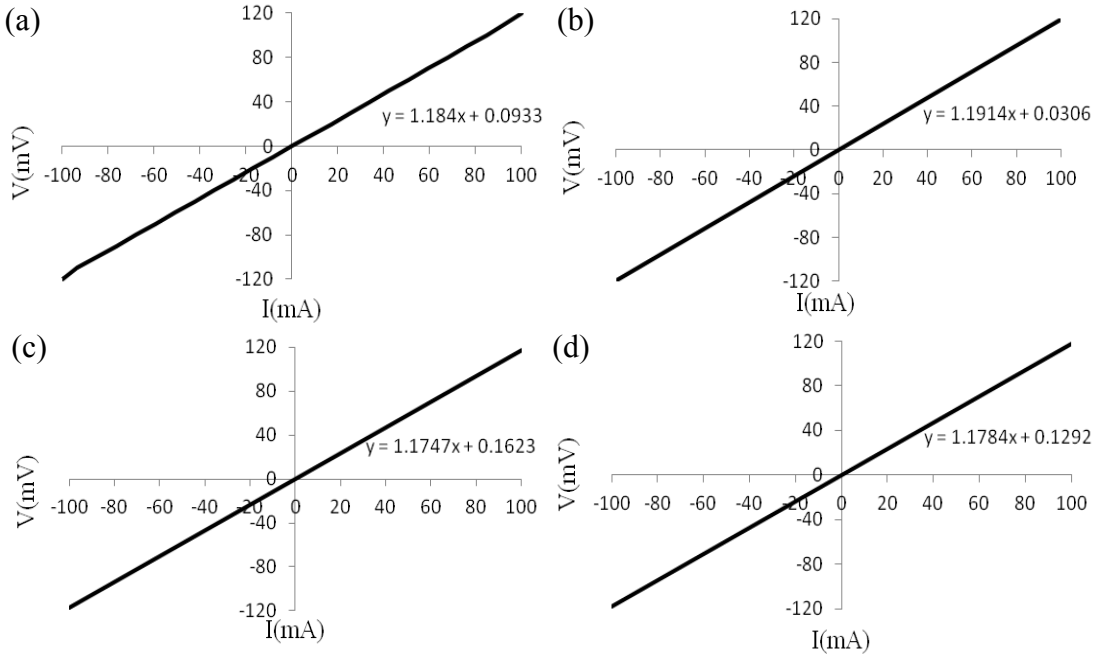


Figure 4.11: I-V characteristics, SOD and sputter coating are done on Si two surfaces. (a): n-type Si bulk(1-10 Ω· cm); (b): n-type Si bulk (0.01-0.02 Ω· cm); (c): p-type Si bulk (1-5 Ω· cm); (d): p -type Si bulk (0.01-0.02 Ω· cm).

All I-V characteristics are Ohmic within the measurement range which is limited by the parameter analyzer, as shown in Fig. 4.15. The slope of the lines is the contact resistance. The values are summarized in Table 4.4:

	n (1-10 Ω·cm)	n (0.01-0.02 Ω·cm)	p (1-10 Ω·cm)	p (0.01-0.02 Ω·cm)
Contact Resistance(Ω)	1.184	1.191	1.174	1.178

Table 4.4: Summary of contact resistance.

If we compare Table 4.3 and 4.4, the contact resistances of both n- and p-type Si are smaller when Cu is sputter coated onto Si. For n-type Si, the large decreased contact resistance is caused by the decrease of ϕ_B and n. The small decrease of contact resistance for p-type Si is caused by the decrease of n. In Table 4.4, the contact resistance is almost the same for the 4 different samples.

It is clear that the electrical contact resistance can be strongly reduced for both n- and p-type Si if SOD and Cu sputtered contacts are used. Unfortunately the temperature drop becomes large between sputtered Cu and Cu block, reducing the open circuit output voltage of the material to nearly zero.

4.4: Conclusions

The thermoelectric materials used in our research are Si and Si/$Si_{1-x}Ge_x$, as well as their NWAs. In order to obtain strong crystalline NWs the MACE recipe was optimized for doping density and type. Since high doping restricts the application of MACE, SOD on the NWAs has been used to increase their doping concentration. In

this chapter we have evaluated the influence of SOD on the contact resistance between Cu and Si. The use of sputter coated Cu contacts decreases the Si-Cu contact resistance for both p- and n-type Si. Unfortunately, the large temperature drop that occurs at the Cu-Cu contact within the measurement set-up restricts its application.

Chapter 5: Output power of Si and Si/SiGe nanowire arrays

As described in the previous chapters, a way to characterize the performance of a material is to measure its output power as a function of temperature and load resistance. In this chapter we will present the output power measurement on lightly doped $Si_{1-x}Ge_x$ based nanowire array structures, the performance of lightly and heavily doped Si nanowire arrays and the use of spin-on-doping to optimize this performance. The techniques used are those as introduced in the previous chapters. In this Chapter, only the $Si_{0.8}Ge_{0.2}$, $Si_{0.7}Ge_{0.3}$ and $Si_{0.6}Ge_{0.4}$ NWAs indicated in Table 5.3 are measured with Ag foil, and all other samples are measured without Ag foil.

5.1: Influences of SiGe alloy and nanostructure

As the theoretical model of the TEG's output power shows, given by eq. (1.26) and Fig. 1.6, the output power is affected by temperature difference ΔT that can be maintained across the structure and the power factor $\alpha^2 \times \sigma_{TEG}$ with the electrical conductivity σ_{TEG} and the Seebeck coefficient α. The application of a $Si_{1-x}Ge_x$ alloy and nanostructure are two methods to increase the temperature difference ΔT due to their much lower thermal conductivity. The material used in this section is grown by LP-CVD which is kindly supplied by Dr. M. Myronov of the University of Warwick (Myronov, Liu & Dobbie et al., 2011).

5.1.1: Si/$Si_{0.8}Ge_{0.2}$ bulk and nanostructure

In this section, we investigate the influence of the introduction of a $Si_{0.8}Ge_{0.2}$ layer. We will compare the performance of Si bulk, Si/$Si_{0.8}Ge_{0.2}$ bulk heterojunction, Si/$Si_{0.8}Ge_{0.2}$ bulk + Si NWA and $Si_{0.8}Ge_{0.2}$ NWA on Si bulk. The NWAs are fabricated via MACE using the recipes described in Chapter 4. We measure the output power of the TEGs for small external temperature differences of maximum 6 K around room temperature as a function of load resistance. In order to allow comparison between the different structures, resistive heating is kept constant at 6.25W such that the heat flux input is kept constant for all measurements. We compare the measured output power with the theoretical output power model given in Section 1.4. The measurements show that, even when the length of the NWAs and the thickness of the SiGe layer are small compared to the remaining bulk, the performance of the TEG is improved.

The Si bulk used in this section is p-type with resistivity $\rho \approx 5.6\ \Omega\cdot$cm, determined by 4 point probe measurement. Si bulk with small doping densities was chosen to simplify the NWAs fabrication processes. This doping density is not optimal thermoelectric performance. For optimization of the output power, the doping

concentration needs to be increased to increase the available carrier density to a level of 10^{19}~10^{20} cm^{-3} which has been demonstrated by the carrier density corresponds to peak ZT in Chapter 3. Increasing the doping density to optimize the performance of Si NWAs structure will be introduced in Section 5.2 and 5.3. Si NWAs used in this section are fabricated via MACE whose recipe is given in the 1st part of Section 4.1.2. The $Si/Si_{0.8}Ge_{0.2}$ bulk used in this section is described in Section 4.2.1, and its NWAs fabrication is described in Section 4.2.2.

Different NWAs-based samples are prepared, all with a NWAs length of approximately 20 μm and a diameter distribution of 50 nm < d < 250 nm (Krali & Durrani, 2013). Five samples are used in the TEG comparison: Si bulk (500 μm thick); $Si/Si_{0.8}Ge_{0.2}$ bulk (~510 μm); a 19-μm Si NWA on 480-μm bulk Si (S1); and a 19-μm SiGe/Si NWA on 490-μm bulk Si (S2). These NWAs are composed of a constant composition $Si_{0.8}Ge_{0.2}$ layer, followed by a graded SiGe layer and a Si layer. The third NWA-based sample (S3) uses the same material as S2; however, a 20-μm Si NWAs is etched at the back of the substrate, and the SiGe layer has been left unetched. The thickness of the remaining Si substrate is 480μm.

As given in Fig. 2.11(a), two small Cu blocks are used as contacts to the sample with a cross sectional area of 1.5 cm × 1.5 cm. For the NWAs side, the effective transport cross sectional area reduces by approximately 50%, as derived from SEM. The pressure applied by the screw is $89N/cm^2$, and the heating power P_{heat} supplied by heater is the same at 6.25W for all 5 measurements.

I-V, temperature difference ΔT, open circuit voltage ΔV, and output power P_{out} as a function of load resistance R_L are measured without the use of Ag foil for all 5 samples because when using Ag foil under pressure on the NWAs, the removal of the sample from the set-up also removes the NWAs from the Si substrates as they remain stuck to the Ag foil, so the NWAs samples cannot be re-used.

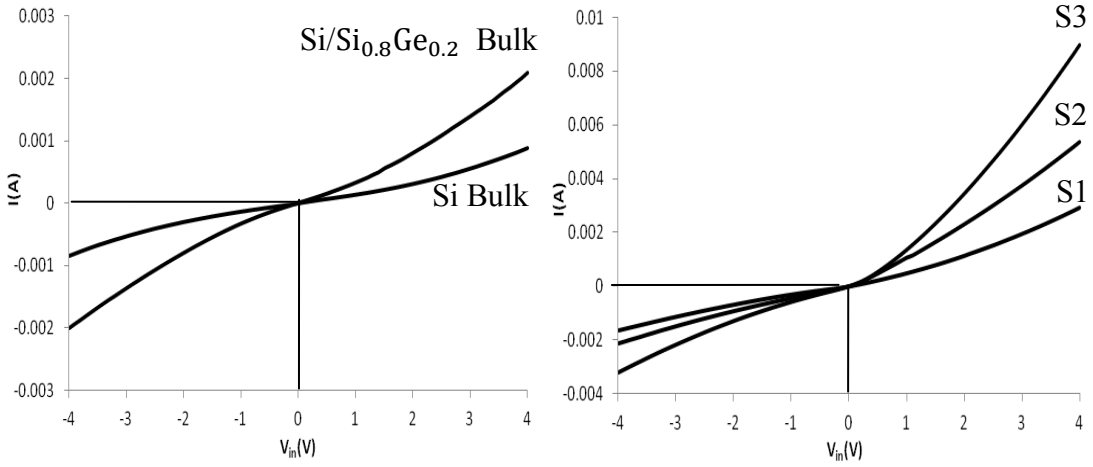


Figure 5.1: I-V figure of all samples using a Cu press contact.

The I-V measurements, given in Fig. 5.1, were done using the set-up and parameter

analyzer as given in Fig. 2.9. These measurements show that the Cu–sample pressure contacts have a non-linear character due to the work function difference between sample and Cu and the nano air gaps at the junction.

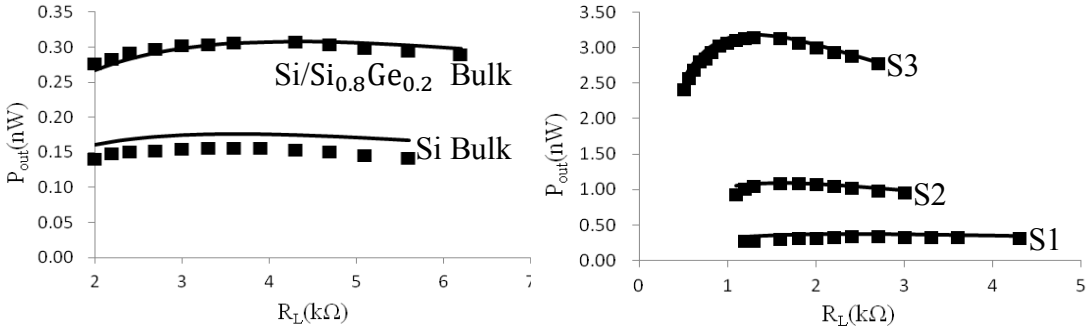


Figure 5.2: Output power of all samples. Solid lines are the theoretical calculations, and squares are the measured values. Output power is measured under the same heat input.

The measured values in Fig. 5.2 are summarized in Table 5.1.

Samples	ΔT(K)	P_{out}^{max}(nW)	R_{TEG}(kΩ)	ΔV(mV)
Si Bulk	2.7	0.16	3.6	1.6
$Si/Si_{0.8}Ge_{0.2}$ Bulk	3.3	0.31	4.3	2.3
S1	3.4	0.34	2.4	1.9
S2	4.9	1.08	1.8	2.6
S3	5.7	3.14	1.3	4.1

Table 5.1: Summary of measured values in Figure 5.2.

As given in Table5.1, ΔT is the measured temperature difference under the same heat input. P_{out}^{max} is the maximum output power when R_L and R_{TEG} are matched. R_{TEG} is the resistance of the TEG determined from the maximum output power point. It is representative for the electrical conductivity σ_{TEG} that has to be used in the theoretical output power model to fit the measurements. ΔV is the measured open circuit voltage.

The solid line is the theoretical output power as a function of load resistance. Seebeck coefficient and temperature difference used in the theoretical model are obtained from ΔT and ΔV given in Table 5.1. The electrical conductivity used in the theoretical model are extracted from the sample's dimensions and R_{TEG} given in Table 5.1. According to the solid lines and square marks in Fig. 5.2, the measured values and theoretical values are consistent.

As given in Table 5.1, ΔT increases for NWA- and $Si_{0.8}Ge_{0.2}$-based TEGs. $P_{out}$is generated for very small ΔT in the same range as those in (Li, Buddharaju & Singh et al., 2011) and (Wang, Jia & Huang et al., 2005). Improvements in P_{out}^{max} of factors of ~2 and ~20 are obtained for S1 and S3, respectively, compared to Si bulk. The internal resistance R_{TEG} is found to be of the same order of magnitude as R_{IV} which

is obtained from Fig. 5.1. Furthermore, R_{TEG} is approximately three orders of magnitude larger than the electrical resistance of the samples, because R_{TEG} is composed of the electrical resistance of the sample and the contact electrical resistance between Cu and samples. This demonstrates that the contact electrical resistance between Cu and samples is much larger than the electrical resistance of the samples.

In order to characterize the influences of ΔT and R_{TEG} on output power improvement, given in Table 5.1, we will first analyze the temperature drop across the samples. The measured Seebeck coefficient can be obtained via ΔV vs ΔT measurement, given in Table 5.1. These values appear low for lightly doped samples in contrast to the theoretical Seebeck coefficient has been given in Section 3.1.1, because of the temperature drop across the sample-Cu interface. In order to find the intrinsic Seebeck coefficient, the temperature drop at the contact needs to be removed. The temperature drop across the sample ΔT_s can be obtained via eq. (2.10) in which ΔT_{Cu} is ignored due to its high thermal conductivity.

Samples	$\Delta T(K)$	$\Delta V(mV)$	$\alpha_{measurement}$ (mV/K)	$\alpha_{Calculate}(mV/K)$	$\Delta T_s(K)$
Si Bulk	2.7	1.6	0.59	1.05	1.5
Si/$Si_{0.8}Ge_{0.2}$ Bulk	3.3	2.3	0.70	1.07	2.2
S1	3.4	1.9	0.56	1.05	1.8
S2	4.9	2.6	0.53	1.07	2.4
S3	5.7	4.1	0.72	1.07	3.8

Table 5.2: Seebeck coefficient and temperature drops across samples.

ΔT_s, given in Table 5.2, reflects the temperature drop across the samples only, and is the real temperature difference which generates the open circuit voltage ΔV by Seebeck effect. NWAs- and $Si_{0.8}Ge_{0.2}$-based samples all have higher ΔT_s in contrast to Si bulk due to the smaller thermal conductivity of the NWAs and $Si_{0.8}Ge_{0.2}$ bulk layer. According to Fourier's law given in eq. (3.53), the thermal conductivity of the $Si_{0.8}Ge_{0.2}$ bulk layer can be estimated as $\lambda_{Si_{0.8}Ge_{0.2}\,bulk} \approx 3.83\ W/(m \cdot K)$, which is consistent with the theoretical value given in Fig. 3.11, via eq. (5.1).

$$\lambda_{Si\,bulk} \times A \times \frac{\Delta T_{Si\,bulk}}{L_{Si\,bulk}} = \lambda_{Si_{0.8}Ge_{0.2}\,bulk} \times A \times \frac{\Delta T_{Si_{0.8}Ge_{0.2}\,bulk}}{L_{Si_{0.8}Ge_{0.2}\,bulk}} \qquad (5.1)$$

With $\lambda_{Si\,bulk}$ the thermal conductivity of Si bulk ($149\ W/(m \cdot K)$), A the sample's area, $\Delta T_{Si\,bulk}$ the temperature drop across Si bulk (1.5 K), $L_{Si\,bulk}$ the thickness of the Si bulk (500μm), $\lambda_{Si_{0.8}Ge_{0.2}\,bulk}$ the thermal conductivity of the $Si_{0.8}Ge_{0.2}$ bulk layer, $\Delta T_{Si_{0.8}Ge_{0.2}\,bulk}$ the temperature drop across the $Si_{0.8}Ge_{0.2}$ bulk layer (0.7K), and $L_{Si_{0.8}Ge_{0.2}\,bulk}$ the thickness of the $Si_{0.8}Ge_{0.2}$ bulk layer (6μm).

The thermal conductivity of Si NWAs can be estimated as $\lambda_{\text{Si NWAs}} \approx 10.77\ \text{W}/(\text{m}\cdot\text{K})$, which is consistent with the value given in (Hochbaum, Chen & Delgado et al., 2008), via eq. (5.2):

$$\lambda_{\text{Si NWAs}} = \lambda_{\text{Si Bulk}} \times \frac{\Delta T_{\text{Si bulk}}}{\Delta T_{\text{Si NWAs}}} \times \frac{L_{\text{Si NWAs}}}{L_{\text{Si Bulk}}} \times \frac{A_{\text{Si Bulk}}}{A_{\text{Si NWAs}}} \tag{5.2}$$

With $\lambda_{\text{Si bulk}}$ the thermal conductivity of Si bulk ($149\ \text{W}/(\text{m}\cdot\text{K})$), the effective transport cross sectional area of NWAs side reduces by approximately 50% making $\frac{A_{\text{Si Bulk}}}{A_{\text{Si NWAs}}} = 2$, $\frac{L_{\text{Si NWAs}}}{L_{\text{Si Bulk}}}$ the ratio of Si NWAs thickness and bulk thickness ($20\mu\text{m}/480\mu\text{m}$) and $\frac{\Delta T_{\text{Si bulk}}}{\Delta T_{\text{Si NWAs}}}$ the ratio of temperature drop across Si bulk and Si NWAs (1.44K/1.66K).

In addition, the ΔT_s magnitudes of S1, S2 and S3 are also consistent with their output power magnitudes. ΔT_s of $Si/Si_{0.8}Ge_{0.2}$ bulk is higher than that of S1, but its output power is slightly smaller than that of S1. This is due to the second factor: R_{TEG} which also affects TEG's output power. The influence of R_{TEG} is analyzed via the normalized output power.

The squares given in Fig. 5.3 are the measured normalized output power, and the solid line is the theoretical normalized output power. We can analyze the output power improvement affected by R_{TEG} only via the normalized output power. As the results given in Fig. 5.3 show, the normalized output power of S1, S2 and S3 is increased by R_{TEG} in contrast to Si bulk. In addition, the normalized output power of $Si/Si_{0.8}Ge_{0.2}$ bulk is decreased by R_{TEG} in contrast to Si bulk. These results are very consistent with the magnitude of R_{TEG} given in Table 5.1: $Si/Si_{0.8}Ge_{0.2}$ bulk has maximum R_{TEG} and S3 has minimum R_{TEG}.

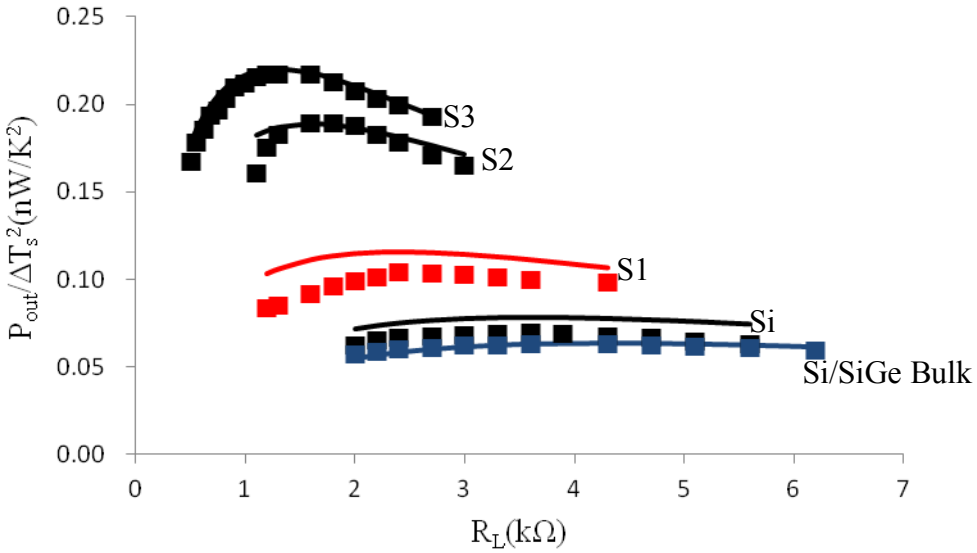


Figure 5.3: Output power P_{out} normalized by ΔT_s^2 as a function of load resistance R_L.

From above analysis, the value of P_{out}^{max} is limited by both the temperature drop across the samples and TEG's electrical resistance. The values of ΔT_s and the estimation of the thermal conductivities of Si NWAs and $Si_{0.8}Ge_{0.2}$ bulk confirm that the NWAs/ $Si_{0.8}Ge_{0.2}$ -based thermoelectric materials have a lower thermal conductivity than bulk even for very thin NWAs/$Si_{0.8}Ge_{0.2}$ layers, improving P_{out}. $P_{out}/\Delta T_s^2$ shows an additional improvement due to the lower electrical resistance of the NWAs-based devices. This is due to a poorer pressure contact on bulk than NWAs because, under pressure, the tops of the NWAs bend and some break but also adhere strongly to the Cu. The lower thermal conductivity, together with the reduced electrical resistance in the NWAs-based samples, leads to improved output power performance.

If these five samples are characterized from the aspects of ZT, they all have quite similar Seebeck coefficient ($1.05mV/K \sim 1.07mV/K$) and electrical conductivity σ due to the same doping density. Their only difference is the much lower thermal conductivity by introducing NWAs and $Si_{0.8}Ge_{0.2}$ layers, so NWAs- and $Si_{0.8}Ge_{0.2}$-based samples have higher ZT in contrast to Si bulk, and this is consistent with their higher output power.

5.1.2: $Si/Si_{1-x}Ge_x$ (x=0.2, 0.3 and 0.4) bulk, nanostructures and pn junctions

In the previous section only a single leg TEG was analyzed using only$Si_{0.8}Ge_{0.2}$. In this section, the output power of a discrete assembly of n-type Si and p-type $Si/Si_{1-x}Ge_x$ with 3 different Ge fractions x=0.2, 0.3 and 0.4, samples are measured as a function of load resistance. The influences of the Ge fraction and NWAs on the TEG's performance are evaluated in measurements around room temperature.

The structure of the p-type Si/$Si_{1-x}Ge_x$ (x=0.2, 0.3 and 0.4) bulk samples were given in Fig. 3.16, and their NWAs were fabricated by one-step MACE which is given in Section 4.2.2.

The schematic drawing of the measurement set-up is given in Fig. 2.12. Two small Cu blocks are used as independent bottom contacts to each sample which have each a cross sectional area of 1.5 cm ×1 cm. For the NWAs side, the effective transport cross sectional area reduces by approximately 50%. In order to decrease the electrical and thermal resistance between the Cu blocks and the TEG the samples are clamped with a pressure of $90N/cm^2$. For all measurements, the power in the heater is the same at 6.25W, thus keeping the supplied heat flux the same.

Fig. 5.4 (a) gives the measurement of the Seebeck coefficient for an n and p-type Si NWA with nanowire length of respectively 15 μm and 16μm. The extracted Seebeck coefficient is given in Table 5.3. These measurements were done without Ag foil and without pressure which results in 80% temperature drop across the interfaces between sample and Cu (Li, Xu & Durrani et al., 2011), (Xu, Li & Myronov et al., 2013). As a consequence, the extracted values for Seebeck coefficient are too low as the temperature drop across the sample ΔT_s is ~20% of the measured one. Taking this into account gives more realistic values of Seebeck coefficient for a substrate resistivity of ρ_{Si} = 5.6 Ω · cm from which these NWAs are made. The estimated Seebeck coefficient $\alpha_{Estimate}$ is given in Table 5.3, which is consistent with the theoretical Seebeck coefficient given in Section 3.1.1. The choice to measure Seebeck coefficient without pressure and Ag foil, is imposed by the need to re-use the same samples in pn junction configurations. Due to the combination of Ag foil and pressure on the NWAs, removal of the sample from the set-up also removes the NWAs from the Si substrate as they remain stuck to the Ag foil. The measurement results of the pn junction configurations can also be found in Fig. 5.4 (a) and Table 5.3. We expect that the total Seebeck coefficient α_{tot} for the pn junction is the sum of that of the individual n- and p-type samples. We find $\alpha_{tot}^{Estimate}$ = 2.35 mV/K, while the sum of $|\alpha_n^{Estimate}|$ and $|\alpha_p^{Estimate}|$ is 2.15mV/K, which is reasonably close to the expected value.

Similar Seebeck measurements have been carried out for individual $Si_{1-x}Ge_x$ NWAs samples for the different Ge fractions. In this case, samples were not re-used and therefore both Ag foil and a pressure of $167N/cm^2$ were applied, and the measurement set-up is given in Fig. 2.11 (a). The results are given in Fig. 5.4 (b) and Table 5.3. The Seebeck coefficients of the $Si_{1-x}Ge_x$ NWAs samples have a similar magnitude and are also similar to that of Si NWAs samples. This is not surprising as Seebeck coefficient theoretical model given in Section 3.1.1 shows that Seebeck coefficient does not vary as a function of Ge fraction and moreover, the length of the

NWAs is much smaller than the thickness of the remaining bulk.

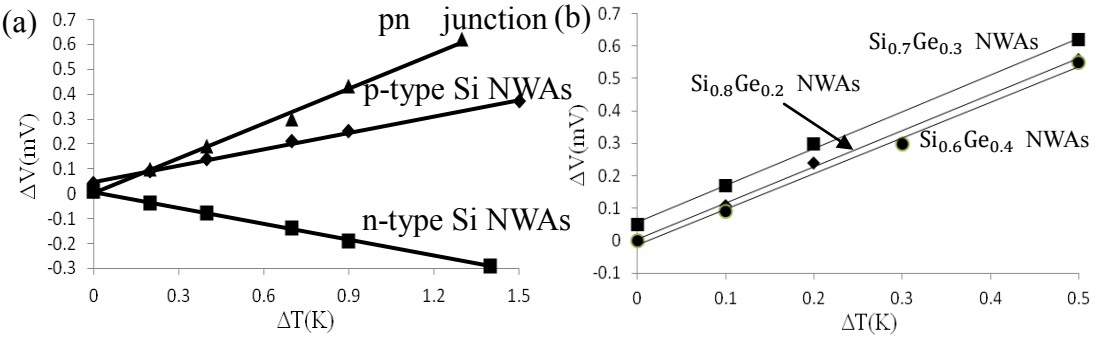


Figure 5.4: Seebeck coefficient measurement. (a): For the individual n- and p-type Si NWAs samples and the pn junction made with the same material. No Ag foil is used and no pressure is applied. (b) For all three SiGe samples containing SiGe NWAs. Ag foil is used to minimize the temperature drop across the interface and a pressure of $167\mathrm{N/cm^2}$ is applied.

The measurement values in Fig. 5.5 are summarized in Table 5.3.

Samples	$L_{NWAs}(\mu m)$	$\alpha(mV/K)$	$\alpha_{real}(mV/K)$
n-type Si NWAs	15	-0.21	-1.05
p-type Si NWAs	16	0.22	1.10
pn junction	16/15	0.47	2.35
$Si_{0.8}Ge_{0.2}$ NWAs	14	1.12	–
$Si_{0.7}Ge_{0.3}$ NWAs	12	1.14	–
$Si_{0.6}Ge_{0.4}$ NWAs	18	1.10	–

Table 5.3: Length of the NWAs, L_{NWAs}, the measured Seebeck coefficient, α for the different Ge fractions and the real Seebeck coefficient, α_{real} that takes into account the temperature drop at the interfaces.

The measurements of the output power P_{out} were done as a function of load resistance R_L using the set-up given in Fig. 2.12. For the n-type leg, Si bulk or NWAs, as appropriate, was used in all cases. For the p-type leg, the p-type Si was replaced by the $Si_{1-x}Ge_x$ samples. The cross sectional area of all samples was approximately 1.5 cm $\times$1 cm. The lengths of the NWAs were kept at approximately the same value for all samples. The samples were clamped under a pressure of around $90\mathrm{N/cm^2}$ and are applied by two screws in order to create a more homogeneous pressure on the system in all measurements, but no Ag foil was used in order to allow repeated measurements. This implies that the measured output power will suffer from a power reduction due to the thermal and electrical contact resistances at the Cu–samples interfaces.

The results of the measurements of P_{out} as a function of R_L are given in Fig. 5.5 (a) for bulk and (b) for the NWAs samples. These measurements follow the expected variation of P_{out} as a function of the load resistance. The maximum output power is reached when the load R_L is equal to the internal resistance R_{TEG} of the TEG. Internal resistance includes both the electrical contact resistances at the Cu-sample

contact interfaces as well as the resistance of the sample itself.

From Fig. 5.5(a), we see that the $Si_{1-x}Ge_x$ alloy with the Ge fraction of 40% outperforms the others, attributed mainly to a better contact resistance. It changes for the NWAs samples where the observed performance improvement of the 40% NWAs is less. We attribute this to a degradation of the SiGe layer upon NWAs etch for higher Ge concentrations or the too high strain of the SiGe NWAs due to the larger difference in length between the p and n leg in the TEG.

Table 5.4 summarizes the most important parameters extracted from these measurements. It is clear that the internal resistance of the bulk-based TEG is higher than that of the NWAs-based TEG. This is due to a poorer pressure contact on bulk than NWAs because, under pressure, the tops of the NWAs bend and some break but also adhere strongly to the Cu. The performance of the $Si_{1-x}Ge_x$ containing samples is better than Si. This is due to a higher temperature difference that is maintained in the $Si_{1-x}Ge_x$ samples. Changing a small part of the bulk into NWAs increases the output power by a factor of $\sim$10, proving experimentally the performance increase to be gained from the introduction of even a small region of NWAs. This improvement is a result of both an improved contact resistance as well as an improved temperature drop across the NWAs samples.

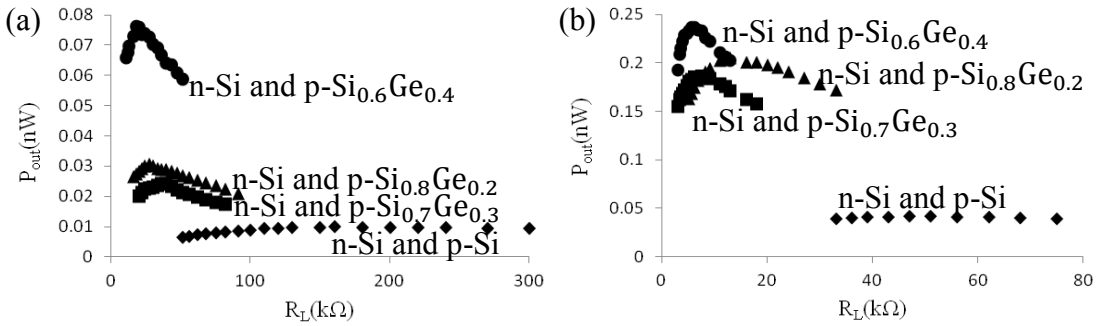


Figure 5.5: Output power P_{out} as a function of load resistance R_L for four different pn junction configurations. (a) Bulk samples. (b) NWAs samples.

The measurement values of Fig. 5.5 are summarized in Table 5.4.

Samples	P_{out}^{max} (nW)	R_{TEG}(kΩ)	ΔT(K)	ΔV(mV)	L_{NWAs}(μm)
Si Bulk	0.01	160	2.4	2.85	0
Si NWAs	0.04	51	2.6	2.98	10p/16n
$Si_{0.8}Ge_{0.2}$ Bulk	0.03	30	2.8	1.9	0
$Si_{0.8}Ge_{0.2}$ NWAs	0.2	13	3.3	3.28	23p/16n
$Si_{0.7}Ge_{0.3}$ Bulk	0.02	39	2.8	1.81	0
$Si_{0.7}Ge_{0.3}$ NWAs	0.19	7.5	3.3	2.4	25p/16n
$Si_{0.6}Ge_{0.4}$ Bulk	0.08	20	2.9	2.32	0
$Si_{0.6}Ge_{0.4}$ NWAs	0.24	6.2	3.3	2.38	31p/16n

Table 5.4: Performance parameters for the different TEGs: maximum output powerP_{out}^{max}, internal resistanceR_{TEG}, temperature differenceΔT, open circuit voltageΔV, and NWAs lengthL_{NWAs}. Samples in the first column only indicate the p-type sample of pn junctions. Subscript p and n in the last column indicate the doping type of the NWAs.

According to the measurement values given in Fig. 5.6 and Table 5.4, the characterizations of $Si_{1-x}Ge_x$-based samples have no big difference with the change of Ge fraction, and this is consistent with the theoretical models of Seebeck coefficient, electrical conductivity and thermal conductivity, which are not affected a lot by Ge fraction given in Section 3.1.1.

5.2: Influence of carrier concentration

Although the previous section clearly indicates the benefits of Si and $Si_{1-x}Ge_x$ NWAs from a viewpoint of reduction in thermal conductivity, it is obvious that output power is very small, primarily because of a too low electrical conductivity. Therefore the second approach to boost the thermoelectric performance is an increase in carrier concentration. As stated before, MACE on heavily doped material poses challenges and the recipe has to be adapted to allow for sufficiently long, good quality NWAs. In Section 4.1, we have shown the adaption of etching recipes necessary to produce good quality NWAs. In Fig. 5.6(a) the output power of a single p-type Si NWA is compared to bulk when the resistivity of the starting Si bulk is $\rho \approx 1 - 10\ \Omega$ cm. In Fig, 5.6(b) the same comparison is made but for a starting Si bulk with $\rho \approx 0.01\Omega \cdot \text{cm} - 0.02\ \Omega \cdot \text{cm}$. The pressure on the contacts is 180N/cm^2 and is applied without Ag foil. The power of the heater is kept the same at 6.25W, thus keeping the supplied heat flux the same.

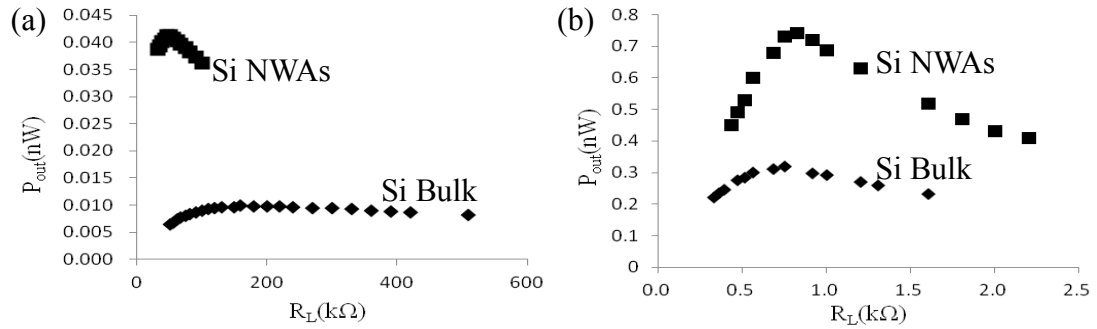


Figure 5.6: Output power P_{out} as a function of load resistance R_L for Si bulk and Si NWAs pn junction TEGs. (a): ρ ≈5.6Ω·cm ;(b): ρ ≈0.01Ω·cm.

The measurement values given in Fig. 5.6 are summarized in Table 5.5.

Samples	$\rho_{Bulk}(\Omega \cdot cm)$	P_{out}(nW)	$R_{TEG}(k\Omega)$	ΔV(mV)	ΔT(K)
Bulk	5.6	0.01	160	2.85	2.6
NWA	5.6	0.04	51	2.98	3.3
Bulk	0.01	0.32	0.75	1.02	2.4
NWA	0.01	0.74	0.82	1.62	3.7

Table 5.5: Performance parameters for different starting wafers.

As the output power given in Table 5.5 shows, an improvement of a factor of ~20 is obtained due to the large decrease of R_{TEG}. For a higher doping starting wafer, the open circuit voltage decreases due to a decrease of Seebeck coefficient with increasing carrier concentration.

The internal resistanceR_{TEG}, given in Table 5.5, of the NWAs sample is higher than that of the bulk sample for heavily doped starting wafers. This result is not consistent with the result presented in Section 5.1 where the NWAs sample has a lower internal resistance in contrast to the bulk sample. The reason might be that the tops of the NWAs bend and some break but also adhere strongly to the Cu under pressure. As the analysis in Section 4.1.2 shows, Si NWAs from heavily doped wafers are etched by a solution whose Ag concentration is very low. Then the average diameter of the Si NWs is larger than those etched with a high Ag concentration, as for the lightly doped samples. Thus, the level of elasticity of the wires changes with etch recipe and this has an impact on the way the NWs bend under pressure contact and reduce the contact resistance.

The doping density of the Si whose resistivity is $5.6\,\Omega \cdot cm$ is $\sim 10^{15} cm^{-3}$, and the doping density of the Si whose resistivity is $0.01\Omega \cdot cm$ is $\sim 10^{18} cm^{-3}$. The Si whose doping density is $\sim 10^{18} cm^{-3}$ has higher output power, and its ZT is also higher than the ZT of Si whose doping density is $\sim 10^{15} cm^{-3}$.

The main drawback of heavily doped Si is that its Seebeck coefficient is reduced, which deteriorates its ZT and TEG's output power. As the calculations in Chapter 3 show, there is an optimal doping level for high ZT. In addition, as shown in Chapter 4 increasing the doping density at the surface of the semiconductor decreases the

potential barrier between the semiconductor and contact, leading to a reduction in contact resistance. Thus, in order to increase the doping density in the Si NWA for improved power factor and reduced contact resistance spin-on-doping (SOD) has been proposed to avoid having to etch heavily doped material and thus risk decreasing the material reliability. In Chapter 4 the SOD process was fully analyzed. This process will be used in the next section to improve the performance of the Si NWAs.

5.3: TEG's output power increase via SOD

The starting Si bulk used in this section has ρ = 0.01-0.02 $\Omega \cdot$ cm for both n- and p-type. The Si NWAs are fabricated via the appropriate MACE recipe, converting ~4% of the bulk thickness (20 µm) into nanowires. The I-V characteristics and Seebeck coefficient measurements show that while SOD mainly influences the contact resistance in Si bulk-based TEGs, it influences both contact resistance and power factor ($\alpha^2\sigma$) in Si NWAs-bulk based TEGs. According to our experiments, using Si NWAs in combination with SOD increases the output power by an order of 3 under the same heating power at 9.5W due to an increased power factor, decreased thermal conductivity of the NWAs and reduced Si-Cu contact resistance.

In the theoretical model given in Section 1.4, the internal resistance of the TEG R_{TEG}, which is composed of the sample's electrical resistance and the Cu-Si electrical contact resistance, is considered as a whole.

In this section, we will separate R_{TEG} into the sample's electrical resistance and the Cu-Si electrical contact resistance. The output power of a TEG is related to the temperature difference ΔT via the thermal conductivity λ of thermoelectric material, and the power factor, $\alpha^2\sigma$ with α the Seebeck coefficient and σ the electrical conductivity of thermoelectric material. TEG uses Cu contacts, introducing a Cu-Si contact resistance. The total resistance of the TEG is thus the sum of Cu-Si contact resistance and the resistance of the sample. The output power of the TEG with matched load ($R_{TEG} = R_L$), in the presence of thermal and electrical contact resistances is given by (Rowe, 1995):

$$P_{out} = \frac{\alpha^2\sigma\Delta T^2}{2\left(\frac{2\rho_c}{\rho}+1\right)\left(1+2\frac{\lambda L_c}{\lambda_c L}\right)^2} \tag{5.3}$$

With L the thickness of the Si, L_c the thickness of the contact layer, ρ_c the electrical contact resistivity, and λ_c the thermal conductivity of the contact layer. Eq. (5.3) shows that the interface resistances, represented by ρ_c and L_c/λ_c, cause a decrease in output power of the TEG. ρ_c is due to the Schottky barrier height and the non-ideality factor of the Si-Cu contacts(Yu, 1970). The thermal contact resistance is a result of the air pockets that exist due to the non-atomically flat Cu contact block and TEG surface and due to the phonon wave vector discontinuity between metal and Si (Prasher, 2006). Thermal interface materials (TIMs) and pressure can be used to reduce L_c/λ_c. In this work, a pressure contact is used together with doping to reduce the contact parasitic. At

certain T, α is inversely proportional (Wanger,2007), while σ is proportional to doping density , determining the maximum value of $\alpha^2\sigma$. Thus doping will influence the output power by the power factor and the contact resistance simultaneously. It is necessary to do the error analysis in the following:

(1) Error analysis on Seebeck coefficient α:
If the Seebeck coefficient α is 10% overvalued and other parameters are correctly valued, the output power P_{out} will be 21% overvalued. If the Seebeck coefficient α is 10% undervalued and other parameters are correctly valued, the output power P_{out} will be 19% undervalued.

(2) Error analysis on electrical contact resistivity (ρ_c):
If the electrical contact resistance ρ_c is 10% overvalued and other parameters are correctly valued, the output power will be recorded as $\frac{\alpha^2\sigma\Delta T^2}{2\left(\frac{2.2\rho_c}{\rho}+1\right)(1+2\frac{\lambda L_c}{\lambda_c L})^2}$ whose ratio to the output power given in eq.(5.3) is $\frac{2\rho_c+\rho}{2.2\rho_c+\rho}$. Generally, ρ_c is much higher than ρ, so the ratio is equal to 91% which indicates 9% undervalued in output power if contact resistance ρ_c is 10% overvalued.

If the electrical contact resistance ρ_c is 10% undervalued and other parameters are correctly valued, the output power will be recorded as $\frac{\alpha^2\sigma\Delta T^2}{2\left(\frac{1.8\rho_c}{\rho}+1\right)(1+2\frac{\lambda L_c}{\lambda_c L})^2}$ whose ratio to the output power given in eq.(5.3) is $\frac{2\rho_c+\rho}{1.8\rho_c+\rho}$. Generally, ρ_c is much higher than ρ, so the ratio is equal to 111% which indicates 11% overvalued in output power if contact resistance ρ_c is 10% undervalued.

(3) Error analysis on thermoelectric material's electrical conductivity(σ)
If the thermoelectric material's electrical conductivity σ is 10% overvalued and other parameters are correctly valued, the output power will be recorded as $\frac{1.1\alpha^2\sigma\Delta T^2}{2(2.2\rho_c\sigma+1)(1+2\frac{\lambda L_c}{\lambda_c L})^2}$ whose ratio to the output power given in eq.(5.3) is $\frac{2.2\rho_c\sigma+1.1}{2.2\rho_c\sigma+1}$ which indicates the output power is overvalued less than 10%, particularly at the circumstance that electrical contact resistance ρ_c is much higher than thermoelectric material's electrical resistance ρ, the output power is not affected by overvalued thermoelectric material's electrical conductivity σ.

If the thermoelectric material's electrical conductivity σ is 10% undervalued and other parameters are correctly valued, the output power will be recorded as $\frac{0.9\alpha^2\sigma\Delta T^2}{2(1.8\rho_c\sigma+1)(1+2\frac{\lambda L_c}{\lambda_c L})^2}$ whose ratio to the output power given in eq.(5.3) is $\frac{1.8\rho_c\sigma+0.9}{1.8\rho_c\sigma+1}$ which indicates the output power is undervalued less than 10%, particularly at the

circumstance that electrical contact resistance ρ_c is much higher than thermoelectric material's electrical resistance ρ, the output power is not affected by overvalued thermoelectric material's electrical conductivity σ.

Six different types of samples with the same area ($2\ cm \times 2\ cm$) were prepared by MACE followed by SOD. All samples start from a bulk resistivity of (ρ= 0.01-0.02 $\Omega \cdot$ cm). 500 µm n-type Si bulk without (S1) and with SOD (S2); 20 µm n-type Si NWAs on 480 µm n-type Si bulk with SOD on both surfaces (S3); 500 µm p-type Si bulk without (S4) and with SOD (S5); and 20 µm p-type Si NWAs on 480 µm p-type Si bulk with SOD on both surfaces (S6). They are given in Fig. 5.7.

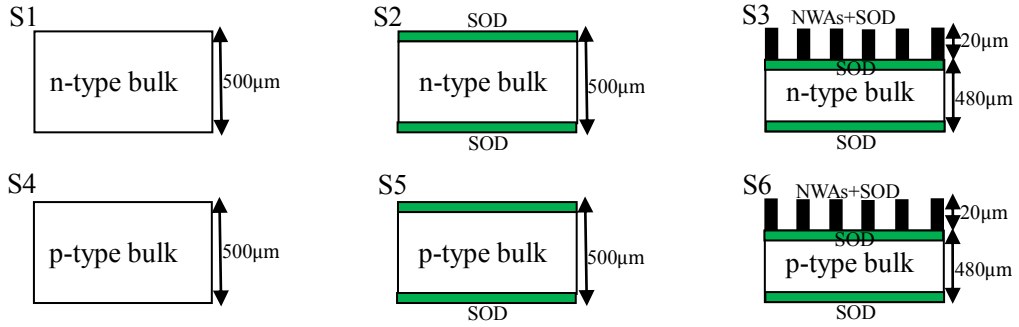


Figure 5.7: Samples used in this experiment.

The I-V characteristics of these 6 samples were measured by the set-up given in Fig. 2.9 under a pressure of $100N/cm^2$. Taking S2 and S6 as examples, their I-V measurements given in Fig. 5.8 demonstrates the occurrence of Ohmic Cu-Si contacts after SOD. The Seebeck coefficient and output power of these 6 samples are measured by the set-up given in Fig. 2.11 (b), and the pressure applied is also $100N/cm^2$. Some Seebeck and output power measurements are given in Fig.5.9.

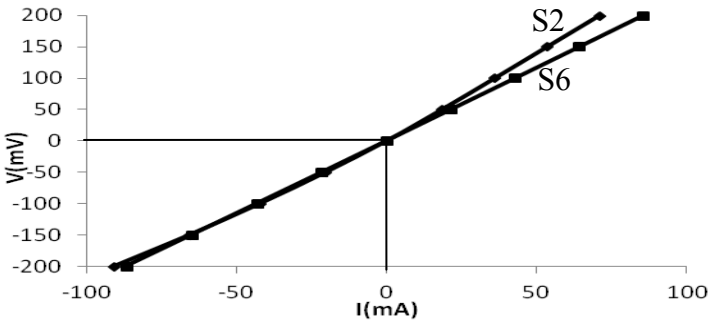


Figure 5.8: I-V characteristics of S2 and S6.

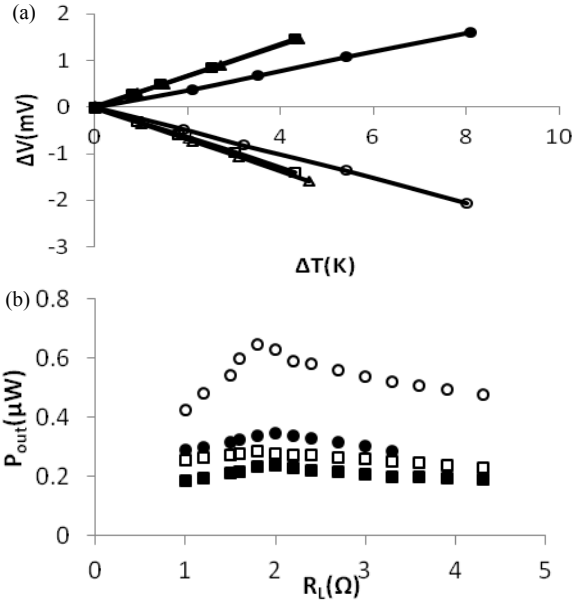


Figure 5.9 (a): Open circuit voltage versus temperature difference measurements. (b) Output power measurements as a function of load resistance for constant heat flux. Open markers: p-type sample and closed markers n-type samples. Squares and triangles are bulk samples with and without SOD, respectively. Circles are NWAs/bulk samples with SOD. The SOD applied forms an Ohmic contact (Xu & Fobelets, 2014).

The I-V characteristic, Seebeck coefficient and output power measurements of all samples are summarized in Table 5.6.

Samples	ΔV(mV)	ΔT(K)	α(mV/K)	V_{oc}(mV)	$R_L(\Omega)$	$P_{out}(\mu W)$	$R_{diff}(\Omega)$
S1	1.47	4.4	0.33	1.47	3000	0.000188	-
S2	1.46	4.3	0.34	1.46	2	0.238	2.49
S3	1.60	8.1	0.20	1.60	2	0.344	2.70
S4	1.60	4.6	0.34	1.60	3300	0.000194	-
S5	1.41	4.3	0.32	1.41	1.8	0.287	2.03
S6	2.06	8.0	0.26	2.06	1.8	0.648	2.32

Table 5.6: Measurement summaries of all samples. R_L is the load resistance which matches TEG's internal resistance($R_L = R_{TEG}$), and R_{diff} is the resistance gotten via I-V figure(Xu & Fobelets, 2014).

For n-type Si, SOD needs to be applied multiple times to generate linear current-voltage characteristics. This is due to phosphorous out-diffusion during the anneal process, resulting in a lower diffused doping concentration inside Si. SOD is carried out 4 times before an Ohmic characteristic is obtained. After 4 SOD applications, the differential resistance for n-type bulk $R_{diff} \approx 2.5\,\Omega$ and for n-type NWAs/bulk $R_{diff} \approx 2.7\,\Omega$. For p-type material only 1 SOD step is necessary to generate Ohmic current-voltage characteristics. The differential resistance obtained for p-type bulk $R_{diff} \approx 2\Omega$ and for p-type NWA/bulk $R_{diff} \approx 2.3\Omega$. Since the difference in R_{diff} between bulk and NWAs/bulk is small, the doping density in the wires is expected to be high and since the material layer is thin we estimate: $R_c \approx R_{diff}$, where R_c is the total contact resistance.

SOD has been applied 4 times on the n-type samples (n_{SOD} is the number of SOD applications), allowing the evaluation of the influence of the doping density on the performance parameters. For the p-type samples a difference in doping density can be obtained by different anneal times, t_a = 10 min, 20 min, 30 min, 60 min and 180 min. The raw data for these measurements is given in Fig. 5.10 and 5.11. The measurements for un-doped and fully doped materials are repeated three times and although some small variation is seen in α, the value of output power P_{out} remains approximately constant.

For both n- and p-type bulk (Fig. 5.10(a) and 5.11(a)) the first observation is that the Seebeck coefficient does not show a clear trend as a function of doping density (via n_{SOD} or t_a). This is because SOD dopes only a thin layer (< 1μm) (Zagozdzon-Wosik, Grabiec & Lux, 1994), (Teh & Chuah, 1989) of the total bulk thickness and thus influences only the contact resistance. There is a clear increasing trend in the value of P_{out} with increasing doping and thus decreasing contact resistance. However, for the NWAs/bulk samples both α and P_{out} are changing. α is decreasing because of increasing doping in the wires (Wanger, 2007), which is given in Fig. 5.12. While P_{out} is increasing because of increasing power factor and decreasing contact resistance.

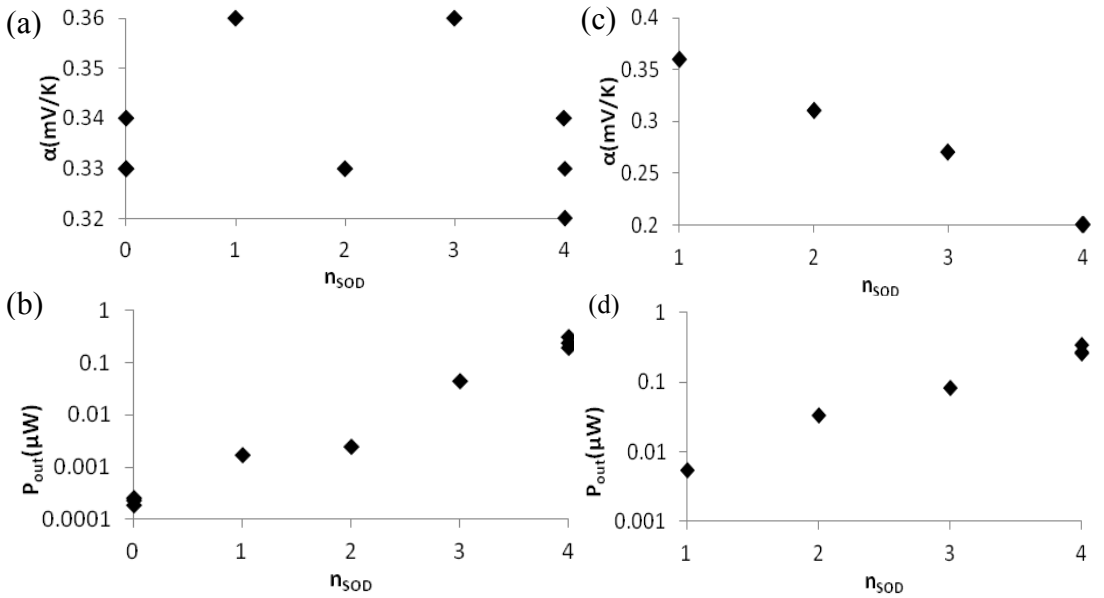


Figure 5.10: Raw performance parameters for n-type Si as a function of SOD applications. (a),(c): Seebeck coefficient. (b),(d): Maximum output power. (a),(b) bulk, (c),(d) NWAs/bulk(Xu & Fobelets, 2014).

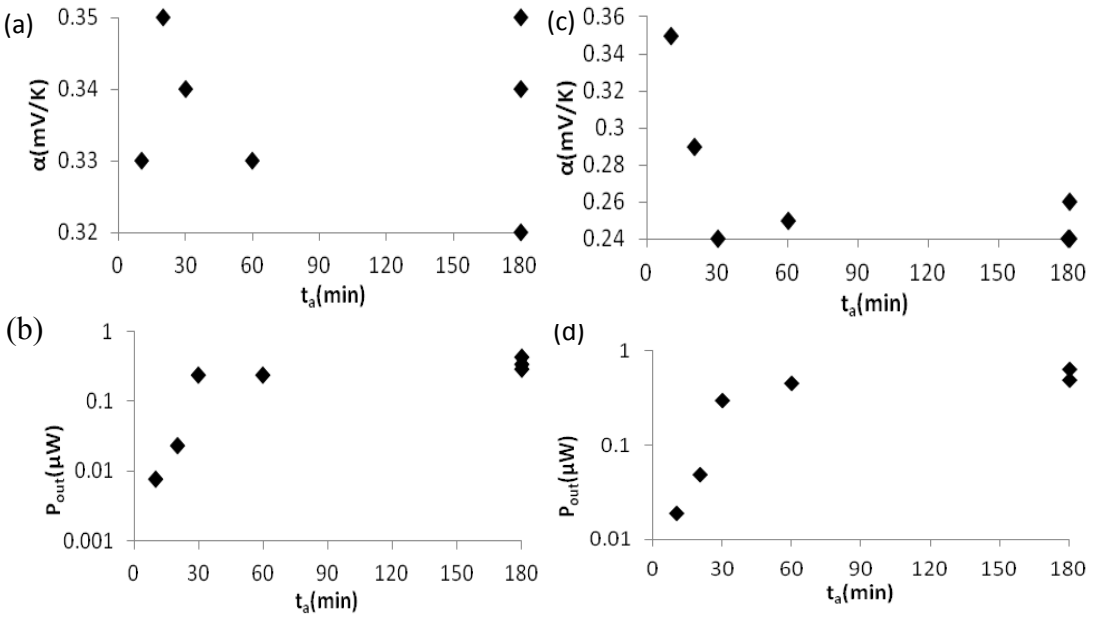


Figure. 5.11: Raw performance parameters for p-Si as a function of anneal time. (a),(c): Seebeck coefficient. (b),(d): Maximum output power. (a),(b) bulk, (c),(d) NWA/bulk(Xu & Fobelets, 2014).

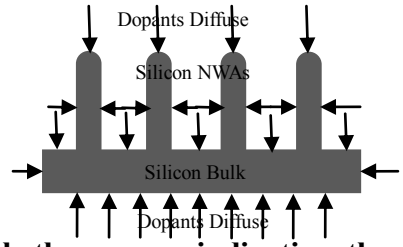


Figure 5.12: Si NWAs with the arrows indicating the direction of the dopants diffusion(Xu & Fobelets, 2014).

Table 5.7 summarizes the raw data points. From the 4-point-probe measurements we find the resistivity of S1 to be $\rho = 0.018\ \Omega \cdot \mathrm{cm}$, associated with a doping concentration $N_D = 1.7 \times 10^{18}\mathrm{cm}^{-3}$, and thus a derived $\alpha = 0.45$ mV/K (Wanger, 2007). For S4, 4-point probe measurements give $\rho = 0.024\ \Omega \cdot \mathrm{cm}$, thus $N_A = 2.3 \times 10^{18}\mathrm{cm}^{-3}$ and $\alpha = 0.44$ mV/K (Wanger, 2007). The difference between measured and the Seebeck coefficient derived from the carrier concentration is mainly caused by the temperature drop at the Cu-Si interface. This means that for S1, about 26% of the total temperature difference is lost across the Cu-Si contact, while for S4 it is about 23%. These two percentages are much smaller than before due to the improvement of measurement set-up, and they will be used to analyze the effective doping parameters for the NWAs/bulk samples. From ΔT in Table 5.7, it is clear that the NWAs/bulk TEGs can maintain a larger temperature difference compared to bulk, due to the lower thermal conductivity of the NWAs.

Sample	$\lvert\alpha\rvert$ (mV/K)	P_{out} (μW)	R_{TEG} (Ω)	ΔT(K)	T_h(°C)	ρ(Ω · cm)
S1	0.33	1.9×10^{-4}	3×10^3	4.4	41	0.019
S2	0.34	0.24	2	4.3	41	–
S3	0.20	0.34	2	8.1	45	–
S4	0.34	1.9×10^{-4}	3.3×10^3	4.6	40	0.024
S5	0.32	0.29	1.8	4.3	41	–
S6	0.26	0.65	1.8	8.0	44	–

Table 5.7: Summary of the extracted parameters. α the Seebeck coefficient; P_{out} the maximum output power, R_{TEG} the internal resistance of the TEG, ΔT the temperature difference, $T_h$the hot side temperature for the same heat flux and ρ the resistivity measured by 4-point-probe measurement(Xu & Fobelets, 2014).

In order to extract the Seebeck coefficient associated to the NWAs only, we follow the process presented in (Krali & Durrani, 2013):

$$\alpha_{NWAs} = \alpha[\left(1 - \frac{\alpha_{Bulk}}{\alpha}\right)\frac{\Delta T}{\Delta T_{NWAs}} + \frac{\alpha_{Bulk}}{\alpha}] \quad (5.4)$$

With α_{NWAs}, α_{Bulk} and α the Seebeck coefficients of Si NWAs, Si bulk and the whole sample, ΔT and ΔT_{NWAs} are the temperature difference of the whole sample and NWAs only. Based on the measured Seebeck coefficients and temperature difference in Table 5.7, as well as the percentage temperature drop across the Cu-Si contacts, the Seebeck coefficients of the p- and n-type Si NWAs only, can be extracted (see Table 5.8).

	p-type Si	n-type Si
$\alpha_{Bulk}(mV/K)$	0.41	0.45
$\alpha(mV/K)$	0.33	0.27
$\alpha_{NWAs}(mV/K)$	0.24	0.08

Table 5.8: Summary of the extracted Seebeck coefficients for the NWAs(Xu & Fobelets, 2014).

Theoretically, the Seebeck coefficient is given by Wanger (Wanger,2007):

$$\alpha = \frac{k}{e}[\ln\left(\frac{N}{N_{c/v}}\right) - (r + \frac{5}{2})] \quad (5.5)$$

With N the doping density, $N_{c/v}$ the effective density of states, k the Boltzman constant, e the unit charge and r the scattering factor. Assuming that the scattering factor is the same in bulk and the NWAs, we can get the following relationship between α_{Bulk} andα_{NWAs}.

$$\alpha_{Bulk} - \alpha_{NWAs} = \frac{k}{e} \ln (\frac{N_{NWAs}}{N_{bulk}}) \quad (5.6)$$

The doping concentration of Si bulk (4-point-probe measurement) and the Seebeck coefficients of bulk and NWAs are known (Table 5.8), thus the doping concentration of the Si NWAs only, can be estimated from eq. (5.6). This gives $N_A = 2.87 \times 10^{19}cm^{-3}$ for the p-type Si NWAs (Xu & Fobelets, 2014), which is less than the boron's solubility in Si ($1 \times 10^{20}cm^{-3}$) (Trumbore,1976). Using this value of N_A and eq. (5.5), we find α= 0.22 mV/K, close to α_{NWA} in Table 5.8. Similarly, for the n-type Si NWAs with n_{SOD}=4, $N_D = 1.39 \times 10^{20}cm^{-3}$ (eq.(5.6)), again less than phosphorous' solubility in Si ($3 \times 10^{20}cm^{-3}$) (Trumbore,1976). This value of N_D gives α= 0.08 mV/K (eq. (5.5)), also consistent with α_{NWA} in Table 5.8. The doping densities extracted from the Seebeck measurements (Table 5.8) are consistent with data on P and B SOD reported in literature. For P doping the carrier density is expected to be ~ $4 \times 10^{20}cm^{-3}$ (Hartiti, Slaoui & Muller et al., 1992) while that of B is ~$2 \times 10^{19}cm^{-3}$ (Mathiot, Lachiq & Slaoui et al., 1998), (Xu & Fobelets, 2014) for similar process parameters as applied in this work. In the n-type NWAs N_D is ~5 times higher than N_A in the p-type NWAs. However, the resistance of the TEG (R_{TEG}) is almost the same for both after SOD. Since R_c dominates R_{TEG}, this results shows that the Cu contact on n-type Si has a higher barrier height and ideality factor than for p-type Si, which is consistent with the analysis in Section 4.3. This necessitates a higher doping concentration for n-type than for p-type for the same R_c and contact area. As a consequence α of the n-type NWAs is lower than that of the p-type NWAs due to its higher doping concentration, resulting in a less optimal power factor.

Based on the extracted doping concentration in the NWAs, we can estimate the NWAs' electrical resistivity by assuming conduction in the NWs is via drift-diffusion processes. The electrical resistivity of p-type NWAs is ~$0.0038\ \Omega \cdot cm$ and of n-type NWAs ~$0.00059\ \Omega \cdot cm$.

The power factor $\alpha^2\sigma$ for n- and p-type Si NWAs and bulk is summarized in Table 5.9.

Samples	$\alpha^2\sigma$ $(\frac{\mu W}{K^2 \cdot cm})$
p-type Si bulk	9.9
p-type Si NWAs	15.9
n-type Si bulk	11.9
n-type Si NWAs	13.4

Table 5.9: Power factor for samples with maximum SOD (Xu & Fobelets, 2014).

When comparing the measurements for bulk, NWAs/bulk and NWAs only, given in Table 5.7 and 5.9, we find that the power factor increase associated with the NWAs for n-type and p-type is respectively 12.8% and 60.7%. Reducing R_c increases P_{out} by a factor of ~1200 for n-type bulk while the combined effect of a reduced R_c, λ_{NWAs} and increased power factor for the NWAs/bulk increase P_{out} by ~1800 for n-type NWAs/bulk. For p-type Si, P_{out} for bulk increases by a factor of ~1500 while that of the NWAs/bulk sample increases by ~3300.

This section shows that the SOD on Si bulk's surface only changes the electrical contact resistance of Cu and Si due to the thin diffusion layer, and the Seebeck coefficient, electrical conductivity and thermal conductivity of Si bulk have not been affected by SOD. Thus, the output power increase of Si bulk-based TEG is due to the significant reduction of R_c.This section also shows that the thin (20μm) NWAs layer attached to bulk can increase the maximumP_{out}. The large improvement of P_{out} is due to the significant reduction of R_c, and the improvement of the power factor of the NWAs only, because the dopants diffusion into Si NWAs as given in Fig. 5.13 reduces the Seebeck coefficient of Si NWAs layer, while increasing the electrical conductivity of Si NWAs layer. In addition, the thermal conductivity of Si NWAs layer is lower than Si bulk, so ZT of Si NWAs layer is also improved in contrast to Si bulk.

The high doping density needed for low R_c in the n-type NWAs based TEGs indicates that for output power optimization the doping for R_c and $\alpha\sigma^2$ improvement needs to be applied independently.

5.4: Output power increase by longer NWAs and small sample areas

As an important factor which affects the TEG's output power, ΔT can be increased by the length of the NWAs. The value of ΔT is proportional to NWAs' length – increasing the length of the NWAs compared to the remaining bulk would increase TEG's output power. A study of the influence of the length of the NWA on the output power of the TEG is given in (Tsai, 2013). An alternative approach is to etch NWAs at both sides of the Si bulk. In this section we investigate the influence of double sided Si NWAs.

Si NWAs were prepared by the MACE recipe given in Section 4.1.2 from a p-type Si

bulk with a resistivity of $\rho = 1 - 10\Omega \cdot \mathrm{cm}$, as well as an n-type bulk with $\rho = 0.01 - 0.02\Omega \cdot \mathrm{cm}$. Two different Si NWAs are fabricated: one with NWAs on one side (SS) and the other with NWAs on both sides (DS) of the bulk. For the p-type Si, L_{NW} for the SS is 23 μm, and L_{NW} for the DS is 23/24μm; for the n-type Si, L_{NW} for the SS is 20 μm, and L_{NW} for the DS is 19/19μm. The cross sectional area of all samples is $\sim 25\,\mathrm{mm}^2$. Longer wires are expected to maintain a larger temperature difference (Tsai, 2013), however, surface depletion/inversion effects for longer wires can increase or invert the Seebeck coefficient (Krali, Li & Fobelets et al., 2011). Using SOD after MACE prevents this due to the high NWAs surface doping, as well as reducing the TEG's internal resistance. The total NWA length of the DS samples is twice that of the SS samples. The Seebeck coefficient and output power measurement set-up used, is given in Fig 2.11 (b), and the pressure applied is $1600\mathrm{N/cm}^2$. The heat influx generated by the heater is constant at 20W for all samples.

The raw measurement results of Seebeck coefficient, range of temperature differences, maximum output power and extracted TEG's internal resistance are given in Table 5.10 under constant heat influx.

Samples	$\alpha_{measurement}(\mathrm{mV/K})$	$\Delta T_{max}(℃)$	$P_{out}^{max}(\mu W)$	$R_{TEG}(\Omega)$
n-type SS ($0.01 - 0.02\Omega \cdot \mathrm{cm}$)	0.38	15.5-16.2	2.4	2.8
n-type DS ($0.01 - 0.02\Omega \cdot \mathrm{cm}$)	0.32	21.6-24.8	3.4	3.3
p-type SS ($1 - 10\Omega \cdot \mathrm{cm}$)	0.30	28.0-28.6	1.5	9
p-type DS ($1 - 10\Omega \cdot \mathrm{cm}$)	0.36	37.0-37.5	3.5	12

Table 5.10: Summary of raw measurement results (Xu, Khouri & Fobelets, 2014).

It is clear that the NWAs length has no big influence on the Seebeck coefficient, because the nanowires surface depletion effects are eliminated by SOD. The maximum output power of the DS sample-based TEG is higher than the one of corresponding SS sample-based TEG, even when the DS sample-based TEG has a higher internal resistance. This is due to the higher temperature difference that can be maintained across the DS samples.

5.5: Conclusions

A TEG's output power is determined by the temperature drop across thermoelectric material and its internal resistance which is composed of thermoelectric material's electrical resistance and the electrical contact resistance between Cu and thermoelectric material.

The increase of temperature drop across thermoelectric material is realized via the decrease of thermoelectric material's thermal conductivity, and two techniques have been used in our research to reduce thermal conductivity: SiGe alloy and NWAs. The output power of Si bulk-based TEG is doubled by using $Si/Si_{0.8}Ge_{0.2}$ bulk, and the application of Si NWAs also doubles the output power of Si bulk-based TEG. The

combination of $Si/Si_{0.8}Ge_{0.2}$ bulk and Si NWAs can increase the output power of Si bulk-based TEG by a factor of 20. The output power of $Si/Si_{0.8}Ge_{0.2}$-, $Si/Si_{0.7}Ge_{0.3}$- and $Si/Si_{0.6}Ge_{0.4}$-based TEG has no big difference, because the change of the thermal conductivity within the Ge concentration range is limited. However, MACE on SiGe with a higher concentration is more challenging and cost of material increases with an increased used of Ge. Therefore, using a 20% Ge fraction is a good compromise between reduction in thermal conductivity and ease of processing/cost of material.

In contrast to temperature drop across thermoelectric material, the influence of internal resistance on the TEG's output power is much bigger in these thin film samples. The dominant term of internal resistance is the electrical contact resistance between Cu and Si which is determined by the Schottky barrier height and ideality factor between Cu and Si. The electrical resistance of the sample is determined by its doping density. The Schottky barrier height and ideality factor between Cu-Si is reduced by doping the semiconductor surface via SOD and improving the contact quality via sputter coating of a Cu layer on the sample's surface. The doping density is increased by SOD and causes the biggest output power improvement. For Si bulk, SOD only reduces the contact resistance between Cu and Si, and for Si NWAs, SOD not only reduces the contact resistance between Cu and Si, but also reduces the electrical resistance of Si nanowires and can improve power factor. The output power can be increased by an order of 3 by the application of NWAs and SOD.

This chapter also demonstrated that the increase of the NWA length by using double sided NWAs, together with the use of SOD increases the output power further.

Chapter 6: Conclusion and future work

This thesis describes all of research achievements that I have realized in my PhD career. This thesis begins with the introduction of thermoelectric material and TEG, and then theoretical ZT model, which is used to characterize thermoelectric material, is systematically introduced, finally TEG's output power, which characterizes TEG's performance more comprehensively, is described, and furthermore, TEG's output power is increased by an order of 3. These research achievements can be split into following:

Chapter 1 gives a brief introduction about three thermoelectric coefficients: Seebeck coefficient, electrical conductivity and thermal conductivity, as well as the relations among them. This chapter also systematically explains why ZT is an important parameter to characterize thermoelectric material from the aspects of TEG's efficiency, followed by the descriptions of semiconductors which are with high ZT. The thermoelectric materials used in this research are Si, SiGe and their nanostructures which have higher ZT in contrast to bulk structures.

Thermoelectric material is only one component of a TEG which is also composed of electrical probes, the contacts between thermoelectric material and electrical probes, heat sources, heat sinks and so on, and these components induce parasitic effects which damage TEG's performance, and TEG's output power as a function of load resistance, which takes account all of these parasitic effects, is used to characterize TEG's overall performance.

Chapter 2 gives thermal conductivities of Si NWs which decreases with increasing porosity, decreasing diameter and increasing surface roughness. The thermal conductivity and Seebeck coefficient of SiGe bulk are not affected a lot by the change of Ge fraction, but a big drop of 96% of thermal conductivity occurs from Si bulk to SiGe bulk. The low thermal conductivity of the matrix material which is filled in NWAs is required in order to boost output power.

One step MACE, which is without H_2O_2, is used to etch SiGe NWAs in order to keep Ge fraction. Two step MACE, which is composed of Ag NPs deposition and Si etching, is used to etch Si NWAs. The quality of the NWAs is related to the bulk's doping concentration, etching time, etching temperature, solution recipe (particularly the concentrations of $AgNO_3$and H_2O_2) and so on.

The measured Seebeck coefficient is undervalued due to the temperature loss at the contacts between thermoelectric material and Cu, and this loss can be eliminated by the application of high pressure and soft interstitial material at the contacts. The Schottky barrier height and ideality factor of contacts between thermoelectric material and Cu is measured via the I-V figure of a Schottky diode structure. The output power

of a TEG as a function of load resistance is measured by providing a constant heat influx, as well as changing the value of load resistance.

Chapter 3 systematically describes ZT of Si bulk, $Si/Si_{0.8}Ge_{0.2}$ bulk and Si bulk/NWs based on the theoretical models of Seebeck coefficient, electrical conductivity and thermal conductivity. ZT of Si bulk whose thickness is 500μ m increases with increasing temperature from 300K to 500K, and ZT of n-type Si bulk is higher than ZT of p-type Si under the same temperature. At 300K, ZT of n-type Si bulk is 0.0035, and ZT of p-type Si bulk is 0.00089. At 500K, ZT of n-type Si is 0.022, and ZT of p-type Si bulk is 0.0045.

$Si/Si_{0.8}Ge_{0.2}$ bulk is constructed by depositing $3\mu m$ thick linearly graded $Si_{1-x}Ge_x$ layer and 3μ m thick $Si_{0.8}Ge_{0.2}$ layer on $500\mu m$ thick Si bulk, and its ZT improvement is very small due to thin SiGe layer in contrast to Si bulk. At 300K, ZT of n-type $Si/Si_{0.8}Ge_{0.2}$ bulk is 0.0040 and ZT of p-type $Si/Si_{0.8}Ge_{0.2}$ bulk is 0.0022.At 500K, ZT of n-type $Si/Si_{0.8}Ge_{0.2}$ bulk is 0.024 and ZT of p-type $Si/Si_{0.8}Ge_{0.2}$ bulk is 0.0085.

The Si bulk/NWs sample is constructed via etching $35\mu m$ long NWs on $500\mu m$ thick Si bulk using MACE. The ZT improvement is larger than the improvement of $Si/Si_{0.8}Ge_{0.2}$ bulk due to two reasons: one is the length of NWs which is much larger than SiGe layer's thickness, and the other one is the Seebeck coefficient improvement of NWs due to quantum confinement effect. At 300K, ZT of n-type Si bulk/NWs is 0.036 and ZT of p-type Si bulk/NWs is 0.022.

TEG's output power is determined by the thermoelectric properties of thermoelectric material and the electrical conductance of the contact between thermoelectric material and Cu. TEG's output power increases with increasing Seebeck coefficient and decreasing thermal conductivity of thermoelectric material. TEG's output power also increases with increasing electrical conductance of the contact between thermoelectric material and Cu, which is characterized by specific contact resistance which is determined by Schottky barrier height and ideality factor at the contact, as well as the doping density of thermoelectric material. The doping density of thermoelectric material is increased by SOD, and the doping density profile is determined by the dopant concentration, thermal diffusion time duration and temperature.

Chapter 4 firstly describes NWAs etching. Ag NPs is deposited on the lightly doped $Si(1-10\Omega\cdot cm)$ bulk surface in Ag deposition solution with volume ratio of $AgNO_3(0.06M):HF(40\%):H_2O=2:5:13$ for 15 minutes, followed by the Si NWAs etching in a solution with volume ratio of $HF(40\%):H_2O:H_2O_2(0.6M)=1:1:2$, and the etching time determines NWAs length.

Ag NPs is deposited on the heavily doped Si($0.01 - 0.02\Omega \cdot \mathrm{cm}$) bulk surface in Ag deposition solution with volume ratio of $\mathrm{AgNO_3(0.06M):HF(40\%):H_2O} = 4:10:33$ for 1.5 minutes, followed by the Si NWAs etching in a solution with volume ratio of $\mathrm{HF(40\%):H_2O:H_2O_2(0.6M)} = 13:37:10$, and the etching time determines NWAs length.

SiGe NWAs is etched by the one-step MACE: Ag deposition and SiGe NWAs etching occur simultaneously in a solution with volume ratio of $\mathrm{AgNO_3(0.06M):HF(40\%)} = 1:1$, and the etching time determines NWAs length.

The dopants for p-type Si is Boron, and the dopants for n-type Si is Phosphorous. They are dropped on the Si surface and spun at 2500rpm for 40s, followed by a soft bake at $200℃$ for 25 minutes to remove solvents. For p-type Si, the thermal diffusion is carried out in a tube furnace in Ar at a temperature of $900℃$ for different durations. For n-type Si, the thermal diffusion is carried out in a RTP furnace with $\mathrm{N_2}$ at $1000℃$ for 1 min, and this thermal diffusion process is repeated several times in order to get maximum doping density.

High Schottky barrier height and ideality factor exists at the contact between Si and Cu, and the Schottky barrier height at n-type Si and Cu contact is higher than the Schottky barrier height at p-type Si and Cu contact. A layer of sputter coated Cu on Si surface can reduce the ideality factor of all contacts, and only reduces the Schottky barrier height at n-type Si and Cu contact, but does not reduce the Schottky barrier height at p-type Si and Cu contact.

Chapter 5 measures output power of TEG. The output power of Si bulk is increased by a factor of 20 by depositing $10\mu\mathrm{m}$ $\mathrm{Si_{0.8}Ge_{0.2}}$ layer, as well as by etching $20\mu\mathrm{m}$ Si NWAs mainly due to lower thermal conductivity.

The absolute value of pn junction's Seebeck coefficient is the sum of the absolute values of individual n-type and p-type samples' Seebeck coefficient.

The output power has an improvement of a factor of 20 by increasing the carrier concentration which is indicated by Si's electrical resistivity from $5.6\Omega \cdot \mathrm{cm}$ to $0.01\Omega \cdot \mathrm{cm}$.

The output power of Si bulk is increased by 3300 times by the application of $20\mu\mathrm{m}$ Si NWAs, followed by SOD applied on Si NWAs and Si bulk simultaneously due to the reduce of thermal conductivity and Si NWAs' increase in power factor.

The increase of the NWAs length by using double sided NWAs, together with the use of SOD doubles the output power further.

The improvement on TEG's output power is a top priority in TEG's research, and several improvements and measurement methods on thermoelectric properties can be done in future work based on current foundations:

1: TEG's output power can be measured under forced cooling, such as adding a ventilator to the cooling fin in order to increase the temperature difference.

2: SOD reduces the contact resistance between Si and Cu, but it also reduces Seebeck coefficient of Si NWs due to higher doping density in Si NWs. In the future work, the dopants only diffuse at the top of Si NWs by protecting Si NWs before SOD so that the Cu-Si contact resistance is reduced without reducing Seebeck coefficient. The contact resistance and thermoelectric material's power factor are improved separately.

3: Fabricating integrated structure such that contacts can be deposited rather than having to use pressure contacts

4: MACE will be researched more in order to get the recipes which can optimize the trade-off between NWs thermal conductivity and its robustness for Si bulks with different doping densities.

5: Thermal conductivity has not been referred to in this thesis, and it will be researched in future work. In addition, as an option to measure ZT directly, Transit-Harman technique will be researched in future work (Bian, Zhang & Schimidt et al., 2005), (Singh, Bian & Zeng et al., 2005).

6: The thermal conductivity can be reduced further by super lattice structure besides the application of NWs and $Si_{1-x}Ge_x$ alloy. Super lattice, especially its NWs etching will be researched in future work.

7: Research the relations between thermoelectric material's ZT and TEG's output power.

According to above descriptions, future work is concerned with three aspects: first aspect is to solve the measurement problems of thermal conductivity and ZT; second aspect is to boost TEG's output power further by improving thermoelectric material's power factor, as well as reducing thermoelectric material's thermal conductivity and contact resistance between metal and thermoelectric material; third aspect is to establish the functions between thermoelectric material's ZT and TEG's output power.

Reference

[1] Abeles, B. (1963) Lattice thermal conductivity of disordered semiconductor alloys at high temperatures. *Physical Review*. 131 (5), 1906.

[2] Amazon.co.uk, (2014) *Hanson HX5000 Glass Electronic Bathroom Scale*. [Online]. 2014. Available from: http://www.amazon.co.uk/Hanson-HX5000-Glass-Electronic-Bathroom/dp/B0017J6YVM [Accessed: 23 September 2014].

[3] Anderson, B., Anderson, R., Deng, N. & Tian, L. et al. (2008) *Ban Dao Ti Qi Jian Ji Chu*. 1st edition. Beijing, Tshinghua University Press.

[4] Bhandari, C. & Rowe, D. (1980) Silicon--germanium alloys as high-temperature thermoelectric materials. *Contemporary Physics*. 21 (3), 219--242.

[5] Bian, Z., Zhang, Y., Schimidt, H. & Shakouri, A. (2005) Thin film ZT characterization using transient Harman technique. In: *the 24th International conference on thermoelectric*. 2005

[6] Bouki,A., Bunimovich,J.,Tahir-Kheli,J.,Yu,J.,Goddard,W.&Heath,J. (2008) Slicon nanowires as efficient thermoelectric materials. *Nature.*451, 168-171.

[7] Bux, S., Fleurial, J. & Kaner, R. (2010) Nanostructured materials for thermoelectric applications. *Chemical Communications*. 46 (44), 8311--8324.

[8] Carboncounted.co.uk, (2014) *When Will Fossil Fuels Run Out*. [Online]. 2014. Available from: http://www.carboncounted.co.uk/when-will-fossil-fuels-run-out.html [Accessed: 23 September 2014].

[9] Chang, C., Fang, Y. & Sze, S. (1971) Specific contact resistance of metal-semiconductor barriers. *Solid-State Electronics*. 14 (7), 541--550.

[10] Chapman, A. (1987) *Fundamentals of heat transfer*. 1st edition. New York, Macmillan.

[11] Cooper, M., Mikic, B. & Yovanovich, M. (1969) Thermal contact conductance. *International Journal of heat and mass transfer*. 12 (3), 279--300.

[12] Curtin, B. & Bowers, J. (2012) Thermoelectric Properties of Silicon Nanowire Array and Spin-on Glass Composites Fabricated with CMOS-compatible Techniques. *Materials Research Society*. 1408(99), 10.1557.

[13] Davila, D., Tarancon, A., Calaza, C. & Salleras, M. et al. (2012) Monolithically integrated thermoelectric energy harvester based on silicon nanowire arrays for powering micro/nanodevices. *Nano energy*. 1 (6), 812--819.

[14] Dismukes, J., Ekstrom, L., Steigmeier, E. & Kudman, I. et al. (1964) Thermal and Electrical Properties of Heavily Doped Ge-Si Alloys up to 1300° K. *Journal of Applied Physics*. 35 (10), 2899--2907.

[15] Dorkel, J. & Leturcq, P. (1981) Carrier mobilities in silicon semi-empirically related to temperature, doping and injection level. *Solid-State Electronics*. 24 (9), 821--825.

[16] Dresselhaus, M., Chen, G., Tang, M. & Yang, R. et al. (2007) New Directions for Low-Dimensional Thermoelectric Materials. *Advanced Materials*. 19 (8), 1043--1053.

[17] Emin, D. (2006) Effects of Charge Carriers'Interactions on Seebeck Coefficients. In: David Michael Rowe (ed.). *Thermoelectrics handbook*. 1st edition. USA, CRC Press.

[18] Feser, J., Sadhu, J., Azeredo, B. & Hsu, K. et al. (2012) Thermal conductivity of silicon nanowire arrays with controlled roughness. *Journal of Applied Physics*. 112 (11), 114306.

[19] Fischetti, M. & Laux, S. (1996) Band structure, deformation potentials, and

carrier mobility in strained Si, Ge, and SiGe alloys. *Journal of Applied Physics*. 80 (4), 2234--2252.

[20] Fobelets, K. (2010) *Advanced Electronic Devices, EE9AO8*.

[21] Futurrex.com, (2014) *Spin-On Dopants*. [Online]. 2014. Available from: http://futurrex.com/en/products/spin-on-dopants.html [Accessed: 22 September 2014].

[22] Geballe, T. & Hull, G. (1955) Seebeck effect in silicon. *Physical Review*. 98 (4), 940.

[23] Gholami, S. & Khakbaz, M. (2011) Measurement of I-V Characteristics of a Pt Si/p-Si Schottky Barrier Diode at low Temperatures. *World Academy of Science, Engineering and Technology*. 57,1001-1004.

[24] Glassbrenner,C. & Slack,G. (1964) Thermal Conductivity of Silicon and Germanium from 3K to the Melting Point. *Phys.Rev.*134,A1058-A1069.

[25] Gmelin, E., Asen-Palmer, M., Reuther, M. & Villar, R. (1999) Thermal boundary resistance of mechanical contacts between solids at sub-ambient temperatures. *Journal of Physics D: Applied Physics*. 32 (6), 19.

[26] Goyne, K., Zimmerman, A., Newalkar, B. & Brantley, S. et al. (2002) Surface Charge of Variable Porosity Al_2O_3(s) and SiO_2(s) Adsorbents. *Journal of Porous Materials*. 9 (4), 243-256.

[27] Hartiti, B., Slaoui, A., Muller, J. & Stuck, R. et al. (1992) Phosphorus diffusion into silicon from a spin-on source using rapid thermal processing. *Journal of applied physics*. 71 (11), 5474--5478.

[28] Hazra, P., Chakrabarti, P. & Jit,s.(2012) Fabrication and characterization of p-type Si NW/n-type ZnO heterostructure for optoelectronics application. In: *International conference on materials science and technology.* 2012.

[29] He, J., Liu, Y. & Funahashi, R. (2011) Oxide thermoelectrics: the challenges, progress, and outlook. *Journal of Materials Research*. 26 (15), 1762--1772.

[30] Hebb, J. & Jensen, K. (2014) The Effect of Patterns on Thermal Stress During Rapid Thermal Processing of Silicon Wafers. *IEEE Transcations on Semiconductor Manufacturing*. 11 (1), 99-107.

[31] Hochbaum, A., Chen, R., Delgado, R. & Liang, W. et al. (2008) Enhanced thermoelectric performance of rough silicon nanowires. *Nature*. 451 (7175), 163--167.

[32] Huang, Z., Geyer, N., Werner, P. & De Boor, J. et al. (2011) Metal-Assisted Chemical Etching of Silicon: A Review. *Advanced materials*. 23 (2), 285--308.

[33] Jiang, H. (2011) *Characterization of thermoelectric generators based on silicon*. MSc. Imperial College London.

[34] Karacalıoğlu, G. (2014) *Energy Resources for Space Missions*. [Online]. 2014. Space Safety Magazine. Available from: http://www.spacesafetymagazine.com/aerospace-engineering/nuclear-propulsion/energy-resources-space-missions/ [Accessed: 23 September 2014].

[35] Keithley.com, (2014) *Model 2000 Digital Multimeter 6-1/2-Digit, GPIB/RS232*. [Online]. 2014. Available from: http://www.keithley.com/products/dcac/dmm/broadpurpose/?mn=2000 [Accessed: 22 September 2014].

[36] Keysight.com, (2014) *4155B / 4156B Semiconductor Parameter Analyzers [Obsolete] | Keysight (formerly Agilent Test and Measurement)*. [Online]. 2014. Available from: http://www.keysight.com/en/pd-542813-pn-4155B/semiconductor-parameter-analyzers?&cc=GB&lc=eng [Accessed: 22 September 2014].

[37] Khounsary, A., Chojnowski, D., Assoufid, L. & Worek, W. (1997) Thermal

contact resistance across a copper-silicon interface. *SPIE.* 3151, 45--51.

[38] Kimukin, I., Islam, M. & Williams, R. (2006) Surface depletion thickness of p-doped silicon nanowires grown using metal-catalysed chemical vapour deposition. *Nanotechnology*. 17 (11), 240.

[39] Krali, E. & Durrani, Z. (2013) Seebeck coefficient in silicon nanowire arrays. *Applied Physics Letters*. 102 (14), 143102.

[40] Krali, E., Li, C., Fobelets, K. & Durrani, Z. (2011) In:*9th European Conference on Thermoelectrics.* 2011

[41] Li, C., Xu, B., Durrani, Z. & Fobelets, K. (2011) SiGe nanowire arrays fabrication and their Seebeck coefficient characterisation. In: *the 9 th European Conference on Thermoelectrics*. 2011

[42] Li,S.(2006) *Semiconductor physical electronics.* 2nd edition.New York, Springer.

[43] Li, S. & Thurder, W. (1977) The dopant density and temperature dependence of electron mobility and resistivity in N-type silicon. *Solid-State Electronics*. 20 (7), 609--616.

[44] Li, Y., Buddharaju, K., Singh, N. & Lo, G. et al. (2011) Chip-level thermoelectric power generators based on high-density silicon nanowire array prepared with top-down CMOS technology. *Electron Device Letters, IEEE*. 32 (5), 674--676.

[45] Li, Y., Buddharaju, K., Tinh, B. & Singh, N. et al. (2012) Improved vertical silicon nanowire based thermoelectric power generator with polyimide filling. *Electron Device Letters, IEEE*. 33 (5), 715--717.

[46] Li, Y., Qian, F., Xiang, J. & Lieber, C. (2006) Nanowire electronic and optoelectronic devices. *Materials today*. 9 (10), 18--27.

[47] Mathiot, D., Lachiq, A., Slaoui, A. & No"el, S. et al. (1998) Phosphorus diffusion from a spin-on doped glass (SOD) source during rapid thermal annealing. *Materials science in semiconductor processing*. 1 (3), 231--236.

[48] Mingo, N., Yang, L., Li, D. & Majumdar, A. (2003) Predicting the thermal conductivity of Si and Ge nanowires. *Nano Letters*. 3 (12), 1713--1716.

[49] Minnich, A., Dresselhaus, M., Ren, Z. & Chen, G. (2009) Bulk nanostructured thermoelectric materials: current research and future prospects. *Energy & Environmental Science*. 2 (5), 466--479.

[50] Myflukestore.com, (2014) *Fluke 52 II Digital Thermometer - Fluke Corporation*. [Online]. 2014. Available from: http://www.myflukestore.com/p1271/fluke_52_ii_digital_thermometer.php [Accessed: 22 September 2014].

[51] Myronov, M., Liu, X., Dobbie, A. & Leadley, D. (2011) Control of epilayer thickness during epitaxial growth of high Ge content strained Ge/SiGe multilayers by RP-CVD. *Journal of Crystal Growth.* 318 (1), 337-340.

[52] Padovani, F. & Stratton, R. (1966) Field and thermionic-field emission in Schottky barriers. *Solid-State Electronics*. 9 (7), 695--707.

[53] P'erez-Aparicio, J., Taylor, R. & Gavela, D. (2007) Finite element analysis of nonlinear fully coupled thermoelectric materials. *Computational Mechanics*. 40 (1), 35--45.

[54] Peng, K., Wu, Y., Fang, H. & Zhong, X. et al. (2005) Uniform, Axial-Orientation Alignment of One-Dimensional Single-Crystal Silicon Nanostructure Arrays. *Angewandte Chemie International Edition*. 44 (18), 2737--2742.

[55] Peng, K., Yan, Y., Gao, S. & Zhu, J. (2003) Dendrite-Assisted Growth of Silicon Nanowires in Electroless Metal Deposition. *Advanced Functional*

Materials. 13 (2), 127--132.

[56] Peng, K., Yan, Y., Gao, S. & Zhu, J. (2002) Synthesis of large-area silicon nanowire arrays via self-assembling nanoelectrochemistry. *Advanced Materials*. 14 (16), 1164.

[57] Pichanusakorn,P.&Bandaru,P,R.(2009) The optimal Seebeck coefficient for obtaining the maximum power factor in thermoelectric. *Applied Physics Letters.*94,223108.

[58] Pierret, R. & Huang, R. (2004) *Ban dao ti qi jian ji chu (Semiconductor Device Fundamentals)*. 1st edition. Beijing, Dian zi gong ye chu ban she.

[59] Prasher, R. (2006) Thermal interface materials: historical perspective, status, and future directions.*Proceedings of the IEEE.* 94 (8), 1571--1586.

[60] Qu, Y., Liao, L., Li, Y. & Zhang, H. et al. (2009) Electrically conductive and optically active porous silicon nanowires. *Nano letters*. 9 (12), 4539--4543.

[61] Rowe, D. (1995) *CRC handbook of thermoelectrics*. 1st edition. Boca Raton, FL, CRC Press.

[62] Schroder, D. (1998) *Semiconductor material and device characterization*. 2nd edition. New York, A Wiley-Interscience Publication.

[63] ScienceDaily, (2014) *Nano-breakthrough: Dramatic Increase In Thermoelectric Efficiency Heralds New Era In Heating, Cooling And Power Generation*. [Online]. 2014. Available from: http://www.sciencedaily.com/releases/2008/03/080320150027.htm [Accessed: 23 September 2014].

[64] Shanks, H., Maycock, P., Sidles, P. & Danielson, G. (1963) Thermal conductivity of silicon from 300K to 1400K. *Physical Review*. 130 (5), 1743-1748.

[65] Simpkins, B., Mastro, M., Eddy Jr, C. & Pehrsson, P. (2008) Surface depletion effects in semiconducting nanowires. *Journal of Applied Physics*. 103 (10), 104313.

[66] Singh, R., Bian, Z., Zeng, G. & Zide, J. et al. (2005) Transient Harman measurement of the cross-plane ZT of InGaAs/InGaAlAs superlattices with embedded ErAs nanoparticles. *Materials Research Society*. 886, 10.1557/PROC-0886-F04-04.

[67] Slack, G. & Hussain, M. (1991) The maximum possible conversion efficiency of silicon-germanium thermoelectric generators. *Journal of applied physics*. 70 (5), 2694--2718.

[68] Smith, B. & Rhoderick, E. (1971) Schottky barriers on P-type silicon. *Solid-State Electronics*. 14 (1), 71--75.

[69] Snyder, G. (2008) Small thermoelectric generators. *The Electrochemical Society Interface*. 17 (3), 54.

[70] Su, Z. (2014) *Improved Thermoelectric Performance of P-type Polycrystalline Bi_2Te_3via Hydrothermal Treatment with Alkali Metal Salts*. Ph.D. Clemson University.

[71] Sze,S.&Ng,K.(2006) *Physics of semiconductor devices.* 3rd edition. New York, John Wiley&Sons.

[72] Teh, S. & Chuah, D. (1989) Diffusion profile of spin-on dopant in silicon substrate. *Solar energy materials*. 19 (3), 237--247.

[73] Tritt, T. & Subramanian, M. (2006) Thermoelectric materials, phenomena, and applications: A bird's eye view. *MRS Bulletin.* 31, 188-229.

[74] Trumbore,F.(1976) Solid solubilities of impurity elements in germanium and silicon. *Bell system, Tech.J.* 19,911, 38-43.

[75] Tsai, H. (2013) Effect of substrate type and thickness on power output of silicon nanowire thermoelectric device. In *Proc. IEEE 2nd ISNE.*2013.

[76] Turner, M. & Rhoderick, E. (1968) Metal-silicon Schottky barriers. *Solid-State Electronics*. 11 (3), 291--300.

[77] Uk.comsol.com, (2014) *COMSOL Multiphysics*. [Online]. 2014. Available from: http://www.uk.comsol.com/ [Accessed: 24 September 2014].

[78] Usami, A., Ando, M., Tsunekane, M. & Wada, T. (1992) Shallow-junction formation on silicon by rapid thermal diffusion of impurities from a spin-on source. *Electron Devices, IEEE Transactions on*. 39 (1), 105--110.

[79] Vick, G. & Whittle, K. (1969) Solid solubility and diffusion coefficients of boron in silicon. *Journal of the Electrochemical Society*. 116 (8), 1142--1144.

[80] Vishay, (2014) *Low Profile Aluminum Load Cell*. [Online]. 2014. Available from: http://www.vishaypg.com/docs/12010/1042.pdf [Accessed: 22 September 2014].

[81] Vishay, (2014) *Wirewound Resistors, Industrial Power, Aluminum Housed, Chassis Mount*. [Online]. 2014. Available from: http://www.vishay.com/docs/30201/30201.pdf [Accessed: 22 September 2014].

[82] Vo, T., Williamson, A., Lordi, V. & Galli, G. (2008) Atomistic design of thermoelectric properties of silicon nanowires. *Nano letters*. 8 (4), 1111--1114.

[83] Wang, W., Jia, F., Huang, Q. & Zhang, J. (2005) A new type of low power thermoelectric micro-generator fabricated by nanowire array thermoelectric material. *Microelectron Engineering.* 77 (3/4), 223-229.

[84] Wanger, M. (2007) *Simulation of Thermoelectric Devices*. Ph,D,. Technischen University Wien, Austria.

[85] Wehmeier, N., Schraps, G., Wagner, H. & Lim, B. et al. (2013) Boron-doped PECVD silicon oxides as diffusion sources for simplified high-efficiency solar

cell fabrication. In: *28th European Photovoltaic Solar Energy Conference and Exhibition*. 2013

[86] Weisse, J., Marconnet, A., Kim, D. & Rao, P. et al. (2012) Thermal conductivity in porous silicon nanowire arrays. *Nanoscale research letters*. 7 (1), 1--5.

[87] Wikipedia, (2013) *Energy harvesting*. [Online]. 2013. Available from: http://en.wikipedia.org/wiki/Energy_harvesting [Accessed: 10 March 2013].

[88] Wikipedia, (2014) *Thermoelectric generator*. [Online]. 2014. Available from: http://en.wikipedia.org/wiki/Thermoelectric_generator [Accessed: 23 September 2014].

[89] Xu, B. & Fobelets, K. (2014) Spin-on-doping for output power improvement of silicon nanowire array based thermoelectric power generators. *Journal of Applied Physics*. 115 (21), 214306.

[90] Xu, B., Khouri, W. & Fobelets, K. (2014) Two-Sided Silicon Nanowire Array/Bulk Thermoelectric Power Generator. *Electron Device Letters, IEEE.* 35(5), 596-598.

[91] Xu, B., Li, C., Myronov, M. & Fobelets, K. (2013) n-Si--p-$Si_{1-x}Ge_x$ nanowire arrays for thermoelectric power generation. *Solid-State Electronics*. 83,107--112.

[92] Xu, B., Li, C., Thielemans, K. & Myronov, M. et al. (2012) Thermoelectric Performance of Nanowire Arrays. *Electron Devices, IEEE Transactions*. 59 (12), 3193--3198.

[93] Xu, B. (2012) *Si/SiGe thermoelectric generator*. Ph.D. transfer report. Imperial College London.

[94] Yu, A. (1970) Electron tunneling and contact resistance of metal-silicon contact barriers. *Solid-State Electronics*. 13 (2), 239--247.

[95] Zagozdzon-Wosik, W., Grabiec, P. & Lux, G. (1994) Silicon doping from phosphorus spin-on dopant sources in proximity rapid thermal diffusion. *Journal of applied physics*. 75 (1), 337--344.

[96] Zeghbroeck,B.(2007) *Principles of semiconductor devices.* Boulder, University press of Colorado.

[97] Zhang, M., Peng, K., Fan, X. & Jie, J. et al. (2008) Preparation of large-area uniform silicon nanowires arrays through metal-assisted chemical etching. *The Journal of Physical Chemistry C*. 112 (12), 4444--4450.

[98] Zhang, W., Li, Z., Luo, J. & Chang, Y. et al. (1998) Carrier freeze-out in strained pSi1-xGex layers. In: *the 5th International Conference on Solid - State and Integrated Circuit Technology*. 1998 .

[99] Zhang, W., Zeng, Z. & Luo, J. (1996) Analysis of carriersâ€™ concentration and effective state density of Si1-xGex. *Research and Progress of SSE*. 16 (4), 314-318.